

LA-UR-19-25002 (Accepted Manuscript)

An anisotropic damage model based on dislocation-mediated nucleation of cracks under high-rate compression

Daphalapurkar, Nitin Pandurang
Luscher, Darby Jon
Versino, Daniele
Margolin, Len G.
Hunter, Abigail

Provided by the author(s) and the Los Alamos National Laboratory (2019-12-18).

To be published in: Journal of the Mechanics and Physics of Solids

DOI to publisher's version: 10.1016/j.jmps.2019.103818

Permalink to record: <http://permalink.lanl.gov/object/view?what=info:lanl-repo/lareport/LA-UR-19-25002>

Disclaimer:

Los Alamos National Laboratory, an affirmative action/equal opportunity employer, is operated by Triad National Security, LLC for the National Nuclear Security Administration of U.S. Department of Energy under contract 89233218CNA000001. By approving this article, the publisher recognizes that the U.S. Government retains nonexclusive, royalty-free license to publish or reproduce the published form of this contribution, or to allow others to do so, for U.S. Government purposes. Los Alamos National Laboratory requests that the publisher identify this article as work performed under the auspices of the U.S. Department of Energy. Los Alamos National Laboratory strongly supports academic freedom and a researcher's right to publish; as an institution, however, the Laboratory does not endorse the viewpoint of a publication or guarantee its technical correctness.

An anisotropic damage model based on dislocation-mediated nucleation of cracks under high-rate compression

Nitin P. Daphalapurkar¹, Darby J. Luscher, Daniele Versino

*Theoretical Division, Los Alamos National Laboratory
PO Box 1663, Mailstop B216, Los Alamos, NM 87545, U.S.A.*

Len Margolin, Abigail Hunter

*X Computational Physics Division, Los Alamos National Laboratory
PO Box 1663, Mailstop T086, Los Alamos, NM 87545, U.S.A.*

Abstract

We developed a thermodynamically-consistent, rate-dependent micromechanics model for brittle damage nucleated by dislocation plasticity applicable for large deformations. Dislocation substructure evolution was used to inform a nucleation criterion for a microcrack. Under global compression, the sliding of a microcrack induces formation of wing cracks. Effective stress drives dynamic growth of these cracks under a 3D stress state, resulting in an anisotropic material stiffness. The model was further advanced to predict grain size dependence of a polycrystalline solid. Internal variables were constrained based on the laws of thermodynamics. Material constants were calibrated for polycrystalline beryllium to demonstrate the applicability of the model to simulate dynamic failure under compression. We demonstrate the versatility of the model to capture brittle to ductile transition governed by temperature and strain rate. The predictive capability of the model to simulate failure stress and failure strain is compared with dynamic and quasistatic data on beryllium.

Keywords: HCP, fracture, cracks, kinetics, damage, viscoplastic

¹Corresponding author. E-mail: nitin@lanl.gov

Contents

1	Introduction	4
2	Background	4
3	Kinematics of finite deformation for polycrystalline plasticity and damage	7
3.1	Macroscopic deformation	9
3.2	Definition of Damage	11
3.3	Kinematics in intermediate configurations	14
4	Micromechanics and continuum descriptions of deformation and damage	15
4.1	Dislocation-based plasticity	15
4.2	Dislocation-mediated crack nucleation	19
4.3	Microcracking-based damage	24
5	Thermodynamics and balance laws	32
5.1	Reversible matrix elasticity	35
5.2	Load-induced damage growth	36
5.3	Irreversible matrix plasticity	37
5.4	Evolution of temperature	39
5.5	Pressure- and temperature-dependent shear modulus	40
6	Numerical implementation	41
6.1	Overview of constitutive equations	41
6.2	Plastic deformation update	42
6.2.1	Plastic flow update in the current configuration, \mathcal{B}	42
6.2.2	Plastic flow update in elastic unloaded configuration, $\bar{\mathcal{B}}$	43
6.2.3	Plastic flow update in the elastic and damage unloaded configuration, $\tilde{\mathcal{B}}$	43
7	Application of the model	44
7.1	Experimental Results on Beryllium	44
7.2	Calibration of the model	45
7.3	Results and Discussion	47
7.3.1	Representative results	48

7.3.2	Calibration with high rate and quasistatic experiments in compression	50
7.3.3	Brittle to ductile transition with temperature	51
7.3.4	Rate-dependence of dynamic failure strength	52
7.3.5	Grain size dependence of failure strain	55
7.3.6	Tension-compression asymmetry in the failure strength	57
7.3.7	Strengths and limitations of the proposed model	58
8	Conclusions	61
9	Appendix	63
9.1	Appendix 1: Kinematic measures	63
9.2	Appendix 2: Dislocation-based plasticity	66
9.3	Appendix 3: Stress update scheme for viscoplastic damage constitutive model	69

1. Introduction

A class of materials demonstrate failure response through brittle cracking by the appearance of fracture surfaces, despite the presence of dislocation plasticity. Examples of such materials are beryllium (Papirov et al., 1979), zinc (Kamdar, 1971), magnesium oxide (Stokes et al., 1958), zirconium-hydrogen alloys (Westlake, 1963), and sapphire (Pollock and Hurley, 1973). These materials are characterized by low order of crystal symmetry and tend to possess limited active slip systems for dislocation slip. The focus of our work is on the failure response of a hexagonal closed-packed (HCP) metal, beryllium.

Beryllium (Be) is a strong, lightweight, and also a toxic metal used in the defense, aerospace and electronics industries. Modulus to density ratio is almost six times higher than that of aluminum, titanium, and steel. The specific strength of beryllium outweighs magnesium, which is considered a next-generation metal for light-weighting of structures. High melting temperature and excellent thermal stability make beryllium a material of strategic and critical importance for defense applications.

Beryllium demonstrates a brittle to ductile transition with temperature (Armstrong, 1968). This transition is measured by the stress-strain behavior, in which failure is determined with either a failure strain or a failure stress. Using such measurements for model development has resulted most commonly in models of dynamic strength, which predict a failure stress. Conversely prediction of a failure strain and related model development has received significantly less attention. This work addresses the strain rate and temperature dependence of failure stress and failure strain. This work is based upon a postulate that the competition between the kinetics of damage and the kinetics of viscoplastic deformation can successfully explain the brittle to ductile transition with strain rate as well as with temperature.

2. Background

The deformation of beryllium at room temperature and quasistatic rates is predominantly through basal slip, while prismatic slip is activated at high stress or at high temperature, and pyramidal twinning is activated at high strain and/or at high strain rates (Regnier and Dupouy, 1970; Green and Sawkill, 1961; Blumenthal et al., 1998). The predominant basal slip system coincides with the preferred plane for cleavage fracture.

The nonlinear failure response of quasi-brittle materials under remote tension is attributed to the dislocation-mediated growth of cracks (Zener, 1948), which were later comprehensively analyzed by Stroh (Stroh, 1958). These *Zener-Stroh* cracks

(here onward referred to as *Stroh* cracks) commonly nucleate at sites susceptible to high stress intensity, such as dislocation cell walls terminated by grain boundaries, inclusions, and other material heterogeneities (Johnston et al., 1962). Such materials are weak in tension, compared to their strength in compression. The ratio of their strengths in compression to tension is lower in comparison to brittle materials with limited plastic deformation such as ceramics, which have a strength ratio in the range 8-10 (Kimberley et al., 2013). Under remote compression, these nucleated Stroh cracks further exhibit sliding resulting in nucleation and growth of wing cracks (Stokes et al., 1958; Nemat-Nasser and Obata, 1988). Despite the overall compressive load, the wing cracks tend to grow under local tension and at a finite angle to the Stroh crack. Growing cracks degrade the material stiffness and contribute to the inelastic strain. Before stress softening, the material demonstrates a peak stress on the characteristic stress-strain response (Paliwal and Ramesh, 2008). We will refer to this peak as the ultimate stress or strength.

Dislocation-based viscoplastic models have considerably evolved since the dislocation-density based mechanical threshold stress (MTS) model of Follansbee and Kocks (1988). Austin and McDowell (2011) developed a physically-based model to address slip in polycrystalline metals subjected to high rates of deformation, above 10^4 s^{-1} . The treatment of dislocation density involved mobile and immobile dislocation densities as internal variables, which enabled physical descriptions of plastic flow rate and slip resistance. Their theory does not include a saturation term for dislocation density (Oudriss and Feaugas, 2016), which is commonly used for metals undergoing large deformation (Beyerlein and Tomé, 2008). Lloyd et al. (2014) extended the approach of Austin and McDowell (2011) to include crystal-based thermoelasticity, anisotropic plasticity kinetics, and distinguishing interactions with forest and parallel dislocation densities. In addition, Follansbee and Kocks (1988) demonstrated rate dependence of the trapping term for the dislocation density, which is relevant to simulating mechanical response over a wide range of strain rates from quasistatic to dynamic. Under high rate deformation and for large strains, dissipation from damage as well as plastic deformation can lead to significant increase in the temperature. Luscher et al. (2018) presented thermodynamically consistent strategies for computing the temperature.

Dynamic brittle-damage models based on the micromechanics of wing-crack growth have considerably evolved in their ability to predict dynamic response under compression. A model based on an accurate representation of damage strain is able to capture development of load-induced anisotropy and bulking (Nemat-Nasser and Obata, 1988). Deshpande et al. (Deshpande and Evans, 2008; Deshpande et al., 2011) inspired a rational for including plasticity, based on the observation of dislo-

cations in ceramics under confined compression. Their model demonstrated the role of plasticity in modulating the failure strength under increased confining pressure. However, their model is restricted to small strains as is the case for high-strength ceramics under dynamic loading. For brittle materials, the failure strain often coincides with the ultimate strain, since a brittle solid typically undergoes catastrophic failure post ultimate stress. Because of uncertainties associated with measured failure strains, validation attempts of failure strain predictions from brittle damage models are less common in the literature.

In general, cracking-activated brittle damage models predict a tensile failure strength that is approximately one-tenth of the compressive failure strength. Under quasistatic tensile rates, the brittle strength is commonly estimated using Irwin's fracture criterion (Irwin, 1957). Under quasistatic compression, the brittle failure is commonly assumed to occur through activation of wing cracks from crack sliding. A ceramic material with a crack size of the order $5 \mu\text{m}$ demonstrates a uniaxial compressive stress of the order 5 GPa (Deshpande and Evans, 2008). Under large confinement pressure, these models predict an increased failure strain due to arrested propagation of microcracks. However, these models excluded any temperature- or rate-dependence of the failure response. With increasing strain rate, purely brittle-damage models predict increasing values of both failure stress and failure strain (Paliwal and Ramesh, 2008). However, beryllium measurements demonstrate decreasing failure strain with increasing strain rate (Blumenthal et al., 1998). Thus, purely brittle damage models are insufficient in predicting this anomalous response of beryllium under dynamic loading.

Winey and Gupta (2014) developed a single crystal model for studying shock response of beryllium, employing independent models for dislocation-density evolution and shear cracking within a thermomechanical formulation. For temperatures above 523 K, prismatic slip system becomes activated (Taylor and Moore, 1964) and is thought to result in enhanced plasticity (Barker et al., 1987). Nonetheless, the consequence of this enhanced plasticity potentially resulting in an increased failure strain has not been demonstrated. In addition, beryllium demonstrates increasing failure strain with decreasing rate of loading from 4000s^{-1} to 0.001s^{-1} , often referred to as the brittle to ductile transition with rate (Blumenthal et al., 1998). However, the rate-dependence of this brittle to ductile transition remains unclear.

The interaction between models of dislocation plasticity and the microcrack growth under quasistatic and fatigue loading rates were introduced by Nicolas et al. (2017) and Anahid et al. (2011), respectively. Their analysis is based on the dislocation-mediated crack nucleation theory by Stroh (Stroh, 1954). The model by Nicolas et al. (2017) is temperature independent, appropriate for small strains ($< 5\%$), and the mi-

crocracking was based on isotropic damage with application to rocks. Their analysis prescribed pre-existing crack sizes, which subsequently resulted in damage growth under load. In Anahid et al. (2011), the cracks were prescribed an equilibrium crack size based on the analysis of a dislocation pileup by Stroh. Stroh’s theory predicts equilibrium crack sizes of the order $5 \mu\text{m}$ (Stroh, 1954).

A key aspect missing in all the aforementioned models is a micromechanically- and thermodynamically-consistent mathematical formulation, coupling dislocation plasticity and brittle damage, under dynamic loading conditions and for large strains. Even the brittle damage response incorporating the mechanism of dislocation-induced crack nucleation under dynamic loading conditions has not been presented elsewhere. State of the art brittle damage models predict an increasing failure strain with increasing strain rate (Ayyagari et al., 2018), which is contradictory to the mechanical response of beryllium. Additionally, the ratio of compressive to tensile failure stress of beryllium (in the range 2-3) cannot be explained using the brittle-damage models alone.

We present a finite deformation, viscoplastic, anisotropic damage model for evolution of inelastic deformation based on the physical mechanisms of dislocation-density evolution and subsequent cracking-induced failure based on the micro-mechanics of dislocation-mediated crack nucleation. The interaction between dislocation density and crack nucleation is facilitated by a kinetics law for the growth of cracks. The brittle failure model is from Ayyagari et al. (2018), which developed expressions for inelastic strain and degraded stiffness applicable for a three-dimensional stress state. The viscoplastic model is that used by Austin and McDowell (2011) and Follansbee and Kocks (1988). In order to understand the contributions of dislocation evolution and subsequent damage evolution to the dynamic failure strength, we apply the model to hot-pressed polycrystalline Beryllium. We calibrated the model to uniaxial stress response obtained from Split-Hopkinson Pressure Bar (SHPB) experiments (Blumenthal et al., 1998), and performed calculations under a variety of temperatures and strain rates to understand the kinetics of viscoplastic damage. We present original results based on the coupling between the kinetics of viscoplastic deformation and the kinetics of damage, and our results for the first time explain the brittle to ductile transition under both loading rate and temperature changes. In addition, our results show the dependence of failure stress and failure strain on grain size.

3. Kinematics of finite deformation for polycrystalline plasticity and damage

This work advances a framework of finite strain, polycrystalline, elastoplasticity and damage theory proposed by Clayton and McDowell (2003). The introduction of

an incompatible deformation tensor makes their framework more suitable for an element with local lattice distortions, e.g. due to geometrically necessary dislocations, which are precluded from the homogeneous theory of plastic deformation (Clayton et al., 2014).

The fundamental unit for averaging is a Statistical Volume Element (SVE). The SVE consists of several grains of a polycrystalline material, crystalline defects such as dislocations, and damage entities such as voids and cracks. The characteristic distributions of grains, dislocations, and damage entity measures in an SVE are statistical realizations of their respective *parent distributions*. The parent distribution in this context is an idealized outcome (e.g. probability density function) representing a large number of measures (e.g. grain size, crack length), where the random effects of the measures do not change.

Under an external load, the damage entities may evolve. In addition, the region of a material that precludes damage entities may exhibit plastic deformation owing to dislocation motion. Specific to this work, the stress field due to dislocation plasticity is assumed homogeneous. This is a reasonable assumption because the length scale associated with the homogenization of deformation due to dislocations is smaller compared with the size of damage entities, such as cracks.

Mesoscopic (i.e. local) coordinates within an SVE in the reference configuration \mathcal{B}_0 and the current configuration \mathcal{B} are indicated with \mathbf{X} and \mathbf{x} , respectively, with the mesoscopic motion denoted by $\mathbf{x} = \phi(\mathbf{X}, t)$, where t denotes time. We use a capitalized letter to represent a variable in the reference configuration, and a small letter without any overhead script to represent a variable in the current configuration. Two intermediate configurations are introduced: $\tilde{\mathcal{B}}$ with coordinates $\tilde{\mathbf{x}}$, and $\bar{\mathcal{B}}$ with coordinates $\bar{\mathbf{x}}$, for plastic deformation map and damage map between the reference and current configurations, respectively. Time derivative of a variable is indicated using an overhead script *dot*, e.g. time derivative of current material density is $\dot{\rho}_c$. Kinematic and kinetic variables in configurations $\bar{\mathcal{B}}$ and $\tilde{\mathcal{B}}$ are represented using overhead scripts $\bar{\cdot}$ and $\tilde{\cdot}$, respectively; these variables are either capitalized or denoted using small letters depending on their Lagrangian or Eulerian nature with respect to the deformation map involving an intermediate configuration. Subscripts are used throughout the manuscript to represent variables and constants. In order to avoid confusion between subscripts and Einstein's indicial notation, this manuscript does not use any tensor algebra using the indicial notation. Subscripts $(j), (k) \in [1, 2, \dots]$ are used as a counter for damage entities. A superscript T indicates a transpose. An algebraic dot product between vectors is denoted as $\mathbf{a} \cdot \mathbf{b}$ and a dyadic product between two vectors is denoted as $\mathbf{a} \otimes \mathbf{b}$. A product between two second-order tensors is $\mathbf{A} \cdot \mathbf{B} = \mathbf{AB}$ results in a second order tensor, where (\cdot) is omitted for

abbreviation. An inner product of two tensors is denoted as $\mathbf{A} : \mathbf{B}$ and results in a scalar. Product between a fourth order tensor \mathbb{C} and a second order tensor \mathbf{E} is denoted as $\mathbb{C}_{pqvw}E_{vu} = \mathbb{C} \cdot \mathbf{E}$. Product between two fourth-order tensors is denoted as $\mathbb{C}_{pqvw}\mathbb{S}_{vulm} = \mathbb{C} \cdot \mathbb{S}$. In the following section, macroscopic deformation tensors are defined as volume averages of mesoscopic tensors defined at locations within an SVE.

3.1. Macroscopic deformation

An SVE represents a continuum point in a macroscopic analysis. The macroscopic deformation gradient \mathbf{F} is specified in terms of motion of the external boundary of the SVE (Hill, 1972; Clayton and McDowell, 2003), i.e.,

$$\mathbf{F} = \frac{1}{V_0} \int_{S_0} \mathbf{x} \otimes \mathbf{N} dS_0, \quad (1)$$

where \mathbf{x} is mapping of a mesoscale point \mathbf{X} in the current configuration, V_0 is the total scalar volume of the SVE in the reference state, while S_0 is the external boundary surface of the SVE in the reference configuration, with corresponding unit outward normal \mathbf{N} in the reference configuration.

We consider the deformation of a body from initial reference configuration \mathcal{B}_0 to a current configuration \mathcal{B} , as shown in Figure 1. In general, the current configuration has K pairs of internal flaw faces for individual damage entities, i.e. crack faces, $\mathcal{S}_{(k)} \in \mathcal{B}_0$ where $(k) \in [0, 1, 2, 3, \dots, K]$. In the initial reference configuration, the damage is non-existent, and as such, $K = 0$. Under an external load, the body will undergo inelastic deformation, which in general is not isochoric. Nucleation of cracks occurs post loading, resulting in a finite pairs of internal flaw faces $K > 0$. The resulting displacement field will be discontinuous over flaw faces $\mathcal{S}_{(k)-}$ and $\mathcal{S}_{(k)+}$ and continuous in the remainder of the pristine material. In the current configuration, the total displacement field is considered as an additive decomposition of continuous and discontinuous displacement fields.

$$\mathbf{u} = \mathbf{x} - \mathbf{X} = \mathbf{u}_m + \sum_{(k)=0}^K \mathcal{H}_{\mathcal{S}_{(k)}} \llbracket \mathbf{u} \rrbracket_{\mathcal{S}_{(k)}}, \quad (2)$$

where \mathbf{X} is a material point in the reference configuration \mathcal{B}_0 . The subscript m indicates the continuous displacement field in the matrix, i.e. material precluding the damage entities. The global discontinuous displacement field is the sum of the jump in the displacements over individual flaw faces, represented as a spatial discontinuity

using the Heaviside step function $\mathcal{H}_{\mathcal{S}_{(k)}}$ and is defined as:

$$\mathcal{H}_{\mathcal{S}_{(k)}} = \begin{cases} 1, & \forall \mathbf{X} \in \mathcal{S}_{(k)+} \\ 0, & \forall \mathbf{X} \in \mathcal{S}_{(k)-}. \end{cases} \quad (3)$$

Assuming the displacement jump is constant over the flaw surface, we have $[[\mathbf{u}]]_{\mathcal{S}_{(k)}} = \mathbf{u}_{\mathcal{S}_{(k)+}} - \mathbf{u}_{\mathcal{S}_{(k)-}}$.

The deformation gradient tensor is obtained using an operation $\mathbf{F} = \mathbf{I} + \partial\mathbf{u}/\partial\mathbf{X}$ as follows:

$$\mathbf{F} = \mathbf{F}_m + \sum_{(k)} \delta_{\mathcal{S}_{(k)}} ([[\mathbf{u}]])_{\mathcal{S}_{(k)}} \otimes \mathbf{N}_{(k)} = \mathbf{F}_m + \mathbf{H}_d, \quad (4)$$

where $\delta_{\mathcal{S}_{(k)}}$ is the Dirac-delta function active on the $(k)^{th}$ pair of flaw surfaces, \mathbf{I} is the second-order identity tensor, $\mathbf{F}_m = \mathbf{I} + \nabla\mathbf{u}_m$ is second order tensor that characterizes contribution from the matrix material, i.e. elastoplasticity within the grains, $\mathbf{N}_{(k)}$ is the normal to the flaw surfaces $\mathcal{S}_{(k)+}$ and $\mathcal{S}_{(k)-}$. The displacement discontinuity specific to this work is due to the presence of the cracks in the solid. \mathbf{H}_d is a second order tensor map between reference \mathcal{B}_0 and current \mathcal{B} configurations and characterizes the contribution of local damage, i.e. internal surfaces of cracks and voids. The damage entities in Eq. (4) are not confined to the grains, and could traverse grain boundaries. Eq. (4) is consistent with Clayton and McDowell (2003), in which an additive decomposition was obtained by applying the generalized Gauss's theorem to the overall deformation gradient on the outer boundary of an SVE.

In general, with a length distribution and an orientation distribution of cracks and a variable displacement jump across crack faces, the contribution to homogenized deformation gradient from a distribution of cracks is given by Kachanov (1980) (for derivation of this expression, see Clayton and McDowell (2003) and references therein)

$$\mathbf{H}_d = \frac{1}{V_0} \sum_{(k)} \int_{{}^s S_0} [[\mathbf{u}]] \otimes {}^s \mathbf{N}_{(k)} dS_{0(k)}. \quad (5)$$

Note, we have dropped the suffix $\mathcal{S}_{(k)}$ for clarity. ${}^s S_0$ is a crack surface, a subset of the total surface S_0 . The total number of crack surface pairs in the material may change to accommodate new cracks that nucleate in the material undergoing deformation.

A multiplicative decomposition of the total macroscopic deformation gradient into a macroscopic elastic part (\mathbf{F}_e) and a total residual part is adopted (Clayton and McDowell, 2003). The total residual deformation gradient is given by $(\mathbf{F}_e)^{-1}\mathbf{F}$. The inverse of macroscopic elastic deformation is responsible for unloading of the

SVE from \mathcal{B} to $\bar{\mathcal{B}}$ and accounts for recoverable elastic deformation of the matrix and rearrangement of damage entities after macroscopic elastic unloading. However, this macroscopic elastic unloading retains the local residual strain in the matrix, allowing a rearranged damage entity to remain compatible with the local matrix in the vicinity of the damage entity.

The local residual elastic deformation emerges as a *meso-incompatible* deformation gradient on a macroscopic SVE (Clayton and McDowell, 2003). We use $\bar{\mathbf{F}}_i$ to denote the meso-incompatible deformation gradient tensor. Examples of such local deformations include heterogeneous elastoplastic deformation due to geometrically necessary dislocations, incomplete closing of cracks due to friction upon load removal, and local elastic stretch fields due to crystalline defects, such as intersecting twins. The matrix deformation gradient is then a combination of reversible elastic, residual elastic, and residual plastic deformation gradients:

$$\mathbf{F}_m = \mathbf{F}_e \bar{\mathbf{F}}_m = \mathbf{F}_e \bar{\mathbf{F}}_i \tilde{\mathbf{F}}_p, \quad (6)$$

where $\tilde{\mathbf{F}}_p$ is a homogenized plastic deformation in the matrix.

3.2. Definition of Damage

Combining Eqs. (4) and (6) results in following equation for the macroscopic deformation gradient:

$$\mathbf{F} = \mathbf{F}_e \bar{\mathbf{F}}_i \tilde{\mathbf{F}}_p + \mathbf{H}_d, \quad (7)$$

where \mathbf{H}_d is given by Eq. (5).

Next, we define $\bar{\mathbf{H}}_d$ between intermediate configurations $\tilde{\mathcal{B}}$ and $\bar{\mathcal{B}}$ as

$$\begin{aligned} \bar{\mathbf{H}}_d &= (\mathbf{F}_e)^{-1} \mathbf{H}_d (\tilde{\mathbf{F}}_p)^{-1}, \\ &= (\mathbf{F}_e)^{-1} \left[\frac{1}{V_0} \sum_{(k)} \int_{sS_0} [[\mathbf{u}]] \otimes {}^s \mathbf{N}_{(k)} dS_{0(k)} \right] (\tilde{\mathbf{F}}_p)^{-1}, \\ &= \frac{1}{\tilde{V}} \sum_{(k)} \int_{sS_0} [[\bar{\mathbf{u}}]] \otimes {}^s \tilde{\mathbf{n}}_{(k)} d\tilde{S}_{(k)}. \end{aligned} \quad (8)$$

where the push-forward of a normal is given by Nanson's formula

$$\tilde{\mathbf{n}} d\tilde{S} = \frac{\tilde{V}}{V_0} \tilde{\mathbf{F}}_p^{-T} \mathbf{N} dS_0, \quad (9)$$

while the elastic pull-back of the displacement jump is $[[\bar{\mathbf{u}}]] = (\mathbf{F}_e)^{-1} [[\mathbf{u}]]$, and the

elastic pull back of a spatial vector is $\bar{\mathbf{x}} = (\mathbf{F}_e)^{-1}\mathbf{x}$. Using Eq. (8), Eq. (7) now takes the following form:

$$\mathbf{F} = \mathbf{F}_e[\bar{\mathbf{F}}_i + \bar{\mathbf{H}}_d]\tilde{\mathbf{F}}_p = \mathbf{F}_e\bar{\mathbf{F}}_d\tilde{\mathbf{F}}_p. \quad (10)$$

Eq. (10) successfully provides a kinematic framework for accommodating residual elastic deformation ($\bar{\mathbf{F}}_i$), recoverable elastic deformation (\mathbf{F}_e), residual plastic deformation ($\tilde{\mathbf{F}}_p$), and anisotropic damage due to cracks ($\bar{\mathbf{H}}_d$). The plastic deformation precedes the damage deformation, and this sequence in multiplicative decomposition of deformation gradient is consistent with physical aspects of plastic deformation preceding dislocation-mediated nucleation of cracks.

In this work, we impose an assumption $\bar{\mathbf{F}}_i = \mathbf{I}$, i.e. the weighted volume average of the residual elastic deformation in $\bar{\mathcal{B}}$ vanishes. Crystal plasticity simulations can be used to quantify the meso-incompatibility deformation gradient, arising from mismatch of strains in the neighboring grains (Clayton and McDowell, 2003). Such simulations incorporating polycrystalline microstructure have the capability to simulate inhomogeneous plastic response. In other words, the plastic strain field from such simulations is inherently nonuniform (plastic strain is dependent on the position). On the other hand, models of the type that are limited to homogeneous plastic deformation (e.g. incorporating isotropic plasticity and lack of microstructure) are unable to simulate residual strains arising from strain incompatibility. Hence, in order to be consistent with our previous assumption of homogeneous plastic deformation $\bar{\mathbf{F}}_i = \mathbf{I}$ follows. Eq. (10) simplifies to the following form:

$$\mathbf{F} = \mathbf{F}_e[\mathbf{I} + \bar{\mathbf{H}}_d]\tilde{\mathbf{F}}_p, \quad (11)$$

where $[\mathbf{I} + \bar{\mathbf{H}}_d]$ is the deformation gradient due to cracks. $\bar{\mathbf{H}}_d$ is a *damage tensor* and characterizes the contribution of cracks to the overall deformation gradient. Note, for an individual crack the contribution to the damage tensor from various elastic loads (e.g. modes I, II, and III) is additive since the crack opening displacements (corresponding to individual elastic loads) are additive.

A comment on the nature of $\bar{\mathbf{H}}_d$ is in order. For cracks that open under remote tension loading, the crack opening displacements recover to their initial configuration upon unloading to zero stress. So, if the cracks were initially closed, then upon removal of the load they will go back to the closed configuration. Wing cracks under compression, however, in general do not recover their crack opening displacements upon complete unloading. This is because the shear stress required to drive the relative crack sliding has to overcome frictional forces. During unloading, the shear stress may be insufficient for complete crack closure. As such, compression of the

wing cracks generally leads to residual damage after unloading. Thus, $\bar{\mathbf{H}}_d$ represents residual damage. The amount of residual damage will depend on the stress path for loading and unloading, in addition to the material properties and the kinematics.

From (Kachanov, 1980; Grechka and Kachanov, 2006), the Lagrangian strain corresponding to the deformation gradient $\bar{\mathbf{F}}_d$ solely due to planar cracks in tension (opening), after excluding the higher order term for crack-crack interactions, is given (in $\tilde{\mathcal{B}}$ configuration) by

$$\tilde{\mathbf{E}}_d = \frac{1}{2\tilde{V}} \sum_{(k)} \int_{s_{S_0}} \{ [[\tilde{\mathbf{u}}]] \otimes {}^s\tilde{\mathbf{n}}_{(k)} + {}^s\tilde{\mathbf{n}}_{(k)} \otimes [[\tilde{\mathbf{u}}]] \} d\tilde{S}_{(k)}. \quad (12)$$

This expression is consistent with Lagrangian strain due to cracks evaluated using $(\bar{\mathbf{F}}_d^T \bar{\mathbf{F}}_d - \mathbf{I})/2$, where $\bar{\mathbf{F}}_d = (\mathbf{I} + \bar{\mathbf{H}}_d)$, after ignoring the higher order terms.

A special case of the damage tensor is obtained when the crack face displacement is along the normal to the crack surface, i.e. $[[\tilde{\mathbf{u}}]] = \bar{u} {}^s\tilde{\mathbf{n}}_{(k)}$. Assuming a stochastic distribution of penny-shaped cracks, the description of the damage tensor for this special case is given by (Grechka and Kachanov, 2006; Park and Voyiadjis, 1998; Murakami, 1983)

$${}^s\bar{\Omega}_d = \eta \sum_{(k)} g(s_{(k)}) r({}^s\tilde{\mathbf{n}}_{(k)}) (s_{(k)})^3 [{}^s\tilde{\mathbf{n}}_{(k)} \otimes {}^s\tilde{\mathbf{n}}_{(k)}], \quad (13)$$

where $s_{(k)}$ is the characteristic length of a penny-shaped crack having a normal ${}^s\tilde{\mathbf{n}}_{(k)}$ for the (k) individual cracks, η is the crack density per unit volume, $g(s_{(k)})$ is the crack-length probability distribution function, and $r({}^s\tilde{\mathbf{n}}_{(k)})$ is the crack-orientation probability distribution function. The half-length of the penny-shaped crack is often used as the characteristic length in damage calculations. ${}^s\tilde{\mathbf{n}}_{(k)}$ is a push-forward of normal in the reference configuration, ${}^s\mathbf{N}_{(k)}$, through $\tilde{\mathbf{F}}_p$. Eq. (13) assumes the opening displacement $[[\tilde{\mathbf{u}}]]$ is constant over a crack surface and \bar{u} is proportional to the characteristic crack length. Eq. (13) has been used to describe the behavior under compression by accounting for additional contribution from wing-crack length and orientation distributions (Hu et al., 2015).

For an isotropic description of damage, one may consider an equiaxial orientation distribution of evolving cracks having same length. This results in a scalar representation of damage given by (Paliwal and Ramesh, 2008)

$${}^s\bar{\Omega}_d = \eta \sum_{(k)} (s_{(k)})^3. \quad (14)$$

An approach to modeling failure using a scalar damage as an internal variable has often considered the limiting value of damage ${}^s\bar{\Omega}_d = 1$ to interpret complete failure. For a tensorial based damage measure, the limiting value for the trace of damage tensor commonly adopted is unity (Hu et al., 2015). The stress in the material may approach its strength well below this limiting value. For example, compression experiments on AlON ceramic (Paliwal et al., 2006) indicate $\text{trace}({}^s\bar{\Omega}_d) \approx 0.12$ at the time of the peak stress. However, it should be noted that this measure (in Eq. (13)) does not account for relative displacement between the crack faces as does the damage deformation tensor. Moreover, a scalar measure may over-predict damage in the direction perpendicular to the oriented-crack normals.

3.3. Kinematics in intermediate configurations

At this point, it is instructive to elaborate on the expression for mechanical energy. The stress-power per unit mass (\mathcal{P}) involves a stress measure and a kinematic measure, referred to as stress-power conjugate pairs, and in the current configuration \mathcal{B} is given by

$$\mathcal{P} = \frac{\boldsymbol{\sigma} : \mathbf{l}}{\rho_c} = \frac{\boldsymbol{\sigma} : \mathbf{d}}{\rho_c} \quad (15)$$

where ρ_c is the material density in the current configuration, $\mathbf{l} = \mathbf{d} + \mathbf{w}$ is expressing the velocity gradient in terms of symmetric part \mathbf{d} and the skew-symmetric part \mathbf{w} , and further, taking note of the identity that an inner product of a symmetric tensor $\boldsymbol{\sigma}$ with a skew-symmetric tensor \mathbf{w} is a null tensor. It is instructive to obtain representations of stress-power in the intermediate configuration using pull-back of stress and pull-back of velocity gradient in $\bar{\mathcal{B}}$:

$$\mathcal{P} = \frac{[\bar{\mathbf{C}}_e \bar{\mathbf{S}}] : \bar{\mathbf{l}}}{\bar{\rho}} = \frac{[\bar{\mathbf{C}}_e \bar{\mathbf{S}} \bar{\mathbf{C}}_e] : \bar{\mathbf{d}}}{\bar{\rho}}, \quad (16)$$

where $\bar{\rho}$ is the density in the elastically unloaded configuration, $\bar{\mathcal{B}}$. The role of $\bar{\mathbf{C}}_e$ as a *metric* appears in the elastically unloaded intermediate configuration. A *metric* is a second order covariant tensor that is used to defined the scalar product of contravariant vectors and is also used for raising and lowering indices and defining products in differential geometry (Clayton et al., 2005). Further, the product $\bar{\mathbf{C}}_e \bar{\mathbf{S}} = \bar{\mathbf{M}}$ is often referred to as the Mandel stress and is a two-point tensor. Thus, in the elastically unloaded configuration the Mandel stress is a conjugate of velocity gradient, while $\bar{\mathbf{M}} \bar{\mathbf{C}}_e$ is a conjugate of symmetric part of the velocity gradient defined as

$$\bar{\mathbf{d}} = \mathbf{F}_e^T \mathbf{d} \mathbf{F}_e = \frac{1}{2} (\bar{\mathbf{C}}_e \bar{\mathbf{l}} + \bar{\mathbf{l}}^T \bar{\mathbf{C}}_e), \quad (17)$$

where the pull-back of the velocity gradient is $\bar{\mathbf{l}} = \mathbf{F}_e^{-1} \mathbf{l} \mathbf{F}_e$.

Next, we obtain representations of stress-power in the elastic and damage unloaded intermediate configuration using pull-back of stress and pull-back of velocity gradient in $\tilde{\mathcal{B}}$:

$$\mathcal{P} = \frac{[\tilde{\mathbf{C}}_{ed} \tilde{\mathbf{S}}] : \tilde{\mathbf{l}}}{\tilde{\rho}} = \frac{[\tilde{\mathbf{C}}_{ed} \tilde{\mathbf{S}} \tilde{\mathbf{C}}_{ed}] : \tilde{\mathbf{d}}}{\tilde{\rho}}, \quad (18)$$

where $\tilde{\rho}$ is the material density in the elastic and damage unloaded configurations, $\tilde{\mathcal{B}}$. The role of $\tilde{\mathbf{C}}_{ed} = \mathbf{F}_d^T \mathbf{F}_e^T \mathbf{F}_e \mathbf{F}_d$ as a *metric* in the elastic and damage unloaded intermediate configuration becomes clear. Further, we identify $\tilde{\mathbf{C}}_{ed} \tilde{\mathbf{S}} = J_d \mathbf{F}_d^T \bar{\mathbf{M}} \mathbf{F}_d^{-T} = \tilde{\mathbf{M}}$ as the pull-back of the Mandel stress from $\tilde{\mathcal{B}}$, where $J_d = \det(\mathbf{F}_d)$. Note, even in this configuration ($\tilde{\mathcal{B}}$), the pull-back of Mandel stress is the conjugate of the velocity gradient, while $\tilde{\mathbf{M}} \tilde{\mathbf{C}}_{ed}$ is a conjugate of symmetric part of the velocity gradient defined as

$$\tilde{\mathbf{d}} = \mathbf{F}_d^T \bar{\mathbf{d}} \mathbf{F}_d = \frac{1}{2} (\tilde{\mathbf{C}}_{ed} \tilde{\mathbf{l}} + \tilde{\mathbf{l}}^T \tilde{\mathbf{C}}_{ed}), \quad (19)$$

where the pull-back of the velocity gradient is $\tilde{\mathbf{l}} = \mathbf{F}_d^{-1} \bar{\mathbf{l}} \mathbf{F}_d$.

Aforementioned definitions for the rates of deformation can be used to arrive at the contributions of elastic, plastic, and damage rate of deformation in the intermediate configurations. Expressions of these kinematic measures are included in Appendix 1.

4. Micromechanics and continuum descriptions of deformation and damage

4.1. Dislocation-based plasticity

Metal plasticity involving large inelastic strains is accomplished by the mechanisms of dislocation motion and dislocation density evolution. While the rate of plastic strain is attributed to the motion of mobile dislocations (ρ_M), the various stages of hardening (Rollett and Kocks, 1993) are accomplished by the mobile as well as the immobile (ρ_I) dislocation densities and their evolution.

The onset of plastic flow in a single crystal is attributed to the motion of initial density of mobile dislocations in the Stage I hardening regime, known as *free glide*, schematically shown in Fig. 2. The Orowan equation relates the rate of plastic strain to the mobile dislocation density, through the Burgers vector and dislocation velocity. The interaction of moving dislocations with themselves and the immobile dislocations leads to further evolution of the mobile as well as immobile dislocation densities, referred to as Stage II hardening. Overcoming the barriers to motion, such as those due to the Peierl's stress, precipitates, and the entanglements with

the immobile (forest) dislocations necessitates an increase in the flow stress. The fundamental relationship for flow stress in this regime is the Taylor equation. The theory for the evolution of dislocation density in this stage assumes that the length of dislocation stored per unit strain is proportional to the reciprocal of the mean free path between existing dislocations. Dislocation cells begin to form in this stage of work hardening.

A growing dislocation cluster eventually limits the value of the dislocation density to a saturation value (Oudriss and Feaugas, 2016). This process is characterized by a nonlinear decrease in the flow stress, termed as the Stage III hardening. The saturation stress is identified by formation of a well-defined cellular structure, where the cell walls are composed of relatively dense dislocation tangles. The average size of these dislocation cells decreases with increasing dislocation density. The mechanism of dislocation motion through cross-slip is assumed to operate in this stage, enabling the follow-on mechanism of dislocation annihilation. Concurrently, the increasing flow stress results in stored dislocations being able to break through the barriers, leaving behind dislocation debris. This debris is composed of dislocation dipoles and loops, in addition to dislocation monopoles, which are usually arranged in tangles or cell walls.

Further accommodation of plastic strain requires that the mobile dislocations glide through the substructure composed of dislocation cell walls. The cell walls have a density of dislocation that is an order of magnitude larger than that measured inside the cells. With increase in the plastic strain the dislocation cell size and the thickness of the cell walls become smaller, which may cause the saturation stress to rise, resulting in Stage IV hardening. When the resistance of the flow stress against further plastic strain becomes sufficiently large, material instabilities (such as formation of cracks and shear bands) may nucleate and grow at numerous sites, resulting in progressive increase of damage and material failure.

The mathematical theory of dislocation-based plasticity is well established. The isotropic form of the theory for dislocation-based plasticity implemented in our model is provided in Appendix 2. We make an approximation of linear elasticity for micromechanical solutions, despite nonlinear aspects of the macroscopic framework. Next, we elaborate on the dislocation evolution expressions that are specific to our work.

The evolution of dislocation density is specified according to mechanisms observed in molecular dynamics simulations and experimental observations. These mechanisms include dislocation multiplication ($\dot{\rho}_{mult}$) as a consequence of interaction between mobile dislocations (ρ_M) and immobile dislocations (ρ_I); the annihilation of oppositely signed dislocations and grain boundaries acting as dislocation sink,

($\dot{\rho}_{ann}$); immobilization of dislocations that encounter obstacles ($\dot{\rho}_{trap}$); and recovery mechanisms due to cross-slip and climb, which further assist in dislocation annihilation ($\dot{\rho}_{rec}$). Homogeneous dislocation nucleation is commonly considered under shock loading conditions, but has not been confirmed for strain rates below 10^4 s^{-1} . Since we are not considering loading conditions above 10^4 s^{-1} , we have chosen to neglect this nucleation term. The evolution equations for the time-rate of dislocation densities can be expressed as follows (Johnston and Gilman, 1960; Kocks, 1966; Estrin and Kubin, 1986; Roters et al., 2000; Austin and McDowell, 2011)

$$\begin{aligned}\dot{\rho}_M &= \dot{\rho}_{mult} - \dot{\rho}_{ann} - \dot{\rho}_{trap}, \\ \dot{\rho}_I &= \dot{\rho}_{trap} - \dot{\rho}_{rec},\end{aligned}\tag{20}$$

where the subscripts *mult*, *ann*, *rec* and *trap* refer to the dislocation multiplication, annihilation, recovery, and trapping, respectively.

Based on the physically based framework of (Ma and Roters, 2004; Austin and McDowell, 2011), the processes of dislocation addition and removal are given by following equations:

$$\begin{aligned}\dot{\rho}_{mult} &= \alpha_{mult}\rho_M\bar{v} \\ \dot{\rho}_{ann} &= \alpha_{ann}b\rho_M^2\bar{v}, \\ \dot{\rho}_{trap} &= \rho_M\bar{v}/\bar{\Lambda}, \\ \dot{\rho}_{rec} &= \beta_{rec}b\rho_I\rho_M\bar{v},\end{aligned}\tag{21}$$

where α_{mult} is a multiplication coefficient and α_{ann} is an annihilation coefficient related to the number of active slip systems and the capture distance within which the mobile dislocations annihilate each other or get absorbed within the grain boundaries. The effective mean free path of statistical trapping, $\bar{\Lambda}$, may be written based on the spacing between immobile dislocation density and the average grain size (\bar{d}) as an harmonic average,

$$\frac{1}{\bar{\Lambda}} = \beta_{trap}\sqrt{\rho_I} + \frac{1}{\bar{d}},\tag{22}$$

where β_{trap} is a trapping coefficient dependent on the immobile dislocation network and grain boundaries acting as obstacles to dislocation motion. Finally, β_{rec} is a recovery coefficient, calculated from saturation dislocation density (Oudriss and Feaugas, 2016). Note, the grain size has an inverse effect on the rate of trapping dislocation density. As such, smaller grain size will lead to a higher yield stress. Expressions in Eq. (21) have been developed over the last several decades, and readers are referred to Austin and McDowell (2011) for the dislocation-dynamics based rationale behind the forms of those expressions.

We elaborate on the form of the expression for immobile dislocation generation $\dot{\rho}_{trap}$. Dislocations are generated by activated dislocation sources, e.g. Frank-Read sources, grain boundaries. A new dislocation is generated when the previous dislocation has moved away from the source to decrease the back stress on the dislocation source. The multiplier β_{trap} indicates the density of activated dislocation sources (Davoudi and Vlassak, 2018).

At low strain rates, where thermally activated glide dominates the processes associated with dislocation multiplication, the trapping coefficient is commonly treated as rate insensitive (Austin and McDowell, 2011). However, from observations on deformation of FCC materials at high strain rates (above 1000 s^{-1}), the flow stress deviates from linear increase at low strain rates to a nonlinear increase at high rates. An explanation was proposed by Follansbee and Kocks (1988) for the strain rate dependence of the initial strain hardening rate based on the limiting dislocation velocity and average distance between obstacles. This supports the notion that there may exist a distribution of activation stresses for dislocation sources, as such, a greater density of dislocation sources is activated at higher strain rates. We thus allow for the trapping coefficient to be dependent on the rate, given by equation of the form

$$\beta_{trap} = c_4 \frac{\dot{\epsilon}_p}{\dot{\epsilon}_{0tp}} + c_5. \quad (23)$$

where $\dot{\epsilon}_{0tp} = 1 \text{ s}^{-1}$ is the reference strain rate for trapping and $\dot{\epsilon}_p$ is the uniaxial rate of plastic strain, related to the resolved rate of shear strain through the Taylor factor.

At the saturation stress, one can expect the immobile dislocation density to saturate. Equating the rate of immobile dislocations ($\dot{\rho}_I$) to zero, leads to the following expression for the recovery coefficient

$$\beta_{rec} = \frac{\beta_{trap}}{b\sqrt{\rho_{satI}}} + \frac{1}{bd\rho_{satI}}, \quad (24)$$

where ρ_{satI} is the saturation dislocation density for immobile dislocations, which may be modeled as both rate and temperature dependent (Beyerlein and Tomé, 2008). Further, the saturation dislocation density may be considered to be dependent on the temperature, similar to the consideration for saturation stress (Nes et al., 2000). Beryllium, for example, demonstrates profuse cross-slip above 523K (Taylor and Moore, 1964). In general, the probability of cross-slip per unit length of screw dislocations may be modeled using an expression of the Arrhenius form with an additional stress dependence (Rhee et al., 1998). However, due to lack of available

experimental data for calibrating the competing effect between dislocation generation and removal of immobile kind, including the rate- and temperature-dependence, we leave this development for the future work.

In addition to the saturation of the immobile dislocation, we impose a saturation for mobile dislocations. From measurements of dislocation density inside the cells by Oudriss and Feaugas (2016), we infer that the saturation of mobile dislocations occurs at approximately an order of magnitude smaller value compared to the saturation of immobile dislocations (within the dislocation cell walls). The saturation of mobile dislocation density is commonly modeled through an increased annihilation activity. Equating the rate of mobile dislocations ($\dot{\rho}_M$) without the trapping term ($\dot{\rho}_{trap}$) to zero, leads to the following expression for the annihilation coefficient of mobile dislocations

$$\alpha_{ann} = c_6 \frac{\alpha_{mult}}{b\sqrt{\rho_{satM}}}, \quad (25)$$

where ρ_{satM} is the saturation dislocation density for mobile dislocations. We assume a saturation limit for mobile dislocations as, $\rho_{satM} = 0.1\rho_{satI}$.

4.2. Dislocation-mediated crack nucleation

Several micromechanical theories of stress-induced cleavage cracking have been proposed for crystalline solids, e.g. Orowan, Zener, Argon-Orowan, and Cottrell [summarized by (Sarfarazi and Ghosh, 1987) and references therein]. We will adapt the theory developed by Stroh, with refinements for specific cases of dislocation mechanisms leading to Freidel-Stroh theory. Certain low-symmetry single crystal metals have a single predominant slip plane, which also acts as a cleavage plane. Example of such a metal is HCP beryllium with basal and prismatic planes favoring both slip and cleavage. Additionally, under large deformations, the dislocation cellular structure generated in Stage III hardening may favor crack nucleation (Pollock and Wilsdorf, 1983). Orowan suggested that when a wall of dislocation terminates inside a crystal, likely due to a barrier, the stress concentration at the terminated wall may develop stress intensity sufficient to nucleate a crack. Examples of such barriers include inclusions, a low-angle grain boundary, and a twin boundary.

Figure 3 shows a schematic of a dislocation pileup under an effective shear stress τ . The pileup formation can intensify the local stress, so that it becomes sufficient to nucleate a crack. According to an analysis by Stroh, which he later refined (Stroh, 1954, 1957), a crack will nucleate when sufficient dislocations have piled up on a slip plane under an effective shear stress. The pileup is instigated by an obstacle that renders the head of the pileup immobile by impinging on either a grain boundary, a slip band, or a precipitate/inclusion within the grain. A stress concentration created

at the head of the pileup instigates crack nucleation.

Following Eshelby et al. (1951), the number of dislocations in a pileup of length L_p under the action of an effective shear stress τ , holding the dislocation pileup in equilibrium on the pileup plane, is given by

$$n = \frac{\pi(1-\nu)L_p\tau}{bG}, \quad (26)$$

where G is the shear modulus.

The mode-I opening stress available for crack nucleation on an arbitrary plane making an angle ϕ_p with the pileup plane is (Smith and Barnby, 1967)

$$p_{22}^s = \frac{\tau}{2} \left(\frac{L_p}{r} \right)^{0.5} [3\sin\phi_p \cos(\phi_p/2)], \quad (27)$$

where γ_s is the crack surface energy, G is the shear modulus, and r is radial distance of a point from head of the pileup. Stroh found that the mode-I opening stress is at a maximum on plane $\phi_p = 70.5^\circ$, hence this plane has the highest likelihood to act as a Stroh crack plane.

An equilibrium analysis is invoked based on Griffith's energy criterion, the mode-I opening stress available on the plane for crack nucleation, and the stress near the tip of the pileup, which is held in equilibrium by an effective shear stress. The condition for crack nucleation is given as (Stroh, 1957)

$$\tau_c = \left[\frac{3\pi\gamma_s G}{8(1-\nu)L_p} \right]^{1/2}, \quad (28)$$

where γ_s is the crack surface energy.

Combining Eqs. (26) and (28), gives the condition for the number of dislocations in a pileup that will initiate nucleation of a Stroh crack (Stroh, 1957)

$$n_c = \left[\frac{3\pi^3(1-\nu)L_p\gamma_s}{8Gb^2} \right]^{0.5}. \quad (29)$$

In Figure 3, the pileup of length L_p nucleates a crack of length l on a plane $\phi_p = 70.5^\circ$. Considering a finite number of pileup dislocations contributing to the nucleation of the Stroh crack, the equilibrium length (l) of the Stroh crack is given by (Stroh, 1957)

$$l = \frac{n_c^2 b^2 G}{8\pi(1-\nu)\gamma_s}. \quad (30)$$

As an example, consider the material properties for Beryllium shown in Table 1. In this case, the number of dislocations in a pileup that will cause a Stroh crack to nucleate is ≈ 124 . The resulting equilibrium length of the Stroh crack is $\approx 5 \mu\text{m}$. The above solution is based on a planar configuration of the Stroh crack micromechanics and makes an approximation of linear elastic fracture mechanics, despite considerations of non-linearity in geometric and material aspects within the macroscopic framework.

A pileup force on the leading dislocation produces a local stress at the leading dislocation that is proportional to the product of the applied stress and the number of dislocations in the pileup (Anderson et al., 2017). Since the number of dislocations is proportional to the applied stress (Eq. (26)), the concentrated force is thus proportional to the square of the applied stress. Further, the square of the applied stress can be related to the dislocation density through the Taylor hardening relation, Eq. (122). We will use this dependence on the dislocation density to derive an expression for the stress intensity at the leading dislocation of the pile-up.

We attempted to reconcile the role of dislocation cell structure formation with the pileup model for crack nucleation. Observations of crack propagation in beryllium indicate that the formation of dislocation cell walls is a precursor to crack nucleation (Pollock and Wilsdorf, 1983). Further, the dislocation cell walls were identified as the preferred propagation pathway for a crack. We infer that the progressively increasing stress intensity within the cell wall is responsible for nucleating a crack. Although the exact spatial distribution of substructure dislocations in the cell wall is uncertain, we assume that a dislocation pileup model can be used to approximate the local stress within a cell wall, resulting in nucleation of a Stroh crack. Next, we obtained the number of dislocations in the pileup from the substructure (immobile) dislocation density.

The number of dislocations in a dislocation pileup (within a cell wall) is approximated from the homogenized immobile dislocation density (ρ_I) (Oudriss and Feaugas, 2016). Following (Nicolas et al., 2017), the number of dislocations intersecting a surface area S is $\rho_I S$. If Λ_{pu} is the average number of pileups over area S , then the average number of dislocations per pileup is $n_p = \rho_I / \Lambda_{pu}$. Let L_{ps} be the average spacing between the pileups, which we assume is related to the size of the structured dislocation cells. Based on analysis by Eshelby et al. (1951), the number of dislocations in a pileup is directly proportional to the grain size (Eq. (26)). The consequence of this dependence is reflected in the increase of failure strain with decreasing grain size (Greenspan, 1957; Terlinde et al., 1982). We assume the average grain size (\bar{d}) to influence the average pileup spacing through a harmonic average

with the length scale L_{ps} as follows

$$\frac{1}{\bar{L}_{ps}} = \frac{1}{L_{ps}} + \frac{1}{\bar{d}}. \quad (31)$$

where \bar{L}_{ps} is a harmonic average pileup spacing. The areal density of pileups is then given by $1/\bar{L}_{ps}^2$. The number of pileups intersecting the surface S is $\Lambda_{pu} = S/\bar{L}_{ps}^2$. An expression for the evolving number of dislocations per pileup (n_p) is given by

$$n_p = c_3 \bar{L}_{ps}^2 \rho_I, \quad (32)$$

where c_3 is a constant that can be calibrated with experimental data and controls when the onset of crack begins to have an impact on the stress-strain curve. This constant is essential because not all substructure dislocations may form pileups. L_{ps} may be obtained from microstructural observations of a recovered specimen. The spacing between dislocation pileups decreases with progressive plastic deformation. An average spacing of approximately $1.5 \mu\text{m}$ was measured by Pollock and Wilsdorf (1983) from failed samples of thin film beryllium. As a consequence, in our model the number of dislocations per pileup (n_p) evolves with ρ_I .

When the condition in Eq. (29) is satisfied, the stress intensity generated at the head of the dislocation pileup will nucleate a Stroh crack. The nucleated crack is then allowed to grow at a rate that is limited by the crack growth kinetics. As additional dislocations pileup, the evolving stress-intensity factor due to net slip on the pileup plane will continue to drive the growth of the Stroh crack.

The nucleated Stroh crack undergoes progressive load-induced growth following the kinetics of crack growth. Following Nemat-Nasser and Obata (1988) and Wong (1990), one can write the stress-intensity factor based on the slip displacement of the sliding plane. The mode I and mode II stress intensity factors at the tip of the Stroh crack due to n dislocations (for $n \geq n_c$) within a pileup are given using linear elastic fracture mechanics

$$K_I^s = \frac{4G}{\kappa + 1} \frac{n_p b \sin \phi_p}{\sqrt{2\pi(2s + l_z)}} + \sigma_{22}^s \sqrt{s\pi}, \quad (33)$$

and

$$K_{II}^s = \frac{4G}{\kappa + 1} \frac{n_p b \cos \phi_p}{\sqrt{2\pi(2s + l_z)}} + \sigma_{12}^s \sqrt{s\pi}, \quad (34)$$

where ϕ_p is the angle made by the pileup slip plane with the Stroh crack plane, σ_{22}^s and σ_{12}^s are the resolved normal and shear stress acting on the Stroh crack (see axes 1 and 2 in Fig. 3), respectively, and l is the length of the Stroh crack. κ takes

on values of $(3 - \nu)/(1 + \nu)$ in plane stress and $(3 - 4\nu)$ in plane strain. l_z is a length scale to regularize the stress intensity factor when the length of the Stroh crack approaches zero (similar to Nemat-Nasser and Obata (1988)), which we term the cohesive length. We choose a value for l_z to represent the length of the cohesive zone during homogeneous crack nucleation in a defect-free single crystal under plane strain conditions. This length scale represents a critical length of a stable crack nucleus, similar to the notion of nucleation of a stable partial dislocation loop that leaves in its wake an equilibrium stacking fault width (Daphalapurkar and Ramesh, 2012). The expression for the cohesive length is given by (Palmer and Rice, 1973),

$$l_z = \frac{9\pi}{32} \frac{2E\gamma_s}{(1 - \nu^2)\sigma_c^2}, \quad (35)$$

where $2\gamma_s$ is the Griffith fracture energy, σ_c is the critical stress (or strength) for homogeneous nucleation of a cleavage crack, and E is the isotropic elastic modulus.

We use the following fracture criterion under plane strain to assess whether the load-induced crack propagation is activated (Wong, 1990)

$$[(K_I^s)^2 + (K_{II}^s)]^{0.5} \geq (K_{IC}) \quad (36)$$

for a Stroh crack, where K_{IC} is the theoretical value of fracture toughness based on the creation of new surfaces, and excluding any energy dissipation associated with plastic deformation at the crack tip. In the absence of any additional energy dissipation at the crack tip, due to plastic deformation mechanisms, the minimum value of fracture toughness is $K_{IC} = [2\gamma_s E / (1 - \nu^2)]^{0.5}$, where γ_s is the crack surface energy. Note, the second term in Eqs. (33) and (34) is the contribution from the external load to the stress intensity factors.

For the Stroh crack tip under tension, we use the semi-analytic expression for the speed of a crack developed by (Freund, 1972; Huang and Subhash, 2003), given as

$$\dot{l} = \frac{c_r}{d_2} \left(\frac{K^s - K_{IC}}{K^s - 0.5K_{IC}} \right)^{d_1}, \quad (37)$$

where $K^s = [(K_I^s)^2 + (K_{II}^s)]^{0.5}$, while d_1 and d_2 are two empirical constants, which aid in calibration of the kinetics law specific to a material.

For a short Stroh crack, the first term in Eqs. (33) and (34) will have a dominant contribution, resulting in a stable crack growth with increasing load. At nucleation, the maximum hoop stress is on the plane $\phi_p = 70.5^\circ$ (Stroh, 1954).

As the Stroh crack grows, the second terms in Eqs. (33) and (34) will have in-

creasing contribution. The overall stress has an influence on the calculated tractions on the Stroh crack face. The growth of the Stroh crack results in growth of damage strain and material compliance, and these measures in turn alter the overall stress state. The speeds of the growing Stroh crack are dictated by the kinetics of crack growth, which also provides a measure of damping and limits the speed of crack propagation.

The model assumes a uniform orientation distribution of grains and a delta distribution for the grain size. In addition, we impose a uniform orientation distribution for the nucleated density of Stroh cracks. This simplifying assumption is made because of the lack of measurements on the orientation distribution of the Stroh cracks, and the appropriateness of this assumption will need to be assessed independently for different materials and loading conditions. In Section 5, we impose a restriction on the evolution of activated crack density based on the thermodynamics of processes.

Next, we implement the micromechanics of wing-crack growth to model the response of the nucleated Stroh crack to remote compression, (i.e. when $\sigma_{22}^s < 0$) which results in development of wing cracks.

4.3. Microcracking-based damage

Under external stress, the distributed Stroh cracks further exhibit opening or sliding on crack faces, contributing to inelastic deformation. Under global compression, sliding of the Stroh cracks may trigger nucleation and growth of two wing cracks, as shown in the schematic Figure 4. The wing crack is aligned along the maximum principal stress plane and at a finite angle with the Stroh crack. The rate of deformation due to damage is given by $\bar{\mathbf{d}}_d = \bar{\mathbf{F}}_d^{-T} \dot{\bar{\mathbf{E}}}_d \bar{\mathbf{F}}_d^{-1}$, where $\dot{\bar{\mathbf{E}}}_d$ is (time) rate of change of Lagrangian strain in $\tilde{\mathcal{B}}$.

The Lagrangian strain corresponding to sliding of the Stroh crack of length $2s$ and opening of two wing cracks of length l was given by Nemat-Nasser and Obata (1988) and was later generalized (for sliding displacement as a function of stress) by Liu and Graham-Brady (2016) (dropping the subscript (k))

$$\begin{aligned} \tilde{\mathbf{E}}_d = \sum_k \left\{ \frac{\eta}{2} [2s(\bar{\mathbf{u}}_{ls} \otimes \tilde{\mathbf{n}}_s + \tilde{\mathbf{n}}_s \otimes \bar{\mathbf{u}}_{ls}) \right. \\ \left. + 2\xi l(\bar{\mathbf{u}}_{ls} \otimes \tilde{\mathbf{n}}_l + \tilde{\mathbf{n}}_l \otimes \bar{\mathbf{u}}_{ls}) \right. \\ \left. + 2l(\bar{\mathbf{u}}_l \otimes \tilde{\mathbf{n}}_l + \tilde{\mathbf{n}}_l \otimes \bar{\mathbf{u}}_l)] \right\}. \end{aligned} \quad (38)$$

This expression is based on the superposition principle of displacement, where the crack opening displacement $\bar{\mathbf{u}}_{ls}$ is the load-induced average sliding displacement

on the Stroh crack face of length $2s$ in the direction of maximum shear; the Stroh crack face normal is $\tilde{\mathbf{n}}_s$; crack sliding also contributes to a proportional opening displacement $\xi \bar{\mathbf{u}}_{ls}$ of the wing crack with normal $\tilde{\mathbf{n}}_l$; $\bar{\mathbf{u}}_l$ is associated with the wing-crack opening displacement when the sliding crack face is assumed fixed; and η is the crack density. In the work of Nemat-Nasser and Obata (1988), ξ was approximated to be $\frac{1}{2}$.

In this work, we apply the wing-crack micromechanics advanced by Ayyagari et al. (2018) to model the development of a wing crack from sliding on the Stroh crack face. The increment in the Lagrange strain due to sliding on the Stroh crack of length $2s$ and opening of wing cracks of length l is given by (Ayyagari et al., 2018) (dropping the subscript (k))

$$\begin{aligned} \tilde{\mathbf{E}}_d = \sum_{(k)} \left\{ \frac{\eta}{2} s \varpi_3 \bar{u}_{ls} (\bar{\mathbf{s}}_\tau \otimes \tilde{\mathbf{n}}_s + \tilde{\mathbf{n}}_s \otimes \bar{\mathbf{s}}_\tau) \right. \\ + \frac{\eta}{2} s \varpi_4 \bar{u}_{ls} [(\boldsymbol{\xi} \cdot \bar{\mathbf{n}}_l) \otimes \tilde{\mathbf{s}}_\tau + \tilde{\mathbf{s}}_\tau \otimes (\boldsymbol{\xi} \cdot \bar{\mathbf{n}}_l)] \\ \left. + \frac{\eta}{2} s \varpi_5 [\boldsymbol{\zeta} \cdot (\bar{\mathbf{S}} \cdot \bar{\mathbf{n}}_l) \otimes \tilde{\mathbf{n}}_l + \tilde{\mathbf{n}}_l \otimes \boldsymbol{\zeta} \cdot (\bar{\mathbf{S}} \cdot \bar{\mathbf{n}}_l)] \right\}, \end{aligned} \quad (39)$$

where, η is the Stroh crack density per unit volume, \mathbf{s}_τ is the direction of maximum shear traction on the Stroh crack plane, $\bar{\mathbf{S}}$ is the far-field second Piola-Kirchhoff stress; $u_{ls} \mathbf{s}_\tau$ describes the Stroh crack sliding displacement as a function of stress and in the direction of maximum shear \mathbf{s}_τ , given by Ayyagari et al. (2018). Note, this sliding displacement is a constant in Nemat-Nasser and Obata (1988). $\boldsymbol{\zeta}$ is a symmetric second order alignment tensor. $\boldsymbol{\xi}$ is a second order transversely isotropic scaling tensor, \mathbf{n}_s is a unit vector normal to the sliding crack (Stroh crack), and \mathbf{n}_l is a unit vector normal to the wing crack. A rate-dependent brittle model incorporating a density of crack sizes was validated against data on basalt (Ayyagari et al., 2018).

An expression for the deformation gradient for the wing-crack micromechanics may be written as

$$\begin{aligned} \bar{\mathbf{F}}_d = \mathbf{I} + \sum_{(k)} \left\{ \eta s \varpi_3 \bar{u}_{ls} (\bar{\mathbf{s}}_\tau \otimes \tilde{\mathbf{n}}_s) \right. \\ + \eta s \varpi_4 \bar{u}_{ls} [(\boldsymbol{\xi} \cdot \bar{\mathbf{n}}_l) \otimes \tilde{\mathbf{s}}_\tau] \\ \left. + \eta s \varpi_5 [\boldsymbol{\zeta} \cdot (\bar{\mathbf{S}} \cdot \bar{\mathbf{n}}_l) \otimes \tilde{\mathbf{n}}_l] \right\}. \end{aligned} \quad (40)$$

Relative sliding of Stroh crack faces will contribute to the stress intensity factor

at the wing crack tip. The crack sliding displacement u_{l_s} follows:

$$\bar{u}_{l_s} = \frac{(\kappa + 1)(1 + \nu)}{\sqrt{2}E} \left[\bar{f}_w + \sigma_2^p \sqrt{l(l + l_z)} \frac{\pi}{\sin\phi_2} \left(1 - \frac{1}{\sqrt{2}} \right) \right], \quad (41)$$

where $\bar{f}_w = -2s\tau_{\text{eff}}$ is the wedging force on the Stroh cracks per unit length and σ_2^P is the maximum principal stress. Extrinsic coefficients ϖ_3 , ϖ_4 and ϖ_5 are an isotropic scaling for crack opening/sliding displacements. Through equivalence of force-driven and displacement driven stress intensity factors, Ayyagari et al. (2018) calculates

$$\varpi_3 = -2s \quad \varpi_4 = \pi \sqrt{l(l + l_z)} \left(1 - \frac{1}{\sqrt{2}} \right), \quad (42)$$

where $2s$ is length of the sliding Stroh crack, l is the wing crack length, and l_z is given by Eq. (35) in order to regularize stress intensity for zero wing-crack length (Nemat-Nasser and Obata, 1988). From energetic consideration (Ayyagari et al., 2018)

$$\varpi_5 = \frac{(\kappa + 1)(1 + \nu)}{2E} \pi l^2, \quad (43)$$

where G and ν are shear modulus and Poissons ratio, while $\kappa = (3 - \nu)/(1 + \nu)$ for plane stress and $\kappa = (3 - 4\nu)$ for plane strain assumptions for micromechanics. ξ is a second order transversely isotropic scaling tensor (Ayyagari et al., 2018) whose diagonal components are given by

$$\begin{aligned} \xi_{11} = \xi_{33} &= \frac{\sin(\alpha_2 + \phi_2)}{\sin\phi_2(\cos\alpha_2 - \mu_f \sin\alpha_2)}, \\ \xi_{22} &= \frac{-\cos(\alpha_2 + \phi_2)}{\sin\phi_2(\sin\alpha_2 + \mu_f \cos\alpha_2)}, \end{aligned} \quad (44)$$

where ϕ_2 is angle made by the wing-crack plane with the Stroh crack plane, $\alpha_2 \in [0, \pi/2]$ is the Euler angle made by the normal to the Stroh crack plane with the global Y-axis of the Cartesian co-ordinate system, $\theta_2 \in [0, 2\pi]$ is the (azimuthal) Euler angle made by the normal of the Stroh crack plane with the global X-axis in the XZ plane, and μ_f is a coefficient of friction on the Stroh crack plane. ζ is a

symmetric second order alignment tensor given by

$$\boldsymbol{\zeta} = \begin{bmatrix} \cos^2\theta_2 \sin^2(\alpha_2 + \phi_2) & 0.5 \cos\theta_2 \sin 2(\alpha_2 + \phi_2) & 0.5 \sin 2\theta_2 \sin^2(\alpha_2 + \phi_2) \\ & \cos^2(\alpha_2 + \phi_2) & 0.5 \sin\theta_2 \sin 2(\alpha_2 + \phi_2) \\ & \text{sym.} & \sin^2\theta_2 \sin^2(\alpha_2 + \phi_2) \end{bmatrix} \quad (45)$$

The choice of the functional form as presented in Eq. (39) can be attributed to contributions due to sliding, tension crack growth and a coupled effect.

The effective traction on the crack face τ_{eff} required to evaluate \bar{f}_w is given by

$$\tau_{\text{eff}} = -\tau_{\text{coh}} - \mu_f (\bar{\mathbf{n}}_s \cdot \bar{\mathbf{S}} \cdot \bar{\mathbf{n}}_s) + |\bar{\mathbf{s}}_\tau \cdot \bar{\mathbf{S}} \cdot \bar{\mathbf{n}}_s|, \quad (46)$$

where the first term is cohesive resistance in shear, the second term is the frictional resistance on the Stroh crack faces as a result of applied normal stress, and the third term is an absolute magnitude of the resolved shear stress on the crack faces that provides the driving force for sliding. The sliding on the Stroh crack in turn drives the growth of wing cracks.

The cohesive resistance in shear was interpreted by Nemat-Nasser and Obata (1988) as the resistance for plastic deformation at the sliding cracks, and in our case accounts for plastic deformation of the wedge at one end of the nucleated Stroh crack. In our work, we adapt the expression for cohesive strength from Nemat-Nasser and Obata (1988) and choose the cohesive resistance to be Peierls stress. The cohesive resistance is given by (Nemat-Nasser and Obata, 1988)

$$\tau_{\text{coh}} = \tau_{0\text{coh}} e^{|\bar{u}_{ls}| \eta_{\text{coh}}}, \quad (47)$$

where $\tau_{0\text{coh}}$ is the initial cohesion, η_{coh} is the decaying factor, and $|\bar{u}_{ls}|$ is the magnitude of crack sliding displacement. $|\bar{u}_{ls}|$ in Eq. (47) was calculated from the maximum magnitude of traction required for plastic deformation, i.e $\tau_{0\text{coh}}$.

Experiments by Nemat-Nasser (1985) offer evidence of wing-cracks from sliding even from inclusions and cavities of various geometric shapes. From their experiments, the wing cracks have managed to emanate from the flaws despite having irregular shaped flaw tips. Similar to the approach by Nemat-Nasser and Obata (1988), we consider the sliding crack model as a representative for our Stroh crack, which can slide after deforming plastically at the wedge.

In Eq. (41), the maximum principal stress component σ_2^p in the direction $\bar{\mathbf{n}}_l$ operating in the neighborhood of a flaw promotes wing-crack growth. Rewriting σ_2^p in terms of $\bar{\mathbf{S}}$ gives

$$\sigma_2^p = (\bar{\mathbf{n}}_l \cdot \bar{\mathbf{S}} \cdot \bar{\mathbf{n}}_l). \quad (48)$$

Under a compressive load, sliding commences when the frictional force acting on the Stroh crack faces is overcome by the effective shear stress on Stroh crack faces. If ϕ_2 is the angle made by the Stroh crack slip direction (\mathbf{P}) with the plane of the wing-crack, then the resulting stress intensity factors at the wing-crack tip are given by

$$\tilde{K}_I = \frac{-2s\tau_{\text{eff}} \sin\phi_2}{\sqrt{\pi(l+l_z)}} + \sigma_2^p \sqrt{\pi l}, \quad (49)$$

and

$$\tilde{K}_{II} = \frac{2s\tau_{\text{eff}} \cos\phi_2}{\sqrt{\pi(l+l_z)}}. \quad (50)$$

The second term in Eq. (49) accounts for the possibility of wing crack growth under remote tension, either due to the applied tensile load or due to the Poisson effect under remote compression. The growth of a wing crack is activated when the following condition is satisfied

$$[\tilde{K}_I^2 + \tilde{K}_{II}^2]^{0.5} \geq K_{IC}. \quad (51)$$

For the case of a crack tip under tension, the expression for the speed of the crack is based on the theoretical analysis of dynamically propagating crack by (Freund, 1972; Huang and Subhash, 2003)

$$i = \frac{c_r}{d_2} \left(\frac{\tilde{K}_I - K_{IC}}{\tilde{K}_I - 0.5K_{IC}} \right)^{d_1}. \quad (52)$$

This expression has two empirical constants (d_1 and d_2), which aid in calibration of the kinetics law specific to a material. In our model, the propagation of the wing crack is on the plane of maximum principal stress. The above solution is based on a planar configuration of the wing crack micromechanics and makes an approximation of linear elastic fracture mechanics, despite considerations of nonlinearity in geometric and material aspects within the macroscopic framework.

The presence of cracks influences the overall compliance matrix, resulting in an effective compliance of the material that is higher than the pristine material compliance. The compliance of the material given by Ayyagari et al. (2018) is composed of compliance from the cracks, in addition to the pristine material compliance. Further, their work proposed to use effective stress inside an isotropic inclusion that is embedded in an homogenized anisotropic damaged matrix (Hu et al., 2015). The effective stress in the inclusion was then used to find tractions on the crack plane

(a crack is within an inclusion) using a plane strain form of reduced stiffness tensor. These tractions within the crack plane were then employed to calculate the stress intensity factors at the tip of the Stroh crack and the wing crack. Essentially, the two-dimensional wing-crack micromechanics was generalized to handle three-dimensional stress states. Such an approach has the ability to account for the compliance of the damage matrix in calculating the stress intensity at the crack tip. In our work, we retain the overall framework as that of Hu et al. (2015) to calculate the effective tractions on the crack under plane strain conditions. However, the self-consistent approximation for damage anisotropy of the matrix in presence of large strain plasticity has not been rigorously validated to the best of our knowledge. As such, we do not account for the change in compliance of the damaged matrix in calculating the crack face tractions i.e. the matrix retains the stiffness properties of the medium as that in the initial configuration. Our resulting solution may be categorized as a *non-interaction approximation*. Under the non-interaction approximation, the predictions may remain sufficiently accurate at substantial concentrations of defects (Kachanov and Sevostianov, 2013).

The relationship between the traction \mathbf{T} on the sliding Stroh crack and the Stroh crack opening displacement $\bar{\mathbf{u}}$ is essential in establishing the increments in compliance due to damage. A general traction-displacement relationship that is applicable particularly to a planar wing-crack problem can be expressed as Grechka and Kachanov (2006):

$$\bar{\mathbf{u}} = \mathbf{Z} \cdot \mathbf{T} \quad (53)$$

where \mathbf{Z} is a second order crack compliance tensor that maps the crack opening displacement $\bar{\mathbf{u}}$ to the tractions \mathbf{T} . \mathbf{Z} can be defined in terms of decomposition along the local flaw basis $\hat{\mathbf{P}}$ and $\hat{\mathbf{N}}$ as:

$$\mathbf{Z} = Z_{pp}(\bar{\mathbf{s}} \otimes \bar{\mathbf{s}}) + Z_{pn}(\bar{\mathbf{s}} \otimes \bar{\mathbf{n}} + \bar{\mathbf{n}} \otimes \bar{\mathbf{s}}) + Z_{nn}(\bar{\mathbf{n}} \otimes \bar{\mathbf{n}}), \quad (54)$$

where $\bar{\mathbf{n}}$ is normal to the planar crack and $\bar{\mathbf{s}}$ is an in-plane vector to the planar crack.

Further, a scalar termed effective crack compliance factor is defined as

$$\bar{Z} = \frac{Z_{pp}Z_{nn} - Z_{pn}^2}{Z_{nn} + \mu Z_{pn}} \quad (55)$$

Under remote tension, it is commonly assumed that the brittle damage evolves through growth of cracks, without activation of wing-cracks. For a finite density of cracks, the increment in compliance due to the opening cracks was developed by

Grechka and Kachanov (2006).

$$\Delta\mathcal{S}_{ijkl} = \frac{8(1-\nu^2)}{3E(2-\nu)} (\Omega_{ik}\delta_{jl} + \Omega_{il}\delta_{jk} + \Omega_{jk}\delta_{il} + \Omega_{jl}\delta_{ik}) \quad (56)$$

where i, j, k, l are indicial notations to denote the components of the compliance, and Ω_{ij} are components of the second order tensorial representation of crack size and orientation distribution ${}^s\mathbf{\Omega}_d$, given by Eq. (13).

Under remote compression, it is commonly assumed that the brittle damage evolves through activation and growth of wing-cracks. Ayyagari et al. (2018) developed expressions for the increment in compliance due sliding on pre-existing cracks and subsequent growth of two wing-cracks, based on kinematic and energetic considerations. These expressions are given by:

$$\left. \begin{array}{lll} \Delta\mathcal{S}_{1111} = c_{\theta_2}^4 \Upsilon_1 & \Delta\mathcal{S}_{2211} = c_{\theta_2}^2 \Upsilon_4 & \Delta\mathcal{S}_{3311} = s_{\theta_2}^2 c_{\theta_2}^2 \Upsilon_1 \\ \Delta\mathcal{S}_{1122} = c_{\theta_2}^2 \Upsilon_3 & \Delta\mathcal{S}_{2222} = \Upsilon_2 & \Delta\mathcal{S}_{3322} = s_{\theta_2}^2 \Upsilon_3 \\ \Delta\mathcal{S}_{1133} = s_{\theta_2}^2 c_{\theta_2}^2 \Upsilon_1 & \Delta\mathcal{S}_{2233} = s_{\theta_2}^2 \Upsilon_4 & \Delta\mathcal{S}_{3333} = s_{\theta_2}^4 \Upsilon_1 \\ \Delta\mathcal{S}_{1123} = c_{\theta_2}^2 s_{\theta_2} \Upsilon_5 & \Delta\mathcal{S}_{2223} = s_{\theta_2} \Upsilon_6 & \Delta\mathcal{S}_{3323} = s_{\theta_2}^3 \Upsilon_5 \\ \Delta\mathcal{S}_{1113} = c_{\theta_2}^2 s_{2\theta_2} \Upsilon_1 & \Delta\mathcal{S}_{2213} = s_{2\theta_2} \Upsilon_4 & \Delta\mathcal{S}_{3313} = s_{\theta_2}^2 s_{2\theta_2} \Upsilon_1 \\ \Delta\mathcal{S}_{1112} = c_{\theta_2}^3 \Upsilon_5 & \Delta\mathcal{S}_{2212} = c_{\theta_2} \Upsilon_6 & \Delta\mathcal{S}_{3312} = s_{\theta_2}^2 c_{\theta_2} \Upsilon_5 \\ \Delta\mathcal{S}_{2311} = c_{\theta_2}^2 s_{\theta_2} \Upsilon_7 & \Delta\mathcal{S}_{1311} = c_{\theta_2}^3 s_{\theta_2} \Upsilon_1 & \Delta\mathcal{S}_{1211} = c_{\theta_2}^3 \Upsilon_7 \\ \Delta\mathcal{S}_{2322} = s_{\theta_2} \Upsilon_8 & \Delta\mathcal{S}_{1322} = s_{\theta_2} c_{\theta_2} \Upsilon_3 & \Delta\mathcal{S}_{1222} = c_{\theta_2} \Upsilon_8 \\ \Delta\mathcal{S}_{2333} = s_{\theta_2}^3 \Upsilon_7 & \Delta\mathcal{S}_{1333} = s_{\theta_2}^3 c_{\theta_2} \Upsilon_1 & \Delta\mathcal{S}_{1233} = s_{\theta_2}^2 c_{\theta_2} \Upsilon_7 \\ \Delta\mathcal{S}_{2323} = s_{\theta_2}^2 \Upsilon_9 & \Delta\mathcal{S}_{1323} = s_{\theta_2}^2 c_{\theta_2} \Upsilon_5 & \Delta\mathcal{S}_{1223} = s_{\theta_2} c_{\theta_2} \Upsilon_9 \\ \Delta\mathcal{S}_{2313} = s_{2\theta_2} s_{\theta_2} \Upsilon_7 & \Delta\mathcal{S}_{1313} = 2s_{\theta_2}^2 c_{\theta_2}^2 \Upsilon_1 & \Delta\mathcal{S}_{1213} = s_{\theta_2}^2 c_{\theta_2} \Upsilon_7 \\ \Delta\mathcal{S}_{2312} = s_{\theta_2} c_{\theta_2} \Upsilon_9 & \Delta\mathcal{S}_{1312} = s_{\theta_2} c_{\theta_2}^2 \Upsilon_5 & \Delta\mathcal{S}_{1212} = c_{\theta_2}^2 \Upsilon_9 \end{array} \right\} \quad (57)$$

where the scalar terms and the associated variables are defined in Table 1. Shorthand notations are $s_{\theta_2}^2 \equiv \sin^2(\theta_2)$, $c_{\theta_2}^2 \equiv \cos^2(\theta_2)$, and $s_{2\theta_2} \equiv \sin(2\theta_2)$.

Crack length is evolved based on Griffith's criterion (Griffith, 1920), which compares the stress intensity factor with a material's fracture energy. While the experimentally measured fracture toughness property takes into account the presence of plasticity around a crack tip, as explained by Irwin's modified criterion for fracture (Irwin, 1957), the Griffith's criterion for fracture excludes the plastic dissipation. Since plastic dissipation in our model has been accounted separately within the constitutive response, we choose the Griffith's criterion over Irwin's modified criterion for fracture initiation.

Table 1: Variables and their functional forms

Variable	Functional form
λ_1	$\mathbf{c}_{\alpha_2}/(\mathbf{c}_{\alpha_2} - \mu\mathbf{s}_{\alpha_2})$
λ_2	$\mathbf{s}_{\alpha_2}/(\mathbf{s}_{\alpha_2} + \mu\mathbf{c}_{\alpha_2})$
λ_3	$(\mathbf{c}_{\alpha_2} - \mu\mathbf{s}_{\alpha_2})/(\mathbf{s}_{\alpha_2} + \mu\mathbf{c}_{\alpha_2})$
ψ_1	$\left(\varpi_1\mathbf{s}_{\alpha_2}(\mathbf{c}_{\alpha_2} - \mu\mathbf{s}_{\alpha_2}) + \frac{\varpi_2}{\mathbf{s}_{\phi_2}}\mathbf{s}_{(\alpha_2+\phi_2)}^2 \right)$
ψ_2	$\left(\varpi_1\mathbf{c}_{\alpha_2}(\mathbf{s}_{\alpha_2} + \mu\mathbf{c}_{\alpha_2}) - \frac{\varpi_2}{\mathbf{s}_{\phi_2}}\mathbf{c}_{(\alpha_2+\phi_2)}^2 \right)$
ψ_3	$\left(\varpi_1(\mathbf{c}_{2\alpha_2} - \mu\mathbf{s}_{2\alpha_2}) + \frac{\varpi_2}{\mathbf{s}_{\phi_2}}\mathbf{s}_{2(\alpha_2+\phi_2)} \right)$
ψ_4	$\pi l^2/\sqrt{2}$
Υ_1	$\eta s\bar{Z} \left(\lambda_1\psi_1^2 + \psi_4\mathbf{s}_{(\alpha_2+\phi_2)}^4 \right)$
Υ_2	$\eta s\bar{Z} \left(\lambda_2\psi_2^2 + \psi_4\mathbf{c}_{(\alpha_2+\phi_2)}^4 \right)$
Υ_3	$-\eta s\bar{Z} \left(\lambda_1\psi_1\psi_2 - \psi_4\mathbf{s}_{(\alpha_2+\phi_2)}^2\mathbf{c}_{(\alpha_2+\phi_2)}^2 \right)$
Υ_4	$-\eta s\bar{Z} \left(\lambda_2\psi_1\psi_2 - \psi_4\mathbf{s}_{(\alpha_2+\phi_2)}^2\mathbf{c}_{(\alpha_2+\phi_2)}^2 \right)$
Υ_5	$\eta s\bar{Z} \left(\lambda_1\psi_1\psi_3 + \psi_4\mathbf{s}_{(\alpha_2+\phi_2)}^2\mathbf{s}_{2(\alpha_2+\phi_2)} \right)$
Υ_6	$-\eta s\bar{Z} \left(\lambda_2\psi_2\psi_3 - \psi_4\mathbf{c}_{(\alpha_2+\phi_2)}^2\mathbf{s}_{2(\alpha_2+\phi_2)} \right)$
Υ_7	$\frac{\eta}{2}s\bar{Z} \left(\psi_1 \left(\lambda_1\lambda_3\psi_2 - \frac{\lambda_2}{\lambda_3}\psi_1 \right) + \psi_4\mathbf{s}_{(\alpha_2+\phi_2)}^2\mathbf{s}_{2(\alpha_2+\phi_2)} \right)$
Υ_8	$-\frac{\eta}{2}s\bar{Z} \left(\psi_2 \left(\lambda_1\lambda_3\psi_2 - \frac{\lambda_2}{\lambda_3}\psi_1 \right) - \psi_4\mathbf{c}_{(\alpha_2+\phi_2)}^2\mathbf{s}_{2(\alpha_2+\phi_2)} \right)$
Υ_9	$\frac{\eta}{2}s\bar{Z} \left(\psi_3 \left(\lambda_1\lambda_3\psi_2 - \frac{\lambda_2}{\lambda_3}\psi_1 \right) + \psi_4\mathbf{s}_{2(\alpha_2+\phi_2)}^2 \right)$

In our model, the applied load evolves both the wing-crack length [Eq. (52)] and the Stroh crack length [Eq. (37)]. Their rate of growth will depend on resolved tractions on their respective crack planes and the resulting stress intensity factors. For the most part, models in the literature assume a pre-existing primary crack. The Stroh crack nucleation and growth in the present model is an extension of Ayyagari et al. (2018), which assumes a fixed primary crack length. Growth of a primary crack, in presence of the wing-crack, has been observed in experiments on rocks and are commonly referred as the secondary cracks or shear cracks (Einstein and Ghahreman, 1995). These secondary cracks grow under the shear mode (mode II) due to shear stress in the plane of the primary crack (Stokes et al., 1958; Park and Bobet, 2010).

5. Thermodynamics and balance laws

Conservation of mass in the current configuration is expressed by

$$-\frac{\dot{\rho}_c}{\rho_c} = \frac{\dot{J}}{J} = \text{trace}(\mathbf{l}) = \text{trace}(\mathbf{d}), \quad (58)$$

where ρ_c is the current material density, \mathbf{l} is the spatial velocity gradient, and $J = \det(\mathbf{F})$ is the Jacobian of deformation gradient tensor. The local form of balance of energy in the current configuration is

$$\rho_c \dot{U} = \boldsymbol{\sigma} : \mathbf{d} - \nabla \cdot \mathbf{q} + \rho_c r, \quad (59)$$

where $\boldsymbol{\sigma}$ is the symmetric Cauchy stress in the current configuration, U is the internal energy per unit mass, \mathbf{q} is the heat flux vector, r is the rate of energy supply/generation per unit mass, and $(\nabla \cdot)$ is a divergence operator. The local form of second law of thermodynamics, expressed by Clausius-Duhem inequality, is given by

$$\rho_c \dot{S} \geq -\nabla \cdot \left(\frac{\mathbf{q}}{\theta} \right) + \frac{\rho_c r}{\theta}, \quad (60)$$

where θ is the temperature and S is the entropy per unit mass. The internal dissipation rate per unit volume ($\rho_c D$) is the difference between $\rho_c \dot{S}\theta$ and the heat supply:

$$\rho_c \dot{D} = \rho_c \dot{S}\theta - (-\nabla \cdot \mathbf{q} + \rho_c r). \quad (61)$$

Further, one can obtain an alternate expression for dissipation rate \dot{D} by combining with the energy balance Eq. (59):

$$\rho_c \dot{D} = \boldsymbol{\sigma} : \mathbf{d} - \rho_c \dot{U} + \rho_c \dot{S} \theta. \quad (62)$$

Expanding the divergence term in Eq. (60) and using the Clausius-Duhem inequality, Eq. (61), the Clausius-Duhem inequality in the local form and in the current configuration can be written as (Scheidler and Wright, 2001)

$$\rho_c \dot{D} - \frac{\nabla \theta}{\theta} \cdot \mathbf{q} \geq 0, \quad (63)$$

where $\nabla \theta$ is a covariant derivative of temperature field with respect to spatial coordinates.

We define the specific Helmholtz energy, $\Psi(\bar{\mathbf{E}}_e, \theta, \eta, \rho, 2s, l, u)$, as a function of elastic Green-Lagrange strain $\bar{\mathbf{E}}_e$, temperature θ , density of damage entities η , the total dislocation density ρ , Stroh crack length $2s$, wing crack length l , and dislocation motion u . Note, the density of damage entities is dependent on dislocation density, since the Stroh crack nucleation is governed by plasticity. In addition, the density of activated damage entities is also dependent on the stress state, i.e. $\eta = \eta(\rho, \boldsymbol{\sigma})$. The time derivative of Helmholtz free energy is given by

$$\rho_c \dot{\Psi} = \rho_c \frac{\partial \Psi}{\partial \bar{\mathbf{E}}_e} : \dot{\bar{\mathbf{E}}}_e + \rho_c \frac{\partial \Psi}{\partial \theta} \dot{\theta} + \rho_c \frac{\partial \Psi}{\partial \eta} \dot{\eta} + \rho_c \frac{\partial \Psi}{\partial \rho} \dot{\rho} + \rho_c \frac{\partial \Psi}{\partial s} \dot{s} + \rho_c \frac{\partial \Psi}{\partial l} \dot{l} + \rho_c \frac{\partial \Psi}{\partial u} \dot{u}. \quad (64)$$

Invoking the relation between Helmholtz free energy and internal energy (U), i.e.

$$\Psi = U - \theta S, \quad (65)$$

and using Eq. (62), an alternate expression for Eq. (63) can be obtained:

$$\boldsymbol{\sigma} : \mathbf{d} - \rho_c \dot{\Psi} - \rho_c S \dot{\theta} - \frac{\nabla \theta}{\theta} \cdot \mathbf{q} \geq 0. \quad (66)$$

If the process of thermal heat conduction (due to \mathbf{q}) is assumed independent of thermomechanical deformation rate \mathbf{d} and entropy rate \dot{S} , then the above inequality yields two stronger inequalities, Planck's inequality and Fourier's inequality (Scheidler and Wright, 2001):

$$\boldsymbol{\sigma} : \mathbf{d} - \rho_c \dot{\Psi} - \rho_c S \dot{\theta} \geq 0; \text{ and } - \frac{\nabla \theta}{\theta} \cdot \mathbf{q} \geq 0, \quad (67)$$

where Planck's inequality accounts for temperature increase due to inelastic thermo-mechanical dissipation processes.

Thermodynamic constraints on internal variables are assessed in the remainder of this section. Using $\mathbf{d} = \mathbf{l}_{sym}$ from Eq. (107) in Planck's inequality, Eq. (67),

$$\begin{aligned}
\boldsymbol{\sigma} : & [\dot{\mathbf{F}}_e^m(\mathbf{F}_e)^{-1} + \mathbf{F}_e \dot{\mathbf{F}}_d(\mathbf{F}_d)^{-1}(\mathbf{F}_e)^{-1} \\
& + \mathbf{F}_e \mathbf{F}_d \dot{\mathbf{F}}_p(\mathbf{F}_p)^{-1}(\mathbf{F}_d)^{-1}(\mathbf{F}_e)^{-1}]_{sym} \\
& - \rho_c \frac{\partial \Psi}{\partial \bar{\mathbf{E}}_e} : \dot{\bar{\mathbf{E}}}_e - \rho_c S \dot{\theta} - \rho_c \frac{\partial \Psi}{\partial \theta} \dot{\theta} \\
& - \rho_c \frac{\partial \Psi}{\partial \eta} \dot{\eta} - \rho_c \frac{\partial \Psi}{\partial \rho} \dot{\rho} - \rho_c \frac{\partial \Psi}{\partial s} \dot{s} - \rho_c \frac{\partial \Psi}{\partial l} \dot{l} - \rho_c \frac{\partial \Psi}{\partial u} \dot{u} \geq 0.
\end{aligned} \tag{68}$$

Grouping terms,

$$\begin{aligned}
& \left\{ \boldsymbol{\sigma} : [\dot{\mathbf{F}}_e^m(\mathbf{F}_e)^{-1}]_{sym} - \rho_c \frac{\partial \Psi}{\partial \bar{\mathbf{E}}_e} : \dot{\bar{\mathbf{E}}}_e \right\} \\
& + \left\{ \boldsymbol{\sigma} : [\mathbf{F}_e \dot{\mathbf{F}}_d(\mathbf{F}_d)^{-1}(\mathbf{F}_e)^{-1}]_{sym} - \rho_c \frac{\partial \Psi}{\partial \eta} \dot{\eta} - \rho_c \frac{\partial \Psi}{\partial s} \dot{s} - \rho_c \frac{\partial \Psi}{\partial l} \dot{l} \right\} \\
& + \left\{ \boldsymbol{\sigma} : [\mathbf{F}_e \mathbf{F}_d \dot{\mathbf{F}}_p(\mathbf{F}_p)^{-1}(\mathbf{F}_d)^{-1}(\mathbf{F}_e)^{-1}]_{sym} - \rho_c \frac{\partial \Psi}{\partial \rho} \dot{\rho} - \rho_c \frac{\partial \Psi}{\partial u} \dot{u} \right\} \\
& - \rho_c \left[\frac{\partial \Psi}{\partial \theta} + S \right] \dot{\theta} \geq 0.
\end{aligned} \tag{69}$$

Eq. (69) has two implications. First, physical laws are required to describe the evolution of internal variables ($\dot{\eta}$ and $\dot{\rho}$). Secondly, a thermodynamic consistent definition for the inelastic strain should be a function of corresponding internal variables. We elaborate on these implications in the next sub-sections.

In Eq. (69), we let the sufficiently understood kinetics of crack growth [Eqs. (37) and (52)] and the kinetics of dislocation velocity (Eq. (118)) constrain the rate-derivatives \dot{s} , \dot{l} , and \dot{u} . Our problem is then reduced to enforcing constraints on $\dot{\eta}$ and $\dot{\rho}$. We instigate a microstructural basis for their definitions, which will become apparent in the following sub-sections.

We assume, the dissipation rate in Eq. (69) does not depend on the rate of elastic strain or the rate of temperature change. Both the damage due to cracking and the dislocation plasticity are dissipative processes (i.e. rate of entropy is positive). As a consequence, Eq. (69) leads to two equalities and two inequalities, which will provide further insight in to the kinematics and kinetics of inelastic processes.

5.1. Reversible matrix elasticity

The material density in the elastically unloaded configuration is $\bar{\rho} = \rho_c \det \mathbf{F}_e = \rho_c J_e$. The first term in Eq. (69) leads to an equality

$$\begin{aligned}
& \left\{ \boldsymbol{\sigma} : [\dot{\mathbf{F}}_e(\mathbf{F}_e)^{-1}]_{sym} - \rho_c \frac{\partial \Psi}{\partial \bar{\mathbf{E}}_e} : \dot{\bar{\mathbf{E}}}_e \right\} = 0, \\
& \Rightarrow \frac{\rho_c}{\bar{\rho}} \left[\det(\mathbf{F}_e) \boldsymbol{\sigma} : \mathbf{d}_e - \bar{\rho} \frac{\partial \Psi}{\partial \bar{\mathbf{E}}_e} : \dot{\bar{\mathbf{E}}}_e \right] = 0, \\
& \Rightarrow \frac{\rho_c}{\bar{\rho}} \left[\det(\mathbf{F}_e) \boldsymbol{\sigma} : (\mathbf{F}_e)^{-T} \bar{\mathbf{d}}_e(\mathbf{F}_e)^{-1} - \bar{\rho} \frac{\partial \Psi}{\partial \bar{\mathbf{E}}_e} : \dot{\bar{\mathbf{E}}}_e \right] = 0, \\
& \Rightarrow \frac{\rho_c}{\bar{\rho}} \left[\det(\mathbf{F}_e) (\mathbf{F}_e)^{-1} \boldsymbol{\sigma} (\mathbf{F}_e)^{-T} - \bar{\rho} \frac{\partial \Psi}{\partial \bar{\mathbf{E}}_e} \right] : \dot{\bar{\mathbf{E}}}_e = 0.
\end{aligned} \tag{70}$$

where $\bar{\mathbf{d}}_e = \dot{\bar{\mathbf{E}}}_e$. One can obtain a stress rule from the first term. In the elastically unloaded configuration, $\bar{\mathcal{B}}$, for values of $\dot{\bar{\mathbf{E}}}_e$, $\dot{\theta}$, and $\rho_c \neq 0$:

$$\bar{\rho} \frac{\partial \Psi}{\partial \bar{\mathbf{E}}_e} = J_e(\mathbf{F}_e)^{-1} \boldsymbol{\sigma} (\mathbf{F}_e)^{-T} \equiv \bar{\mathbf{S}}, \tag{71}$$

where $\bar{\mathbf{S}}$ is the second Piola-Kirchhoff stress—a symmetric stress tensor in $\bar{\mathcal{B}}$ and $J_e = \det(\mathbf{F}_e)$. Thus, in the elastically unloaded configuration, the second Piola-Kirchhoff stress tensor is the work conjugate of the symmetric rate of elastic deformation tensor in the same configuration. While in the current configuration, it can be shown that the work conjugate pairs are the Kirchhoff stress $\boldsymbol{\tau} = \det(\mathbf{F}_e) \boldsymbol{\sigma}$ and the symmetric rate of elastic deformation tensor in the current configuration $[\dot{\mathbf{F}}_e(\mathbf{F}_e)^{-1}]_{sym} = \mathbf{d}_e = (\mathbf{F}_e)^{-T} \dot{\bar{\mathbf{E}}}_e(\mathbf{F}_e)^{-1} = [(\mathbf{l}_e)^T + \mathbf{l}_e]/2$.

We note that the elastic strains accounted by the variable $\bar{\mathbf{E}}_e$ are contributions from the pristine matrix as well as the defects (cracks and voids). For example, under tri-axial tensile load, cracks will open up contributing to the overall strain. This strain is commonly assumed recoverable upon removal of the load. The material stiffness is obtained from the derivatives of the Helmholtz energy with respect to the recoverable strains, given by

$$\mathbb{C} = \frac{\partial^2 \Psi}{\partial \bar{\mathbf{E}}_e \otimes \partial \bar{\mathbf{E}}_e}. \tag{72}$$

This measure of *degraded* stiffness is in general smaller compared to the pristine material stiffness. Our work adopts the components of the compliance tensor (inverse of the stiffness tensor) derived by Ayyagari et al. (2018) for considering the Stroh

crack and wing-crack kinematics.

5.2. Load-induced damage growth

For crack-induced damage (the second term in Eq. (69)) is

$$\begin{aligned}
& \left\{ \boldsymbol{\sigma} : \left[\mathbf{F}_e \dot{\mathbf{F}}_d (\mathbf{F}_d)^{-1} (\mathbf{F}_e)^{-1} \right]_{sym} - \rho_c \frac{\partial \Psi}{\partial \eta} : \dot{\eta} - \rho_c \frac{\partial \Psi}{\partial s} \dot{s} - \rho_c \frac{\partial \Psi}{\partial l} \dot{l} \right\} \geq 0, \\
& \Rightarrow \frac{\rho_c}{\tilde{\rho}} \left[J_d J_e (\mathbf{F}_e)^{-1} \boldsymbol{\sigma} (\mathbf{F}_e)^{-T} : \bar{\mathbf{d}}_d - \tilde{\rho} \frac{\partial \Psi}{\partial \eta} : \dot{\eta} - \tilde{\rho} \frac{\partial \Psi}{\partial s} \dot{s} - \tilde{\rho} \frac{\partial \Psi}{\partial l} \dot{l} \right] \geq 0, \\
& \Rightarrow \frac{\rho_c}{\tilde{\rho}} \left[J_d (\mathbf{F}_d)^{-1} \bar{\mathbf{S}} (\mathbf{F}_d)^{-T} : \tilde{\mathbf{d}}_d - \tilde{\rho} \frac{\partial \Psi}{\partial \eta} : \dot{\eta} - \tilde{\rho} \frac{\partial \Psi}{\partial s} \dot{s} - \tilde{\rho} \frac{\partial \Psi}{\partial l} \dot{l} \right] \geq 0, \\
& \Rightarrow \frac{\rho_c}{\tilde{\rho}} \left[\tilde{\mathbf{S}} : \tilde{\mathbf{d}}_d - \tilde{\rho} \frac{\partial \Psi}{\partial \eta} : \dot{\eta} - \tilde{\rho} \frac{\partial \Psi}{\partial s} \dot{s} - \tilde{\rho} \frac{\partial \Psi}{\partial l} \dot{l} \right] \geq 0.
\end{aligned} \tag{73}$$

where $\tilde{\rho} \frac{\partial \Psi}{\partial \eta} : \dot{\eta}$ is the energy stored from accommodating new free surfaces within the original pristine matrix due to crack nucleation. The term $\tilde{\mathbf{d}}_d$ has contributions from crack growth. A definition for the rate of strain tensor ($\tilde{\mathbf{d}}_d = \dot{\hat{\mathbf{E}}}_d$) is given by the time-derivative of Eq. (39), which is micromechanically consistent with the growth of Stroh cracks and wing cracks under global tension as well as global compression.

In this work, we will constrain the growth rate for the Stroh cracks and the wing cracks (\dot{s} and \dot{l}) using the kinetics law for dynamic crack propagation, Eqs. (37) and (52). As such, the only remaining constraint implied by the above inequality is on the nucleation rate of crack density. In this work, we assume a constant crack density. The formation of new crack surfaces contributes to the rate of energy dissipation, which is $\tilde{\mathbf{S}} : \tilde{\mathbf{d}}_d$ less than the stored energy due to the creation of a density of cracks.

The second Piola-Kirchhoff stress in $\tilde{\mathcal{B}}$ is the pull-back of the second Piola-Kirchhoff stress $\bar{\mathbf{S}}$ in $\bar{\mathcal{B}}$, i.e.

$$\tilde{\mathbf{S}} = J_d (\mathbf{F}_d)^{-1} \bar{\mathbf{S}} (\mathbf{F}_d)^{-T}. \tag{74}$$

Note the symmetry: since $\bar{\mathbf{S}} = \bar{\mathbf{S}}^T$, it implies $\tilde{\mathbf{S}} = \tilde{\mathbf{S}}^T$.

The activated wing crack density (a realization of η) evolves implicitly based on the alignment of the stress state with respect to the initial crack orientation distribution. We imposed a uniform orientation distribution for the nucleated density of Stroh cracks. The activation of wing-cracks from Stroh cracks is dependent on the local stress state and strain rate. η is the total pair of wing-cracks that may potentially activate, which is a sum of cracks that have activated and those that have

not yet activated. Since, the crack density in the dissipation expression includes the activated crack density, we have retained η in the dissipation.

5.3. Irreversible matrix plasticity

For dislocation-based residual plasticity, from the third term in Eq. (69),

$$\begin{aligned}
& \left\{ \boldsymbol{\sigma} : \left[\mathbf{F}_e \mathbf{F}_d \dot{\mathbf{F}}_p (\mathbf{F}_p)^{-1} (\mathbf{F}_d)^{-1} (\mathbf{F}_e)^{-1} \right]_{sym} - \rho_c \frac{\partial \Psi}{\partial \rho} \dot{\rho} - \rho_c \frac{\partial \Psi}{\partial u} \dot{u} \right\} \geq 0, \\
& \Rightarrow \frac{\rho_c}{\rho_0} \left[J_p J_d J_e (\mathbf{F}_d)^{-1} (\mathbf{F}_e)^{-1} \boldsymbol{\sigma} (\mathbf{F}_e)^{-T} (\mathbf{F}_d)^{-T} : \tilde{\mathbf{d}}_p - \rho_0 \frac{\partial \Psi}{\partial \rho} \dot{\rho} - \rho_0 \frac{\partial \Psi}{\partial u} \dot{u} \right] \geq 0, \\
& \Rightarrow \frac{\rho_c}{\rho_0} \left[J_p \tilde{\mathbf{S}} : \tilde{\mathbf{d}}_p - \rho_0 \frac{\partial \Psi}{\partial \rho} \dot{\rho} - \rho_0 \frac{\partial \Psi}{\partial u} \dot{u} \right] \geq 0, \\
& \Rightarrow \frac{\rho_c}{\rho_0} \left[J_p (\mathbf{F}_p)^{-1} \tilde{\mathbf{S}} (\mathbf{F}_p)^{-T} : \mathbf{D}_p - \rho_0 \frac{\partial \Psi}{\partial \rho} \dot{\rho} - \rho_0 \frac{\partial \Psi}{\partial u} \dot{u} \right] \geq 0, \\
& \Rightarrow \frac{\rho_c}{\rho_0} \left[\mathbf{S} : \mathbf{D}_p - \rho_0 \frac{\partial \Psi}{\partial \rho} \dot{\rho} - \rho_0 \frac{\partial \Psi}{\partial u} \dot{u} \right] \geq 0,
\end{aligned} \tag{75}$$

where $\dot{u} = \bar{v}$ is the dislocation velocity, and the second Piola-Kirchhoff stress \mathbf{S} in \mathcal{B}_0 is the pull-back of the second Piola-Kirchhoff stress in $\hat{\mathcal{B}}$, i.e.

$$\mathbf{S} = J_p (\mathbf{F}_p)^{-1} \tilde{\mathbf{S}} (\mathbf{F}_p)^{-T}. \tag{76}$$

Also, $\rho_0 \frac{\partial \Psi}{\partial \rho}$ is the force that leads to change in the dislocation density, e.g. nucleation, annihilation, and the resulting energy change is included in the rate of energy dissipation $\mathbf{S} : \mathbf{D}_p$. Further, $J_p = \rho_0 / \tilde{\rho}$ is the Jacobian of plastic deformation. For volume conserving plastic deformation $J_p = 1$.

The energy (and contribution to plastic strain) associated with dislocation production is commonly ignored, because the term associated with energy expended (and contribution to plastic strain) in motion of dislocations yields much larger contribution to dissipation. A Taylor-Quinney factor of $Q = 0.9$, for example, suggests the energy expended by dislocation motion is approximately 90% (converted into heat), while the remaining 10% of the energy supplied is stored as strain energy due to dislocation network of mobile and immobile dislocation densities. Recently, Bertin and Cai (2018) developed calculations for the energy of periodic discrete dislocation networks using the non-singular theory for dislocations (Cai et al., 2006). Their work showed that approximately 5% of the work done per unit volume is stored as elastic energy due to the dislocation network. For a network of straight dislocations of length L and dislocations density ρ in volume V , the elastic energy per unit volume

is expressed as (Hull and Bacon, 2011)

$$\psi_d^0 = A \frac{Gb^2L}{4\pi V} \ln \left(\frac{R}{a_0} \right) = A\rho \frac{Gb^2}{4\pi} \ln \left(\frac{R}{a_0} \right), \quad (77)$$

where $A = 1$ for a screw dislocation and $A = 1/(1 - \nu)$ for an edge dislocation, R is the cut-off radius for the dislocation's stress field, ρ is the total dislocation density (length of dislocations per unit volume), and $a_0 = 0.1b$ is the core radius. The cut-off radius for the energy calculation may be approximated to be $R \approx 1/\sqrt{\rho}$. The above expression has an excellent agreement with discrete dislocation calculations (Bertin and Cai, 2018).

For a moving dislocation the energy is given by the sum of kinetic energy and strain energy. Including the effect of a mixed dislocation character, where ϕ_c is the angle made by the Burgers vector with the line sense vector (i.e. $\phi_c = 90$ deg for pure edge and $\phi_c = 0$ for pure screw), a non-singular solution for the energy of a moving dislocation is given as follows (Hirth et al. MSM 1998):

$$\psi_d = \psi_d^0 \zeta_d(\phi_c, \bar{v}), \quad (78)$$

and

$$\zeta_d(\phi_c, \bar{v}) = (\gamma_l)^{-1} \cos^2 \phi_c + [8\gamma_l + 4(\gamma_l)^{-1} - 7\gamma_t - 6(\gamma_t)^{-1} + (\gamma_t)^{-3}] \left(\frac{c_L}{\bar{v}} \right)^2 \sin^2 \phi_c, \quad (79)$$

where $\gamma_l = [1 - (\bar{v}/c_L)^2]^{0.5}$, $\gamma_t = [1 - (\bar{v}/c_T)^2]^{0.5}$, \bar{v} is the dislocation velocity, c_L is the longitudinal wave velocity, and c_T is the transverse (shear) wave velocity for an isotropic material.

Substituting Eq. (78) in Eq. (75), gives a constraint for the evolution of the dislocation density as follows:

$$\frac{\rho_c}{\rho_0} \left[\mathbf{S} : \mathbf{D}_p - \rho_0 A \frac{Gb^2}{4\pi} \ln \left(\frac{R}{a_0} \right) \zeta_d(\phi_c, \bar{v}) \dot{\rho} \right] \geq 0. \quad (80)$$

This expression assumes that the dislocation velocity is dependent on material properties and the stress state acting on a dislocation within an isotropic, homogeneous medium (Daphalapurkar et al., 2014). Finally, this inequality provides a constraint for the evolution of dislocation density given by Eq. (21).

5.4. Evolution of temperature

From Eq. (69), one can obtain an entropy rule from the last term. In the elastically unloaded configuration, $\bar{\mathcal{B}}$, for values of θ and $\rho_c \neq 0$:

$$S = -\frac{\partial \Psi}{\partial \theta}, \quad (81)$$

where S is the entropy, θ is the temperature, and $\Psi = \Psi(\bar{\mathbf{E}}_e, \theta, \eta, \rho, 2s, l, u)$ is the Helmholtz energy. We follow the rate form of temperature evolution elaborated by (Luscher et al., 2018). The material time derivative of entropy in the elastically unloaded configuration $\bar{\mathcal{B}}$ is given by

$$\begin{aligned} \dot{S} = & -\frac{d}{dt} \frac{\partial \Psi}{\partial \theta} = -\frac{\partial^2 \Psi}{\partial \theta^2} \dot{\theta} - \frac{\partial^2 \Psi}{\partial \mathbf{E}_e \partial \theta} : \dot{\mathbf{E}}_e \\ & - \frac{\partial^2 \Psi}{\partial \eta \partial \theta} \dot{\eta} - \frac{\partial^2 \Psi}{\partial \rho \partial \theta} \dot{\rho} - \frac{\partial^2 \Psi}{\partial s \partial \theta} \dot{s} - \frac{\partial^2 \Psi}{\partial l \partial \theta} \dot{l} - \frac{\partial^2 \Psi}{\partial u \partial \theta} \dot{u}. \end{aligned} \quad (82)$$

The specific heat is expressed as the second derivative of a thermodynamic potential, $C_{\mathbf{E}_e} = -\theta(\partial^2 \Psi)/(\partial \theta^2)$, where $C_{\mathbf{E}_e}$ is the specific heat at constant elastic deformation.

Multiplying Eq. (82) with density and temperature gives

$$\begin{aligned} \rho_c C_{\mathbf{E}_e} \dot{\theta} = & \rho_c \dot{S} \theta + \\ & \rho_c \theta \left(\frac{\partial^2 \Psi}{\partial \mathbf{E}_e \partial \theta} : \dot{\mathbf{E}}_e + \frac{\partial^2 \Psi}{\partial \eta \partial \theta} \dot{\eta} + \frac{\partial^2 \Psi}{\partial \rho \partial \theta} \dot{\rho} + \frac{\partial^2 \Psi}{\partial s \partial \theta} \dot{s} + \frac{\partial^2 \Psi}{\partial l \partial \theta} \dot{l} + \frac{\partial^2 \Psi}{\partial u \partial \theta} \dot{u} \right). \end{aligned} \quad (83)$$

An alternate expression for the balance of energy is written by combining Eqs. (61), (62), (64), and (65). Further, the equation is expressed in the elastically unloaded configuration, $\bar{\mathcal{B}}$, and is obtained by multiplying J_e :

$$\begin{aligned} \bar{\rho} \dot{S} \theta - (-J_e \nabla \cdot \mathbf{q} + \bar{\rho} r) = & \left(\bar{\mathbf{S}} - \bar{\rho} \frac{\partial \Psi}{\partial \mathbf{E}_e} \right) : \bar{\mathbf{d}}_e - \bar{\rho} \left(\frac{\partial \Psi}{\partial \theta} + S \right) \dot{\theta} + \bar{\mathbf{S}} : (\bar{\mathbf{d}}_d + \bar{\mathbf{d}}_p) \\ & - \bar{\rho} \left(\frac{\partial \Psi}{\partial \eta} \dot{\eta} + \frac{\partial \Psi}{\partial \rho} \dot{\rho} + \frac{\partial \Psi}{\partial s} \dot{s} + \frac{\partial \Psi}{\partial l} \dot{l} + \frac{\partial \Psi}{\partial u} \dot{u} \right). \end{aligned} \quad (84)$$

Using Eqs. (70) and (81), the first two bracketed-terms on the right side of the

equation disappear and Eq. (84) simplifies to the following form:

$$\begin{aligned} \bar{\rho}\dot{S}\theta - (-J_e\nabla \cdot \mathbf{q} + \bar{\rho}r) = & \bar{\mathbf{S}} : (\bar{\mathbf{d}}_d + \bar{\mathbf{d}}_p) \\ & - \bar{\rho} \left(\frac{\partial\Psi}{\partial\eta}\dot{\eta} + \frac{\partial\Psi}{\partial\rho}\dot{\rho} + \frac{\partial\Psi}{\partial s}\dot{s} + \frac{\partial\Psi}{\partial l}\dot{l} + \frac{\partial\Psi}{\partial u}\dot{u} \right). \end{aligned} \quad (85)$$

Substituting for the rate of entropy from Eq. (83) gives a final expression for rate of temperature increase:

$$\begin{aligned} \bar{\rho}C_{\mathbf{E}_e}\dot{\theta} = & \underbrace{\bar{\mathbf{S}} : (\bar{\mathbf{d}}_d + \bar{\mathbf{d}}_p)}_{\text{Plastic and damage power}} - \underbrace{\bar{\rho} \left(\frac{\partial\Psi}{\partial\eta} : \dot{\eta} + \frac{\partial\Psi}{\partial\rho}\dot{\rho} \right)}_{\text{Stored energy}} + \underbrace{(-J_e\nabla \cdot \mathbf{q} + \bar{\rho}r)}_{\text{Heat source/sink and flux}} \\ & - \underbrace{\bar{\rho} \left(\frac{\partial\Psi}{\partial s}\dot{s} + \frac{\partial\Psi}{\partial l}\dot{l} + \frac{\partial\Psi}{\partial u}\dot{u} \right)}_{\text{Expend surface and non-thermal energies}} + \underbrace{\bar{\rho}\theta \frac{\partial^2\Psi}{\partial\mathbf{E}_e\partial\theta} : \dot{\mathbf{E}}_e}_{\text{Thermo-elastic coupling}} \\ & + \underbrace{\bar{\rho}\theta \left(\frac{\partial^2\Psi}{\partial\eta\partial\theta}\dot{\eta} + \frac{\partial^2\Psi}{\partial s\partial\theta}\dot{s} + \frac{\partial^2\Psi}{\partial l\partial\theta}\dot{l} \right)}_{\text{Thermo-damage coupling}} + \underbrace{\bar{\rho}\theta \left(\frac{\partial^2\Psi}{\partial\rho\partial\theta}\dot{\rho} + \frac{\partial^2\Psi}{\partial u\partial\theta}\dot{u} \right)}_{\text{Thermo-plastic coupling}} \end{aligned} \quad (86)$$

The resulting temperature increase is attributed to thermal energies created from microscale processes, such as friction on sliding crack surfaces, inelastic breaking of bonds, and interaction of a moving dislocation with atoms. In the aforementioned expression, the terms besides the plastic power and damage power dissipation are commonly ignored in order to calculate the temperature increase. Elaborate thermodynamics involving thermo-elastic, thermo-damage, and thermo-plastic coupling terms introduce nonlinearity in the macroscopic framework, however, the micromechanics models do not introduce consistent sources for nonlinearity.

5.5. Pressure- and temperature-dependent shear modulus

Conventional strength models for dynamic material response up to a strain rate of 1000 s^{-1} typically do not consider the effect of pressure on shear properties. However, under extreme compression, pressure influences the shear modulus, which in turn influences plasticity under high pressure. In addition, the shear modulus is also influenced by the temperature. Steinberg et al. (1980) proposed a relation between pressure, temperature, and shear modulus for high pressure and temperatures up to

the melting point. The shear modulus is given as

$$G = G_a \left[1 + \left(\frac{1}{G_a} \frac{\partial G}{\partial p} \right) (p - p_a) J_e^{1/3} + \left(\frac{1}{G_a} \frac{\partial G}{\partial \theta} \right) (\theta - \theta_a) \right] \quad (87)$$

where G_a , p_a , and θ_a are shear modulus, pressure and temperature at ambient conditions, i.e. $p_a \approx 0$ and $\theta_a = 300\text{K}$. J_e is the ratio of deformed specific volume to ambient specific volume of elastic deformation. Values of temperature-dependent material parameters for beryllium are given in Table 2.

In addition to the temperature dependence of the shear modulus, one may assume that the elastic modulus is temperature dependent, as well. However, since the change in the elastic modulus between 0 K - 1500 K is merely 10 % (Nadal and Bourgeois, 2010), we assume a constant elastic modulus in this study. We calculated the linear elastic modulus from ambient shear modulus of 135 GPa and Poisson's ratio of 0.06. Moreover, we assume that the temperature change does not influence the fracture (surface) energy of the material. Note that a more realistic approach, especially for dynamic compression involving shock waves, must account for the pressure dependence of bulk modulus.

6. Numerical implementation

6.1. Overview of constitutive equations

The total deformation gradient is given by

$$\mathbf{F} = \mathbf{F}_e \bar{\mathbf{F}}_d \tilde{\mathbf{F}}_p. \quad (88)$$

$\bar{\mathcal{B}}$ is an intermediate configuration after unloading elastically from the current configuration \mathcal{B} . B_0 is the reference configuration. $\tilde{\mathcal{B}}$ is the configuration after applying plastic deformation.

In the intermediate configuration $\bar{\mathcal{B}}$, the velocity gradient is

$$\bar{\mathbf{l}} = \bar{\mathbf{l}}_e + \bar{\mathbf{l}}_d + \bar{\mathbf{l}}_p. \quad (89)$$

The symmetric (associated with stretch) part of the velocity gradient in $\bar{\mathcal{B}}$ is

$$\bar{\mathbf{d}} = \bar{\mathbf{d}}_e + \bar{\mathbf{d}}_d + \bar{\mathbf{d}}_p. \quad (90)$$

The skew-symmetric part of the velocity gradient (associated with rotation) in $\bar{\mathcal{B}}$ is

$$\bar{\mathbf{w}} = \bar{\mathbf{w}}_e + \bar{\mathbf{w}}_d + \bar{\mathbf{w}}_p. \quad (91)$$

For isotropic plasticity $\bar{\mathbf{w}}_p \approx 0$. As a result, $\bar{\mathbf{w}}_e = \bar{\mathbf{w}} - \bar{\mathbf{w}}_d$ and $\bar{\mathbf{d}}_e = \bar{\mathbf{d}} - \bar{\mathbf{d}}_d - \bar{\mathbf{d}}_p$. Numerically, the deformation gradient at the current time $t + \Delta t$ is updated from reference t using

$$\mathbf{F}_e^{t+\Delta t} = \exp(\mathbf{l}_e \Delta t) \mathbf{F}_e^t \quad (92)$$

Alternatively, one may use a second order update

$$\mathbf{F}_e^{t+\Delta t} = (\mathbf{I} + \mathbf{l}_e^{n+1} \Delta t + 0.5 \mathbf{l}_e^{n+1} \mathbf{l}_e^{n+1} \Delta t^2) \mathbf{F}_e^t \quad (93)$$

The time derivative of the constitutive equation in the elastically unloaded configuration, $\bar{\mathcal{B}}$, is

$$\dot{\bar{\mathbf{S}}} = \dot{\mathbb{C}} \cdot \bar{\mathbf{E}}_e + \mathbb{C} \cdot \dot{\bar{\mathbf{E}}}_e = \left[-\mathbb{S}^{-1} \cdot \left(\dot{\mathbb{S}} \cdot \mathbb{S}^{-1} \right) \right] \cdot \bar{\mathbf{E}}_e + \mathbb{S}^{-1} \cdot \dot{\bar{\mathbf{E}}}_e \quad (94)$$

where the superscript dot represents derivative with respect to time, $\dot{\bar{\mathbf{S}}}$ is the rate of the second Piola-Kirchhoff stress in the elastically unloaded configuration $\bar{\mathcal{B}}$ and \mathbb{C} is the fourth order stiffness tensor as a function of recoverable strains and elasticity constants. The stiffness tensor was obtained from an inverse of the compliance tensor (\mathbb{S}) derived by Ayyagari et al. (2018), considering the wing-crack kinematics.

6.2. Plastic deformation update

The plastic flow update can be performed in either of the two intermediate configurations or the current configuration. Next, we identify some reasonable constitutive choices for the plastic flow update, by summarizing constitutive equations in the elastically unloaded configuration ($\bar{\mathcal{B}}$) and elastic and damage unloaded configuration ($\hat{\mathcal{B}}$).

Commonly, the plastic flow update is done in the current configuration, but in the following sub-sections we elaborate on methods for completing this in the two intermediate configurations. The resulting plastic flow update is indifferent to the choice of update procedure because of thermodynamic consistency (Belytschko et al., 2014).

6.2.1. Plastic flow update in the current configuration, \mathcal{B}

The tensorial rate of plastic deformation in the current configuration \mathcal{B} is given by

$$\mathbf{d}_p = \frac{3}{2} \frac{b \rho_M \bar{v}}{\bar{\sigma}} \text{dev}(\boldsymbol{\sigma}), \quad (95)$$

where $\bar{\sigma} = \sqrt{\frac{3}{2} \text{dev}(\boldsymbol{\sigma}) : \text{dev}(\boldsymbol{\sigma})}$ is the equivalent stress, $\text{dev}(\boldsymbol{\sigma}) = \boldsymbol{\sigma} - \text{hyd}(\boldsymbol{\sigma})$ is the deviatoric part and $\text{hyd}(\boldsymbol{\sigma})$ is the hydrostatic part of the Cauchy stress tensor

$\boldsymbol{\sigma}$ referred in the \mathcal{B} configuration. In addition, $b = |\mathbf{b}|$ is the magnitude of the Burgers vector, ρ_M is the mobile dislocation density, and \bar{v} is magnitude of the mean dislocation velocity.

6.2.2. Plastic flow update in elastic unloaded configuration, $\bar{\mathcal{B}}$

The tensorial rate of plastic deformation in elastically unloaded intermediate configuration $\bar{\mathcal{B}}$ is given by (Belytschko et al., 2014)

$$\bar{\mathbf{d}}_p = \frac{3}{2} \frac{b\rho_M\bar{v}}{\bar{\sigma}} [\bar{\mathbf{C}}_e \cdot \text{dev}(\bar{\mathbf{S}}) \cdot \bar{\mathbf{C}}_e], \quad (96)$$

where $\bar{\sigma} = \sqrt{\frac{3}{2}[\text{dev}(\bar{\mathbf{S}}) \cdot \bar{\mathbf{C}}_e] : [\text{dev}(\bar{\mathbf{S}}) \cdot \bar{\mathbf{C}}_e]}$ is the equivalent stress, $\text{dev}(\bar{\mathbf{S}}) = \bar{\mathbf{S}} - \text{hyd}(\bar{\mathbf{S}})$ is the deviatoric part and $\text{hyd}(\bar{\mathbf{S}})$ is the hydrostatic part of $\bar{\mathbf{S}}$ referred in the $\bar{\mathcal{B}}$ configuration. The hydrostatic part of $\bar{\mathbf{S}}$ defined in $\bar{\mathcal{B}}$ is a pull-back of the hydrostatic part of the Cauchy stress tensor $\boldsymbol{\sigma}$ in the current configuration \mathcal{B} (Belytschko et al., 2014), i.e.,

$$\text{hyd}(\bar{\mathbf{S}}) = \frac{1}{3}(\bar{\mathbf{S}} : \bar{\mathbf{C}}_e)\bar{\mathbf{C}}_e^{-1} = \frac{1}{3}\text{trace}(\boldsymbol{\sigma})J_e\bar{\mathbf{C}}_e^{-1}, \quad (97)$$

where $J_e = \det(\mathbf{F}_e)$ is the Jacobian of elastic deformation, $\bar{\mathbf{C}}_e = \mathbf{F}_e^T \mathbf{F}_e$ is the elastic Green-Lagrange deformation tensor, which acts as the metric in the intermediate configuration. $\bar{\mathbf{S}}$ is the second Piola-Kirchhoff stress tensor in $\bar{\mathcal{B}}$ configuration and is related to the Cauchy stress tensor in the current (\mathcal{B}) configuration through Eq. (71), derived previously based on thermodynamic consistency.

6.2.3. Plastic flow update in the elastic and damage unloaded configuration, $\tilde{\mathcal{B}}$

Plastic flow update in this configuration allows for the subsequent calculation of the updated plastic deformation gradient, without any pull-back operation compared to the previous choices for the plastic flow update. Additionally, the average number of dislocation in a pileup is calculated using the updated density of immobile dislocations. Finally, this choice of plastic flow update is also consistent with our assumption of plastic deformation gradient preceding the damage deformation gradient.

In configuration $\tilde{\mathcal{B}}$, it can be shown that $\tilde{\mathbf{C}}_{ed} = \mathbf{F}_e^T \mathbf{F}_d^T \mathbf{F}_d \mathbf{F}_e$ acts as a metric for tensor products, consistent with the allowable products between co-variant, contra-variant, or mixed tensors. The tensorial rate of plastic deformation in elastic and damage unloaded intermediate configuration $\tilde{\mathcal{B}}$ has the following form:

$$\tilde{\mathbf{d}}_p = \frac{3}{2} \frac{b\rho_M\bar{v}}{\tilde{\sigma}} [\tilde{\mathbf{C}}_{ed} \cdot \text{dev}(\tilde{\mathbf{S}}) \cdot \tilde{\mathbf{C}}_{ed}], \quad (98)$$

where $\tilde{\sigma} = \sqrt{\frac{3}{2}[\text{dev}(\tilde{\mathbf{S}}) \cdot \tilde{\mathbf{C}}_{ed}] : [\text{dev}(\tilde{\mathbf{S}}) \cdot \tilde{\mathbf{C}}_{ed}]}$ is the equivalent stress, $\text{dev}(\tilde{\mathbf{S}}) = \tilde{\mathbf{S}} - \text{hyd}(\tilde{\mathbf{S}})$ is the deviatoric part and $\text{hyd}(\tilde{\mathbf{S}})$ is the hydrostatic part of $\tilde{\mathbf{S}}$ referred in the $\tilde{\mathcal{B}}$ configuration. The hydrostatic part of $\tilde{\mathbf{S}}$ defined in $\tilde{\mathcal{B}}$ is a pull-back of the hydrostatic part of the Cauchy stress tensor $\boldsymbol{\sigma}$ in the current configuration \mathcal{B} , i.e.,

$$\text{hyd}(\tilde{\mathbf{S}}) = \frac{1}{3}(\tilde{\mathbf{S}} : \tilde{\mathbf{C}}_{ed})\tilde{\mathbf{C}}_{ed}^{-1} = \frac{1}{3}\text{trace}(\boldsymbol{\sigma})J_{ed}\tilde{\mathbf{C}}_{ed}^{-1}, \quad (99)$$

where $J_{ed} = \det(\mathbf{F}_e)\det(\mathbf{F}_d)$ is a product of the Jacobian of elastic and damage deformations and $\tilde{\mathbf{S}}$ is the second Piola-Kirchhoff stress tensor in $\tilde{\mathcal{B}}$ configuration. It can be shown that $\tilde{\mathbf{S}}$ is a pull-back of second Piola-Kirchhoff stress in the $\tilde{\mathcal{B}}$ configuration, given by $\tilde{\mathbf{S}} = J_d(\mathbf{F}_d)^{-1}\tilde{\mathbf{S}}(\mathbf{F}_d)^{-T}$.

7. Application of the model

We apply the model developed in this work to simulate the compressive response of polycrystalline Beryllium. The model was calibrated against uniaxial compression response obtained from SHPB and quasistatic experiments. Calculations were performed to obtain the temperature- and rate-dependent strengths in compression and to provide insights into the combined evolution of damage and plasticity. In the following subsections, we summarized experimental results on beryllium, included a brief discussion on the calibration process, and presented results from the calibrated model.

7.1. Experimental Results on Beryllium

Blumenthal et al. (1998) performed SHPB experiments for high rate compressive response of polycrystalline, S-200F grade beryllium. The quasistatic response was obtained by Ablen et al. (1995). The compressive response was strongly dependent on the applied strain rate between 0.001 and 4000 s⁻¹. The strain hardening response displayed a moderate temperature dependence between 77 K and 873 K. From SHPB experiments, no twins were observed for strains below 7%, which implies plastic deformation was accommodated through dislocation slip. Twinning was observed in samples deformed above 7% true strains, while both twinning and cracking were observed above 20% strain. The microcracks were observed at grain boundaries as well as within the grains. The advent of microcracking was concluded to end the linear strain hardening due to plasticity.

Single crystal beryllium demonstrates brittle failure in both tension and compression (Govila and Kamdar, 1970; Gandhi and Ashby, 1979). The cleavage is confined

to basal and prismatic planes (Wilhelm and Aldinger, 1976) or at structured dislocation cell walls (Gardner et al., 1977). At elevated temperatures, the fracture toughness of the material increases by a factor of 4.5 (Govila and Kamdar, 1970).

Polycrystalline beryllium demonstrates high failure strain under compression. Depending on the processing method, e.g. hot pressing, cross-rolling, the failure stress and strain of the specimen can vary significantly (Nicholas, 1975). For beryllium S-200F grade, at SHPB compression rates (3000 s^{-1}) and at room temperature, the failure stress and failure strain are higher than 1.25 GPa and 20%, respectively (Blumenthal et al., 1998; Cady et al., 2018). The values of failure stress or failure strain are not known because the specimens were not loaded to failure. At moderate rates in tension (300 s^{-1}) and at room temperature, the failure stress and failure strains are approximately 0.5 GPa and 4%, respectively (Nicholas, 1975). Beryllium thus demonstrates tension-compression asymmetry in the failure response, having a compression to tension ratio of failure stress near 2.5.

Formation of dislocation cellular structures was observed prior to the appearance of cracks in strained thin film specimens of beryllium (Pollock and Wilsdorf, 1983). Images of fractured beryllium specimens revealed an average value of the dislocation cell size to be $1.5\text{ }\mu\text{m}$ and covered a range of 1-3.5 μm . In addition, cracks were observed to nucleate from the cell walls (Gardner et al., 1977; Wilsdorf, 1983). It is commonly assumed that the dislocation cellular structure formation is a result of dislocations arranging themselves in a low energy configuration. Further, the size of the dislocation cells and the width of the cell walls progressively decrease with increasing dislocation density (Pollock and Wilsdorf, 1983; Oudriss and Feaugas, 2016). Similar to a dislocation pileup, the collective effect of interacting dislocations in a dislocation cell-wall may produce a local stress concentration.

We infer that the local stress concentration produced within the dislocation cell-wall is similar in notion to the stress concentration at the leading dislocation in a pileup model. Under this assumption, we apply the proposed viscoplastic damage model and the dislocation-mediated crack nucleation model to beryllium. We ignore the contribution of plasticity from deformation twins and the possible influence of twin boundaries in aiding crack propagation because these mechanisms are not well understood.

7.2. Calibration of the model

For calibration of our model we referred to the polycrystalline hot-pressed S-200F grade Beryllium from Brush Wellman Inc. Grain size varies considerably, with the average grain size being $11.4\text{ }\mu\text{m}$ and the maximum grain size being $50\text{ }\mu\text{m}$ (Cady et al., 2018). The microstructure consists of equi-axed grains with few pre-existing

twins. The total impurity content is less than 1%.

An initial boundary valued problem was solved, conforming to uniaxial stress conditions (Ayyagari et al., 2018). Strain rate is imposed in the current configuration, while output variables are stress and internal variables associated with damage and plasticity models. A set of normals representing individual Stroh crack planes were predefined. The range of Euler angles $\alpha_2 \in [0, \pi/2]$ and $\theta_2 \in [0, 2\pi]$ were equally divided in $n^{\alpha_2} = 2$ and $n^{\theta_2} = 8$ divisions, respectively, representing equiaxial distribution of crack plane normals. A small fractional angle, $\frac{1}{100}$, was added to the distribution of oriented angles to avoid division by zero from trigonometric terms that appear in the definition of degraded stiffness for the brittle damage model (Ayyagari et al., 2018). Note that, such a limited number of crack orientations may not model a rotation invariant mechanical response (Nemeth, 2014), however, we make this choice due to the lack of measurements on the evolution of defects. One may revisit this choice of orientation distribution once data from advanced techniques becomes available, e.g. X-ray phase contrast imaging for characterizing crack distribution (Leong et al., 2018). A maximum timestep of 10 ns was used for all calculations that limited the maximum increment of dislocation and damage within a timestep. The calculations were terminated right after the peak stress, since the stress softening response wasn't available from experiments for comparison with calculations.

The model was calibrated with temperature-dependent high-rate response data obtained from SHPB experiments (Blumenthal et al., 1998) and also with data from quasistatic rate experiments (Ablen et al., 1995). In general, the experiments in aforementioned references were not performed to failure, because of safety issues incurred by fragmenting the samples and the potential generation of toxic beryllium powder.

While calibration of most other viscoplastic models is restricted to high strain rates (Austin and McDowell, 2011), in our work, the rate-dependent trapping coefficient enabled calibration of the model to a wider range of strain rates, ranging from 0.001 - 4000 /s. Tables 2 and 3 present a set of material properties as a function of pressure and temperature. Tables 4 and 5 present calibrated parameters for the viscoplastic model and the brittle damage model, respectively. The calibrated set of values are not unique. We rely on obtaining a set of calibrated parameters that are closer to experimental measurements and microscopy observations reported in the literature. Parameters for which experimental data is unavailable, our calibrated values are comparable to viscoplastic studies on other metals, e.g. Austin and McDowell (2011); Luscher et al. (2017); Nguyen et al. (2017) and damage studies in brittle ceramics, e.g. Hu et al. (2015).

At low temperatures, plastic deformation is expected to have a relatively low

contribution to energy dissipation. As temperature increases, plastic deformation is expected to have an increasing role in energy dissipation. The net fracture energy will be a sum of energy expended in creation of new surfaces as well as the energy dissipated by dislocation plasticity. Since plastic dissipation is separately accounted for in our model, the Griffith's fracture energy associated with creation of new crack surfaces, excluding the work that goes in plastic deformation, was chosen as an input for calculating fracture toughness. Our model implementation is thus consistent with Rice (1968) theory on dissipation measured by the J-integral and the experimental observations of temperature-dependent increase in the measured fracture toughness for beryllium (Govila and Kamdar, 1970).

The density of Stroh cracks (η) and the pileup spacing (L_{ps}) act as influential parameters for calibration of the ultimate strain (failure strain). The pileup spacing was chosen based on the observations of dislocation cell-wall spacing in the range 1-3.5 μm from *in situ* experiments on beryllium (Pollock and Wilsdorf, 1983). In addition, the pile-up spacing was chosen based on the observation of the onset of cracks at a strain of 0.2 by Blumenthal et al. (1998). We calibrated the density of cracks that resulted in an ultimate strain of approximately 0.3. The calibrated number density of Stroh cracks for the aforementioned orientation distribution was 10^7 m^{-3} .

Experimental results suggest a substantial increase in cross slip of dislocations from basal to prismatic planes near 523 K (Taylor and Moore, 1964). As such, we anticipate changes to the rate of work hardening for tests at temperatures above 523K. The recovery term introduced in Eq. (21) generically accounts for the cross-slip phenomenon. However, we have not considered an explicit dependence of the recovery or trapping terms on the aforementioned transition temperature.

7.3. Results and Discussion

The very first set of results are obtained from a calculation employing the viscoplastic model alone, without the damage model. These results are compared with a calculation that employed the combined viscoplastic model and the damage model. We then conducted calculations for a range of initial temperatures and strain rates, for comparison with SHPB and quasistatic experimental data. Insights were obtained into the evolution of deformation and damage mechanisms using the calibrated material model for beryllium. Uniaxial stress-strain plots are presented for all the results. In addition, evolution of several field variables and internal variables are presented, including the mobile and immobile dislocation densities, plastic and damage Lagrangian strain tensors, and trace of the damage tensor. From each calculation, peak stress (ultimate stress), strain corresponding to the peak stress (ultimate strain), and

trace of damage corresponding to the peak stress (ultimate damage) were acquired. The failure strength is assumed to correspond with the ultimate stress, while the failure strain is assumed to correspond to the ultimate strain. We will discuss trends in the failure strain from our model to infer on the brittle to ductile transition. The simulations are conducted under dynamic adiabatic conditions, and the temperature of the material increases as deformation progresses.

7.3.1. Representative results

We present results from representative calculations at a temperature of 300 K and a compressive strain rate of 3000 s^{-1} . These calculations demonstrate the evolution of viscoplastic deformation with (Figure 6) and without (Figure 5) the damage model. The applied strain rate results in evolution of the Lagrangian strain component E_{11} , along the loading axis (X-axis or 1-axis). For the calculation without the damage model, the crack density parameter is set to zero and the nucleation criterion for Stroh cracks was set to zero, $L_{ps} = 0$.

Figure 5(a) shows a plot of the evolution of six components of Cauchy stress tensor with the strain component E_{11} along the horizontal axis. As a consequence of the boundary conditions imposed for developing a uniaxial stress state, all the stress components are nearly zero, except for the stress component along the loading axis, σ_{11} . Since damage is deactivated, the trace of damage tensor in Figure 5(a), the damage tensor in Figure 5(b), and the Lagrangian strain tensor for damage in Figure 5(c) are all zero. The simulation is carried out to a strain of 0.5. The stress-strain curve does not show any stress softening (i.e. decrease in stress with increasing strain).

Figure 5(d) shows the evolution of dislocation densities. For strains less than 0.05, the mobile dislocation density is higher than the immobile dislocation density. Beyond a strain of 0.05, the mobile dislocation density saturates, while the immobile dislocation density increases towards its saturation value. The overall trends in the evolution of these dislocation densities is consistent with experimental measurements on FCC materials Al and Cu and associated viscoplastic models (Bratov and Borodin, 2015). Figure 5(e) and Figure 5(f) show evolution of the Lagrangian strain tensor components for plastic and total strains, respectively. Note, the components of total strain lateral to the loading axis are a consequence of the solution for the uniaxial stress boundary valued problem. The plastic strain has a relatively higher contribution to the total strain compared with the damage and elastic strains.

Without the damage response, the stress-strain curve based simply on dislocation plasticity will at most saturate to a flow stress. However, the plasticity model acting alone does not have the capability to model the stress softening. The recovery term

(for the immobile dislocation density) and the annihilation term (for the mobile dislocation density) are the mathematical terms that model this saturation of immobile and mobile dislocation densities, respectively.

Figure 6 shows plots for corresponding results obtained from the viscoplastic model along with the damage model. Figure 6(a) shows that stress reaches a peak, beyond which, stress decreases with increasing strain (referred to as the stress softening). We will refer to the peak in the stress as the ultimate stress (or the strength). In this case, we terminated the simulation when the trace of the damage tensor reached a value of 5, as seen in Figure 6(b).

We elaborate on the rationale for choosing to plot the damage tensor, over damage deformation gradient tensor, in presentation of our results. Note that, the damage tensor ${}^s\bar{\mathbf{\Omega}}_d$ is a semi-physical representation of the crack distribution. While it accounts for the orientation and size of the cracks, the physical interpretation of the damage tensor is restricted to the opening cracks. Specifically, the trace of the damage tensor is commonly interpreted to correspond to the porosity of the specimen, and as such, a limiting value of 1 is often referred to as complete damage. Application of the damage tensor is empirically extended to represent even the sliding cracks (Hu et al., 2015). However, in compression, sliding cracks may dominate the contribution to the damage tensor, in which case, the value of ultimate damage may exceed one. So, if the damage tensor is used to represent sliding cracks, then the trace of the damage tensor may not be a good measure for porosity. On the other hand, the damage deformation gradient tensor \mathbf{F}_d accounts for sliding cracks, but our definition precludes contribution from opening cracks. Thus, despite the incomplete physical representation of the damage tensor, we use this measure to gain qualitative understanding from our results.

Figure 6(b) shows, the components of the damage tensor that are lateral to the loading axis have significantly evolved, implying formation of oriented crack normals. These oriented cracks are predominantly aligned along the directions perpendicular to the loading axis. Comparatively, the component of the damage tensor along the loading direction is small, and this relative difference is consistent with formation of oriented wing cracks seen in uniaxial compression of brittle materials (Paliwal et al., 2006; Ayyagari et al., 2018).

The components of the damage strain (Figure 6(c)) begin to evolve beyond a strain of 0.13. The magnitude of the damage strain components is small compared to the magnitude of the plastic strain components (Figure 6(e)), and despite this difference, the damage strain results in the softening response of the stress beyond the peak stress, because of the degradation in stiffness. Prior to the peak in the stress response, the immobile dislocation density shows a tendency to sustain (restrict any

further evolution), and the sustained value of immobile dislocation density is retained beyond the peak stress (in the stress softening regime). In this regime, even the plastic strain does not evolve, resulting in the total strain components in Figure 6(f) that are different from the ones computed from a purely viscoplastic response, shown in Figure 5(e). The sustained value of immobile dislocation density is below the prescribed value of saturation for the immobile dislocation density.

From Figure 6(d), the total dislocation density from our calculation at a strain of 0.2 is approximately $14.5 \times 10^{14} \text{ m}^{-2}$. The calculated value is comparable to the measured range of dislocation density 4×10^{14} to $6 \times 10^{14} \text{ m}^{-2}$ at the same strain in the experimentally deformed samples of beryllium (Brown et al., 2013).

Overall, the damage model contributes to the stress softening, resulting in material failure. The ultimate stress and the ultimate strain are a consequence of three things: the kinetics of damage, kinetics of plasticity, and the nucleation criterion for the cracks (at which the damage begins to grow). Thus, no unphysical criteria, such as a critical damage, is prescribed to predict a failure stress or failure strain.

7.3.2. Calibration with high rate and quasistatic experiments in compression

Material response is calculated under compressive loading for a variety of initial temperatures and constant strain rates from quasistatic to SHPB rates. Figure 7(a), 7(b), and 7(c) show the degree of agreement of the calculated uniaxial stress-strain response with the measured data for strain rates in the range 0.001 - 4300 s^{-1} . The experimental measurements for high rates are from Blumenthal et al. (1998) and for quasistatic rates are from Ablen et al. (1995). Experimental data is plotted using markers in color blue, while lines are results from our calculations.

The experimental data was not obtained to failure of the specimen, so the endpoints of the experimental data do not inform a failure strain. However, since cracks were seen at a strain of 0.2 (Blumenthal et al., 1998), we anticipate failure of the specimen soon after that strain value. The flaw density in our model for beryllium was adjusted to result in a failure strain (ultimate strain) of approximately 0.3. At lower rates in experiments, the specimens do not fail even at a strain of 0.5, inferred from Figure 7(c).

For the strain rate of 1 s^{-1} , shown in Figure 7(b), our calculations predict the specimens can sustain strains above 0.25, but less than 0.5. For the strain rate of 0.001 s^{-1} , shown in Figure 7(c), the experimental data shows that the specimens are able to sustain a strain of 0.5. Our calculation for the temperature of 473 K predicts early failure. On the other hand, our calculation for the temperature of 673 K shows that the material does not fail at a strain of 0.5, in agreement with the experiment.

Overall, the agreement of flow stress between experiments and calculations using

the set of calibrated parameters is reasonable. The flow stress at temperatures 573 K and 773 K, shown in Figure 7(a), do not have good agreement with experiments for strains less than 5%. We accept this limitation in order to obtain an agreement with the large strain response.

A *ductile* response, with a relatively higher failure strain, is apparent in the low-rate data, shown in Figures 7(b) and 7(c), compared with the high-rate data shown in Figure 7(a). We will refer to this increase in the failure strain (with decreasing strain rate) as the brittle to ductile transition with decreasing strain rate. From the available experimental data, the range of rates over which this brittle to ductile transition spans is unclear. In addition to the rate dependence of the failure strain, the failure strain increases with increasing temperature, as seen in Figures 7(b) and 7(c). We will elaborate on this brittle to ductile transition with decreasing rate and increasing temperature in the subsections that follow.

7.3.3. Brittle to ductile transition with temperature

Beryllium demonstrates brittle to ductile transition with increasing temperature (Blumenthal et al., 1998). We perform calculations using our model to elaborate on the temperature dependence of failure strain.

We performed uniaxial compression calculations on beryllium for various temperatures and at a fixed strain rate of 3000 /s. The Stroh crack density is fixed at $\eta = 10^7 / \text{m}^3$. Figure 8(a) shows uniaxial stress-strain plots (colored blue) obtained for different initial temperatures. The stress-strain curves are terminated at the ultimate stress for clarity of deciphering the ultimate values of stress, damage, and dislocation density. The yield stress, initial hardening, and flow stress are seen to decrease with increasing temperature. These trends are in agreement with the dynamic response of beryllium at different temperatures (Blumenthal et al., 1998). A similar trend in the dependence of flow stress on the temperature is observed from experiments conducted at quasistatic rates (Ablen et al., 1995; Dawu et al., 2016).

From Figure 8(a), the ultimate stress decreases with increasing temperature. On the other hand, the ultimate strain increases with increasing temperature. Our calculated results are in agreement with trends in the strains sustained by beryllium samples for different temperatures under dynamic rates (Blumenthal et al., 1998). The calculated ultimate value of stress is a result of competition between the kinetics of damage and kinetics of viscoplastic deformations. The same figure shows the evolution of the trace of damage with strain, E_{11} . The ultimate damage (trace of damage at ultimate stress) decreases with increasing temperature.

The evolution of dislocation density for corresponding temperatures is plotted in Figure 8(b). The mobile dislocation density saturates to the same value for all

temperatures. For a constant strain, e.g. strain of 0.15, the value of immobile dislocation density is the same, as well, regardless of the temperature. Since the brittle damage in our model is independent of the temperature, the differences in the resulting stress-strain responses with temperature is attributed primarily to the kinetics of dislocation motion, given by Eq. (118). Calculations suggest the saturation stress that is observed in Figure 8(a) is inversely related to the ultimate value of immobile dislocation density.

Figure 8(c) shows evolution of stress plotted against the effective plastic strain. The general trends of ultimate stress and ultimate damage as a function of temperature, seen in Figure 8(a), are applicable to the same variables in Figure 8(c).

The temperature dependence of failure strain from our model suggests that the failure strain increases gradually with increasing temperature. The combined kinetics of damage and kinetics of viscoplastic mechanisms is thus effective in modeling the brittle to ductile transition with increasing temperature.

We elaborate on the efficacy of our model for beryllium over other existing models. Johnson-Cook (JC) model (Johnson and Cook, 1983) and Mechanical Threshold Stress (MTS) Model (Follansbee and Kocks, 1988), extended from Mecking and Kocks (1981), are commonly used to model the strain rate and temperature dependence of the plastic flow stress. These models often additionally rely on a failure criterion, such as maximum plastic strain. For this work, the plastic strain to failure was unavailable because of toxicity associated with subjecting beryllium specimens to failure/fragmentation. Evidently from this work, plastic strain at failure is a function of temperature, rate, and tensorial stress-state. Our model predicts value of plastic strain and enables calibration of a functional for relatively efficient simulation schemes employing maximum plastic strain criterion.

7.3.4. Rate-dependence of dynamic failure strength

We conducted simulations for compressive rates between 0.001 through 10,000 s^{-1} at a fixed temperature of 300 K. Results from simulations are presented in Figure 9. Figures 9(a) and 9(b) show selective stress-strain plots (in blue) for a range of strain rates 0.001-100 /s and 100-10,000 /s, respectively. Evolution of damage with strain (in red) corresponding to individual stress-strain curves is superimposed on these plots. Evolution of immobile and mobile dislocation densities for all rates are shown in Figures 9(c) and 9(d), respectively.

For the range of rates 0.001-100 /s, the ultimate stress and ultimate strain increases with increasing rate. The crack-induced damage begins at a strain between 0.2-0.3 and the ultimate stress corresponds to a value of damage near 1. With increasing rate, higher strains are required to reach the ultimate damage, i.e. damage

at ultimate stress. The mobile dislocation density for all the rates in this range sustains at a value of about $1.55 \times 10^{14} /\text{m}^2$, while the immobile dislocation density is close to $1 \times 10^{15} /\text{m}^2$ and increases slightly with rate.

For the range of rates 100-10,000 /s, a significant deviation is observed in the evolution of damage and dislocation densities, compared to the quasistatic rates. With increasing rate, the ultimate stress increases, while the ultimate strain decreases. Lower strains are required to reach the ultimate damage, indicating gradual transition from a ductile to a relatively brittle response. The sustained value of mobile dislocation density decreases. The immobile dislocation density, as well as its rate, increases by a significant amount.

From Figure 9(c), the decreasing value of the sustained mobile dislocation density with rate implies decreasing role of plastic deformation, since the plastic flow is dependent on the mobile dislocation density. From Figure 9(d), the increasing value of immobile dislocation density suggests increased hardening. Moreover, since the criterion for nucleation of Stroh cracks is dependent on the immobile dislocation density, increased rates of immobile dislocation density lead to an earlier activation of Stroh cracks on the strain axis. Thus, plasticity is relatively more pronounced at lower rates, compared to the higher rates, while the brittle damage is more pronounced at the higher rates.

Figure 9(e) shows the rate-dependent response of dynamic failure strength (ultimate stress) in compression. Compared to the response of brittle materials without any significant plastic deformation, such as ceramic materials (Kimberley et al., 2013), the strength does not plateau at quasistatic strain rates between the range 10^{-3} and 100 s^{-1} . Such an increase in the failure strength (linear on a semi-log scale) from our calculations is similar to the trend in the rate-dependence of strength observed from experiments on Beryllium (Nicholas, 1975) and other metals, such as tantalum (Hoge and Mukherjee, 1977), aluminum and iron (Klopp et al., 1985). This rate-dependence of the strength at low rates is attributed to the rate-dependence of flow stress. As such, plasticity dominates the response of the material at low strain rate regime, which in case of beryllium is in the regime of strain rate less than 100 s^{-1} .

In Figure 9(e), the increase in the compressive strength for strain rates between 100 and 10^4 s^{-1} may be attributed to the rate-dependence from the damage model as well as the plasticity model. With increasing strain rate, the rate of damage is higher. While crack growth rate (and the crack density) limit the damage rate and the dissipation rate, the applied strain rate deposits an increasing amount of elastic energy, which reflects as an increase in the dynamic strength at higher rates (Daphalapurkar et al., 2011).

Note that, increasing the crack density is not always a judicious choice for in-

creasing the rate of damage. The damage is linearly dependent on the crack density and on the cube power of crack length. The contribution to the rate of damage from growing cracks may outweigh the contribution to the rate of damage from increasing the density of cracks. Moreover, increasing the density of cracks beyond a certain value may soften the material, which could hinder the rate of crack growth and lower the net rate of damage.

The suppressed rate of crack growth due to a high crack density is in addition to the retardation due to plastic flow. The onset of damage initiation (controlled by variable \bar{L}_{ps}) is thus a crucial parameter in the competition between rate of damage and rate of plastic flow. In our case, we calibrated \bar{L}_{ps} so that the Stroh cracks of length given by Eq. (30) are formed at approximately 20% strain, consistent with the observations of microcracks by Blumenthal et al. (1998).

rules The rate-dependence of dynamic failure strength of brittle materials may be described using a power law relation involving strain rate and the characteristic strain rate, which is a function of material properties (Kimberley et al., 2013). However, the relationship proposed by Kimberley et al. (2013) does not consider plastic deformation. We propose a similar relation for the dynamic failure strength of materials that considers brittle failure and plasticity. Our proposed relation accounts for rate effects due to plasticity and is given by the following expression:

$$\sigma_d = \sigma_{fu} \left[1 + \left(\frac{\dot{\epsilon}}{\dot{\epsilon}_0} \right)^{\frac{2}{3}} \right], \quad (100)$$

where σ_d is the dynamic failure strength under uniaxial stress conditions, σ_{fu} is the rate-dependent flow-stress at ultimate strain, $\dot{\epsilon}$ is the applied strain rate, and $\dot{\epsilon}_0$ is the characteristic strain rate. Terms σ_{fu} and $\dot{\epsilon}_0$ are specific to a material.

The characteristic strain rate is a function of material properties. The expression given by (Kimberley et al., 2013) was applicable for a two-dimensional measure of crack density. For a three-dimensional measure of crack density a modified expression for characteristic strain rate is given by

$$\dot{\epsilon}_0 = \alpha_1 \frac{c_d K_{IC}}{\hat{s} E} \eta^{\frac{1}{6}}, \quad (101)$$

where c_d is the one-dimensional wave speed, K_{IC} is plane strain fracture toughness calculated from surface energy of fracture, E is Young's modulus of elasticity, \hat{s} is the average half-length of pre-existing cracks, η is the flaw density, α_1 is a calibration constant, aligning the aforementioned relation to intercept at the quasistatic compressive strength of the material.

Quasistatic strength of brittle materials (e.g. ceramics) is commonly assumed to be a constant, because brittle materials do not demonstrate an appreciable change in the strength for rates less than 1 s^{-1} . However, for beryllium, the quasistatic strength is not constant, because the plastic flow stress is rate dependent even at lower rates. We thus make a modification to the scaling relation for brittle failure (Kimberley et al., 2013), in order to accommodate rate-dependence of compressive strength in the low rate regime. We approximate the rate-dependent flow stress using a linear relation with the natural logarithm of strain rate (Johnson and Cook, 1985) as follows:

$$\sigma_{fu} = [\alpha_2 + \alpha_3 \ln(\dot{\epsilon}^*)][1 - \theta^*], \quad (102)$$

where $\dot{\epsilon}^* = \dot{\epsilon}/\dot{\epsilon}_{00}$ is a non-dimensional strain rate, normalized by reference strain rate $\dot{\epsilon}_{00} = 1 \text{ s}^{-1}$, and $\theta^* = \theta/\theta_m$ is the homologous temperature. Since plasticity dominates the flow-stress response at low rates, we use data less than $\dot{\epsilon} \leq 2 \text{ s}^{-1}$ to calibrate the constants. As it turns out, values of these constants are dependent on the crack density. We obtained $\alpha_2 = 9.51 \times 10^8 \text{ Pa}$ and $\alpha_3 = 2.30 \times 10^7 \text{ Pa}$ for a crack density of 10^7 m^{-3} , while $\alpha_2 = 8.94 \times 10^8 \text{ Pa}$ and $\alpha_3 = 2.03 \times 10^7 \text{ Pa}$ for a crack density of 10^8 m^{-3} . We apply these calibrated constants to obtain the scaling of ultimate stress (or strength) for the strain rate regime $0.001\text{-}10,000 \text{ s}^{-1}$.

The characteristic strain rate is a function of material properties and the flaw statistics. The average half-length \hat{s} is estimated from the equilibrium length of a nucleated Stroh crack as $2.5 \text{ }\mu\text{m}$, using Eq. (30). Because the characteristic strain rate is dependent on the crack density, and since we do not have a measurement of crack density, we provide following values as illustrations. From our calculations for beryllium, the resulting characteristic strain rates were $\dot{\epsilon}_0 = 2.01 \times 10^4 \text{ s}^{-1}$ for a crack density of $\eta = 10^7 \text{ m}^{-3}$ and $\dot{\epsilon}_0 = 2.96 \times 10^4 \text{ s}^{-1}$ for a crack density of $\eta = 10^8 \text{ m}^{-3}$. Using $\alpha_1 = 0.1$, Eq. (101) has a reasonable agreement with the model-calculated dynamic failure strengths for both the flaw densities, as shown by the fits to the calculated data in Figure 9(e). Dynamic strength from experiments are not available for quantitative comparison with calculated results. Instead, we make a qualitative comparison with quasistatic measurements presented by Petch and Wright (1980), in the next subsection.

7.3.5. Grain size dependence of failure strain

Quasistatic data on the flow stress for different grain sizes of extruded beryllium suggests that flow stress increases with decreasing grain size (Petch and Wright, 1980). This variation is characterized by the Hall-Petch coefficient, which is the slope of the yield/flow stress to the square root of the inverse grain size. At room temperature, the Hall-Petch coefficient for the yield stress is $10 \text{ MPa}\cdot\text{mm}^{1/2}$, while

that for the flow stress at a strain of 0.005 is 20 MPa-mm^{1/2}. Thus, the Hall-Petch coefficient increases at higher strains for beryllium. Interestingly, the Hall-Petch coefficient for the failure stress is 51 MPa-mm^{1/2} and is much higher than that for any other flow stress (Petch and Wright, 1980). In yet another study by Greenspan (1957), with decreasing grain size (obtained by extrusion and cross-rolling), both the maximum strain to necking and the ultimate stress increases. Their data for the ultimate strain to ultimate stress was characterized by a linear relation that has a slope of $26.6 \times 10^{-4} \text{ MPa}^{-1}$. In the experimental study by Greenspan (1957), the ultimate strain of beryllium samples ranged from 0.2 to as high as 0.8. We infer, decreasing grain size has two effects: increase in the failure stress and increase in the failure strain. This behavior is counter-intuitive to our understanding of FCC metals, which demonstrate a strength-ductility trade-off, i.e. decreasing failure strain with decreasing grain size (or with increasing failure stress).

In our model, we have introduced a grain size dependence for the brittle failure model (Eq. (31)), which is independent of the grain size dependence of yield for the plasticity model (Eq. (121)). Figure 10 illustrates the resulting failure stress and failure strain with varying grain size. We have illustrated results for two (Stroh) crack densities. Figure 10(a) shows the dependence of the ultimate stress on the grain size for two flaw densities. The ultimate stress increases with decreasing grain size. With higher flaw density, the failure stress is lower, regardless of the strain rate. Figure 10(b) shows the dependence of the ultimate strain on the grain size for flaw densities of 10^7 and 10^8 m^{-3} , respectively. The ultimate strain increases with decreasing grain size. For the higher flaw density, the failure strain is lower regardless of the strain rate.

In our model, the harmonic average of the pileup spacing given by Eq. (31), which involves grain size as an additional variable, is able to model the atypical response of increasing failure strain with decreasing grain size for beryllium. Figure 10(b) shows calculated failure strains from the model with and without the grain size for a crack density of 10^7 m^{-3} . Without the term for grain size in Eq. (31) (i.e. $\bar{L}_{ps} = L_{ps}$), the response of the model to the decreasing grain size is opposite, i.e. the ultimate strain decreases, shown in Figure 10(b) for the crack density of 10^7 m^{-3} (labelled, without grain size effect).

From Figure 10(a), the increase of the ultimate stress (for small grain size) without the term for grain size in Eq. (31) is solely due to the Hall-Petch coefficient for yield stress, Eq. (121). The Hall-Petch coefficient for the ultimate stress from our model is higher compared to that for the yield stress, and this trend is consistent with the quasistatic data for ultimate stress presented in Petch and Wright (1980).

Thus, the notion of harmonic average of the pileup spacing is suitable for captur-

ing the qualitative trends in the dependence of ultimate strain and ultimate stress on the grain size. Because experimental data is unavailable for the grain size dependence of ultimate strain and ultimate stress for S-200F grade beryllium, our work is limited to qualitative validation of Eq. (31) with quasistatic measurements by Petch and Wright (1980). Next, we provide some insights in to the effect of microstructural parameters on the Hall-Petch slope for the ultimate stress.

Figure 10(c) shows a plot of the effect of crack density (η) and pileup spacing (L_{ps}) on the Hall-Petch slope for the ultimate stress against the inverse square root of the grain size. The baseline calibration parameters for this work are $\eta = 10^7 / \text{m}^3$ and $L_{ps} = 1.55 \mu\text{m}$. Comparison of results between the two cases of crack densities, keeping pileup spacing the same, reveals that increasing the crack density decreases the Hall-Petch slope for ultimate stress. On the other hand, comparison of results between the two cases of pileup spacing, for the same crack density, reveals that increasing the pileup spacing increases the Hall-Petch slope for ultimate stress. The ultimate stress has a nearly linear relation with inverse square root of the grain size, in qualitative agreement with measured data from Greenspan (1957) and Petch and Wright (1980).

Figure 10(d) shows a plot of the effect of crack density (η) and pileup spacing (L_{ps}) on the slope for the ultimate strain against ultimate stress. For a fixed crack density and pileup spacing, calculated results from varying grain size are plotted as one set of points. Increasing the crack density decreases the ultimate strain. Increasing the pileup spacing also decreases the ultimate strain. The slope indicates sensitivity of ultimate strain to the ultimate stress. The slope can also be used to interpret the change in ductility with the grain size. The slope, which is the change of ultimate strain with the grain size, decreases for higher crack density and for higher pileup spacing. The trends in variation of the failure stress with the grain size are applicable for the failure strain, as well. The variation of ultimate strain with ultimate stress may be described using a linear relation, in qualitative agreement with measured data from Greenspan (1957).

7.3.6. Tension-compression asymmetry in the failure strength

The anisotropic damage model in this work is capable of predicting failure strains under tension. We present comparison of results between tensile and compressive loading from our calculations. Figure 11 shows representative results obtained for a temperature of 300 K and strain rate of 3000 s^{-1} under compression [Figures 11(a) and 11(c)] and tension [Figures 11(b) and 11(d)].

Under tensile loading, the calculated value of strength is 500 MPa and ultimate strain is 0.018, as seen in Figure 11(b). Our predicted value for the tensile strength

is in agreement with the measured range of 450-550 MPa applicable for tensile rates 100-500 /s of different grades of beryllium (does not include S-200F grade used in this study) (Nicholas, 1975).

Under compressive loading, the strength of beryllium is 1.5 GPa. For a strain rate of 3000 /s and at room temperature, the ratio of compressive to tensile failure strength is approximately 3. For lower rates, this ratio may decrease. For example, for the rate of 0.001 /s, the calculated compressive strength is 790 MPa [from Figure 9(a)] and the tensile strength is 374 MPa (plot not included), which leads to a strength ratio of 2.1. Regardless of the rate, this compression to tension strength ratio is lower than that obtained from pure brittle damage models. For example, armor ceramics, rocks, and concrete demonstrate a strength ratio in the range 8-10 (Kimberley et al., 2013). On the other hand, for an isotropic plastic model acting alone, the compression to tension flow stress ratio for the same strain and loading conditions is 1.

The effect of viscoplastic damage model is to increase the strength under tension and reduce the strength under compression, compared with the purely brittle damage models. For both tension and compression, a critical amount of dislocation density is necessary to nucleate a Stroh crack. The effect of this dependence is pronounced under tension; the failure strength is higher compared with the pure brittle damage models. In case of compression, the activation of plasticity at relatively lower stress reduces the strength compared to the purely brittle damage models, e.g. for ceramics, which have a strength in the range of 3-5 GPa (Deshpande and Evans, 2008).

Figures 11(c) and 11(d) show the evolution of dislocation densities under compression and tension. For strains less than 0.016, the evolution of dislocation densities is similar. This is expected, since the viscoplastic model in our work incorporates isotropic hardening. We thus expect similar plastic flow under compression and tension early on, in absence of damage.

The anisotropic damage model is effective in predicting failure strains and strengths under compression as well as under tension. The calculated failure strains under compression are about an order of magnitude higher compared to the failure strain under tension. On the other hand the calculated strength under compression is higher than the strength under tension by a relatively smaller factor compared to the brittle materials that do not demonstrate plasticity.

7.3.7. Strengths and limitations of the proposed model

The proposed model, combining the kinetics of viscoplastic deformation with the kinetics of damage, along with a dislocation-mediated nucleation criteria for damage, can successfully predict trends in the failure stress and failure strain of beryllium

under varying temperature, strain rate, and grain size.

Using the viscoplastic model of Austin and McDowell (2011) as the baseline, following changes were implemented that extended the applicability to beryllium: (a) The rate-dependence of initial hardening (Follansbee and Kocks, 1988) was implemented as part of the trapping coefficient. This extended the calibration of the stress-strain curves over a wider range of rates, from SHPB to quasistatic. (b) The recovery term for the immobile dislocation density implemented saturation limit for the immobile dislocation density. Annihilation term for the mobile dislocation density implemented a saturation limit for mobile dislocation density. These saturation limits on dislocations density enabled physical basis for saturation stress.

The dependence of the Stroh crack nucleation on the immobile dislocation density informed the damage model on the onset of crack growth. The dislocation density continues to drive the dynamic growth of the Stroh crack, which enabled predictions of the failure stress. The geometric argument based on the harmonic average of pileup spacing and grain size enabled the grain size dependence of the failure strain.

Using the brittle damage model by Ayyagari et al. (2018) as the baseline, following changes were implemented. The damage model defined an expression for the damage deformation gradient, consistent with the kinematics of wing-crack growth and preceding plastic deformation. The cohesive length was used as a regularizing parameter for the stress-intensity at the tip of the wing crack, replacing unnatural dependence of the stress intensity on the growing (Stroh) crack size in the expression proposed by Nemat-Nasser and Obata (1988).

Stroh (1954) proposed that dislocation coalescence may simultaneously occur with nucleation of a Stroh crack. Implicit in this assumption is that the obstacle that held the pileup disappears upon crack formation. However, in our model, this additional mechanisms of dislocation escape at the crack surfaces was precluded, because the number of dislocations estimated to enter the cracks was significantly small compared to the total dislocation density. In our model, the rate of dislocation densities are affected by the damage through the multiplicative decomposition of the total deformation gradient, e.g. increase in damage reduces the net rate of dislocation generation. A related assumption is that we ignore the part of the kinetics of crack nucleation that results in a characteristic incubation time that is strain rate dependent (Lawn et al., 1983).

Our model assumes that the propagating crack tip does not generate a significant amount of dislocations. Our choice of assumption is based on the (a) limited availability of favorable slip systems for plasticity at the crack tip, as inferred from failure response through brittle cracking by the appearance of fracture surfaces, and (b) experimental evidence that the crack is more likely to take a path through dislocation

saturated cell-walls (Pollock and Wilsdorf, 1983; Gardner et al., 1977). In addition, the effective compliance (Ayyagari et al., 2018) is based on the linear elastic stress field at the tip of the crack. Indeed, the current framework may be advanced by considering the crack tip as source of dislocations for a variety of other metals, but we leave this development for the future.

At temperatures above 523 K, cross-slip significantly influences the material response (Govila and Kamdar, 1970). Above this transition temperature, the material may demonstrate latent hardening mechanisms, different than those at the room temperature, which are not considered in this model.

Some of the assumptions and analytical solutions at the lower length scale, for dislocations and cracks, were motivated by micromechanics solutions and are not consistent with those of the macroscopic model. Specifically, the treatment of cracks and dislocations most often rely on linear isotropic elasticity, but the macroscopic application invokes geometric and material nonlinearity. While the macroscopic framework considers a 3D stress state, the micromechanics solution for crack growth is based on two-dimensional plane strain conditions. Moreover, the macroscopic framework considers elaborate thermodynamics involving thermo-elastic, thermo-damage, and thermo-plastic coupling terms that involve nonlinearity, the micromechanics models do not introduce any relevant sources for nonlinearity.

Observations from SHPB experiments demonstrate twinning beyond 7% strain, this model does not consider twinning as a deformation mechanism. This is because twinning seems to have interactions with dislocations as well as with cracks, and we lack proper models representing these interactions. At moderate rates, we assume that dislocation plasticity dominates the response over twinning plasticity. At high strain rates beyond 5000s^{-1} , twinning appears to have a significant contribution to the materials response and is evident from the increase in the hardening rate (Sisneros et al., 2010). We accept this limitation in the model for sake of understanding the kinetics of combined dislocation-crack interactions.

Although, contribution of twinning is excluded from this work, we note some existing works that have accomplished inclusion of twinning plasticity within a finite deformation framework. Clayton (2009) introduced contribution of twinning to plastic deformation through the meso-incompatibility deformation gradient tensor. Our framework retains the meso-incompatibility deformation tensor and is thus amenable to including contribution of twinning to plastic deformation. Work by (Becker and Lloyd, 2016) on the reduced order model for HCP metals may be resourceful in incorporating an efficient model for twinning, without a need for a comprehensive crystal plasticity framework. Further, it is known that twinning may influence damage in certain HCP materials. The present theory, based on dislocation pileup-mediated nu-

cleation of cracks, can be readily extended to consider pileup of twinning dislocations and their influence on nucleated crack density (Lloyd, 2018).

8. Conclusions

This paper presents a new multi-scale theory and new results for Beryllium. Despite the relatively large number of calibrated parameters, the model captures a wide spectrum of physical phenomena in materials that undergo coupled inelasticity mechanisms acting in concurrence. The equations were motivated by fundamental physics and materials science with relevance to high rate failure mechanics. The original contributions from this work include: (a) grain size dependence of failure strain and failure strength, (b) a dynamic model for dislocation-mediated nucleation of a crack, (b) kinematic and energetic consistent coupling of damage and viscoplastic deformations within a large deformation framework, (c) calibration of the model to predict dynamic damage and failure of beryllium, and (d) demonstration that the competition between kinetics of damage and kinetics of viscoplastic deformation can successfully predict the brittle to ductile transition observed in Beryllium under dynamic loading conditions.

This work developed a finite deformation framework for the description of elasticity, isotropic plasticity, and anisotropic damage using a three-term decomposition of the deformation gradient. The kinematic basis for the decomposition of the deformation gradient led also to a formal definition of the damage deformation gradient tensor with respect to the intermediate configuration. Within this framework, the flow stress in the uniaxial stress-strain curve is influenced by the inelastic strains due to plasticity and damage.

The thermodynamic basis for calculation of the plastic strain rate tensor produced consistent formulations in the two intermediate configurations. Owing to thermodynamic consistency and to a dissipation inequality, it was possible to define the temperature evolution law and the constraints for the evolution of internal variables (density of cracks and density of dislocations). Finally, an explicit time integration scheme was designed. Pull-back and push-forward operations, necessary to obtain a material response that is rotation invariant for large deformation analysis, were derived directly from thermodynamic principles.

The kinetics law associated with the dislocation density evolution and crack growth produced a non-linear evolution of the stress-strain response that is dependent on the strain rate, temperature, and stress-state. Furthermore, the model is capable of capturing the brittle to ductile transition of the failure strain response with increasing temperature and decreasing strain rate.

The viscoplastic model was calibrated to the stress-strain response under compression obtained from split-Hopkinson pressure bar and quasistatic experiments on polycrystalline beryllium S-200F grade. Microstructural measurements of the pileup spacing at failure and onset-strain of cracks were used to inform the damage model. The present model is sufficiently flexible to capture a variety of phenomena, particularly tension-compression asymmetry in failure strength, rate dependence of failure stress, brittle to ductile transition with temperature and strain rate, grain size dependence of failure stress and failure strain.

Acknowledgments

Authors are grateful to Dr. Bill Blumenthal from Los Alamos National Laboratory for sharing experimental data on beryllium. Authors acknowledge and appreciate funding from ASC/PEM program, with the current program manager Dr. Marianne Francois and the former program manager Dr. Mark Schraad.

This work was performed under the Advanced Simulation and Computing Program supported by National Nuclear Security Administration, U.S. Department of Energy. This work has been authored by employees of Triad National Security, LLC, operator of the Los Alamos National Laboratory (LANL) under Contract No. 89233218CNA000001 with the U.S. Department of Energy. The United States Government retains and the publisher, by accepting this work for publication, acknowledges that the United States Government retains a nonexclusive, paid-up, irrevocable, world-wide license to publish or reproduce this work, or allow others to do so for United States Government purposes.

9. Appendix

9.1. Appendix 1: Kinematic measures

The Green-Lagrange strain in the reference configuration is

$$\mathbf{E} = \frac{1}{2}(\mathbf{F}^T \mathbf{F} - \mathbf{I}). \quad (103)$$

Substituting for \mathbf{F} from Eq. (10) in Eq. (103) gives

$$\mathbf{E} = \mathbf{E}_e + \mathbf{E}_d + \mathbf{E}_p, \quad (104)$$

where

$$\begin{aligned} \mathbf{E}_e &= (\mathbf{F}_p)^T (\mathbf{F}_d)^T \frac{1}{2} [(\mathbf{F}_e)^T \mathbf{F}_e - \mathbf{I}] \mathbf{F}_d \mathbf{F}_p, \\ \mathbf{E}_d &= (\mathbf{F}_p)^T \frac{1}{2} [(\mathbf{F}_d)^T \mathbf{F}_d - \mathbf{I}] \mathbf{F}_p, \\ \mathbf{E}_p &= \frac{1}{2} [(\mathbf{F}_p)^T \mathbf{F}_p - \mathbf{I}]. \end{aligned} \quad (105)$$

We focus on an intermediate configuration ($\bar{\mathcal{B}}$) obtained by unloading the reversible elastic deformation \mathbf{F}_e . The Lagrangian strains in $\bar{\mathcal{B}}$ are a pull-back of strains in \mathcal{B} given by Eq. (105)

$$\begin{aligned} \bar{\mathbf{E}}_e &= \frac{1}{2} [(\mathbf{F}_e)^T \mathbf{F}_e - \mathbf{I}], \\ \bar{\mathbf{E}}_d &= (\mathbf{F}_d)^{-T} \frac{1}{2} [(\mathbf{F}_d)^T \mathbf{F}_d - \mathbf{I}] (\mathbf{F}_d)^{-1}, \\ \bar{\mathbf{E}}_p &= (\mathbf{F}_d)^{-T} (\mathbf{F}_p)^{-T} \frac{1}{2} [(\mathbf{F}_p)^T \mathbf{F}_p - \mathbf{I}] (\mathbf{F}_p)^{-1} (\mathbf{F}_d)^{-1}. \end{aligned} \quad (106)$$

The rate form of Eq. (10) is given by an additive decomposition of spatial velocity gradients in the current configuration

$$\mathbf{l} = \dot{\mathbf{F}} \mathbf{F}^{-1}. \quad (107)$$

Substituting for \mathbf{F} from Eq. (10) in Eq. (107) gives

$$\mathbf{l} = \mathbf{l}_e + \mathbf{l}_d + \mathbf{l}_p, \quad (108)$$

where

$$\begin{aligned}
\boldsymbol{l}_e &= \dot{\boldsymbol{F}}_e(\boldsymbol{F}_e)^{-1}, \\
\boldsymbol{l}_d &= \boldsymbol{F}_e[\dot{\boldsymbol{F}}_d(\boldsymbol{F}_d)^{-1}](\boldsymbol{F}_e)^{-1}, \\
\boldsymbol{l}_p &= \boldsymbol{F}_e\boldsymbol{F}_d[\dot{\boldsymbol{F}}_p(\boldsymbol{F}_p)^{-1}](\boldsymbol{F}_d)^{-1}(\boldsymbol{F}_e)^{-1}.
\end{aligned} \tag{109}$$

The symmetric parts of the velocity gradients in the current configuration \mathcal{B} are

$$\begin{aligned}
\boldsymbol{d}_e &= 0.5[\boldsymbol{l}_e + (\boldsymbol{l}_e)^T], \\
\boldsymbol{d}_d &= 0.5[\boldsymbol{l}_d + (\boldsymbol{l}_d)^T], \\
\boldsymbol{d}_p &= 0.5[\boldsymbol{l}_p + (\boldsymbol{l}_p)^T].
\end{aligned} \tag{110}$$

The velocity gradients in $\bar{\mathcal{B}}$ are pull-backs of velocity gradients in \mathcal{B} from Eq. (109)

$$\begin{aligned}
\bar{\boldsymbol{l}}_e &= (\boldsymbol{F}_e)^{-1}\dot{\boldsymbol{F}}_e, \\
\bar{\boldsymbol{l}}_d &= \dot{\boldsymbol{F}}_d(\boldsymbol{F}_d)^{-1}, \\
\bar{\boldsymbol{l}}_p &= \boldsymbol{F}_d[\dot{\boldsymbol{F}}_p(\boldsymbol{F}_p)^{-1}](\boldsymbol{F}_d)^{-1}.
\end{aligned} \tag{111}$$

The symmetric parts of the velocity gradients in configuration $\bar{\mathcal{B}}$ are

$$\begin{aligned}
\bar{\boldsymbol{d}}_e &= 0.5[\bar{\boldsymbol{C}}_e\bar{\boldsymbol{l}}_e + (\bar{\boldsymbol{l}}_e)^T\bar{\boldsymbol{C}}_e], \\
\bar{\boldsymbol{d}}_d &= 0.5[\bar{\boldsymbol{C}}_e\bar{\boldsymbol{l}}_d + (\bar{\boldsymbol{l}}_d)^T\bar{\boldsymbol{C}}_e], \\
\bar{\boldsymbol{d}}_p &= 0.5[\bar{\boldsymbol{C}}_e\bar{\boldsymbol{l}}_p + (\bar{\boldsymbol{l}}_p)^T\bar{\boldsymbol{C}}_e].
\end{aligned} \tag{112}$$

where $\bar{\boldsymbol{C}}_e = (\boldsymbol{F}_e)^T\boldsymbol{F}_e$ is the right Cauchy-Green deformation tensor for elastic deformation, which acts as a metric in configuration $\bar{\mathcal{B}}$.

The velocity gradients from Eq. (109) referred to in $\tilde{\mathcal{B}}$ are

$$\begin{aligned}
\tilde{\boldsymbol{l}}_e &= (\boldsymbol{F}_d)^{-1}(\boldsymbol{F}_e)^{-1}\dot{\boldsymbol{F}}_e\boldsymbol{F}_d, \\
\tilde{\boldsymbol{l}}_d &= (\boldsymbol{F}_d)^{-1}\dot{\boldsymbol{F}}_d, \\
\tilde{\boldsymbol{l}}_p &= \dot{\boldsymbol{F}}_p(\boldsymbol{F}_p)^{-1}.
\end{aligned} \tag{113}$$

The symmetric parts of the velocity gradients in configuration $\tilde{\mathcal{B}}$ are

$$\begin{aligned}
\tilde{\boldsymbol{d}}_e &= 0.5[\tilde{\boldsymbol{C}}_{ed}\tilde{\boldsymbol{l}}_e + (\tilde{\boldsymbol{l}}_e)^T\tilde{\boldsymbol{C}}_{ed}], \\
\tilde{\boldsymbol{d}}_d &= 0.5[\tilde{\boldsymbol{C}}_{ed}\tilde{\boldsymbol{l}}_d + (\tilde{\boldsymbol{l}}_d)^T\tilde{\boldsymbol{C}}_{ed}], \\
\tilde{\boldsymbol{d}}_p &= 0.5[\tilde{\boldsymbol{C}}_{ed}\tilde{\boldsymbol{l}}_p + (\tilde{\boldsymbol{l}}_p)^T\tilde{\boldsymbol{C}}_{ed}].
\end{aligned} \tag{114}$$

where $\tilde{\mathbf{C}}_{ed} = (\mathbf{F}_d)^T \bar{\mathbf{C}}_e \mathbf{F}_d$ acts as a metric in configuration $\tilde{\mathcal{B}}$.

The velocity gradients from Eq. (109) referred to in the reference configuration \mathcal{B}_0 are

$$\begin{aligned}\mathbf{L}_e &= (\mathbf{F}_p)^{-1} (\mathbf{F}_d)^{-1} (\mathbf{F}_e)^{-1} \dot{\mathbf{F}}_e \mathbf{F}_d \mathbf{F}_p, \\ \mathbf{L}_d &= (\mathbf{F}_p)^{-1} (\mathbf{F}_d)^{-1} \dot{\mathbf{F}}_d \mathbf{F}_p, \\ \mathbf{L}_p &= (\mathbf{F}_p)^{-1} \dot{\mathbf{F}}_p.\end{aligned}\tag{115}$$

The symmetric parts of the velocity gradients in the reference configuration \mathcal{B}_0 are

$$\begin{aligned}\mathbf{D}_e &= 0.5[\mathbf{C}_{edp} \mathbf{L}_e + (\mathbf{L}_e)^T \mathbf{C}_{edp}], \\ \mathbf{D}_d &= 0.5[\mathbf{C}_{edp} \mathbf{L}_d + (\mathbf{L}_d)^T \mathbf{C}_{edp}], \\ \mathbf{D}_p &= 0.5[\mathbf{C}_{edp} \mathbf{L}_p + (\mathbf{L}_p)^T \mathbf{C}_{edp}].\end{aligned}\tag{116}$$

where $\mathbf{C}_{edp} = (\mathbf{F}_p)^T \bar{\mathbf{C}}_{ed} \mathbf{F}_p = \mathbf{F}^T \mathbf{F}$ acts as a metric in the reference configuration \mathcal{B} .

9.2. Appendix 2: Dislocation-based plasticity

We utilize a J_2 flow theory with isotropic hardening to describe the polycrystalline response. In addition, we adopt Orowan equation (Orowan, 1948) to describe the plastic shear strain rate ($\dot{\gamma}_p$) in terms of the average dislocation velocity (\bar{v}) as follows.

$$\dot{\gamma}_p = b\rho_M\bar{v} \quad (117)$$

where b is magnitude of the Burgers vector for a dislocation and ρ_M is the mobile dislocation density.

Slip occurs on preferential glide planes and the mean dislocation velocity is in general a function of effective stress. It is assumed that the SVE contains a number of grains such that the distribution of grain orientation is uniform. For motion of a dislocation on a glide plane above the athermal stress threshold (τ_r), we adopt the expression for mean dislocation velocity based on the theory of thermally-activated dislocation glide, combined with the drag and relativistic effects at even higher stresses, given by (Clifton, 1970; Austin and McDowell, 2011)

$$\bar{v} = \frac{\bar{L}}{t_w + t_r} \quad (118)$$

where \bar{L} is the average glide distance between successive obstacles on a slip plane, t_w is the time spent waiting at an obstacle, and t_r is the time to travel the average distance between obstacles.

Dislocations act as obstacles for moving dislocations. We use \bar{L} to quantify an effective mean free path between the dislocation network, expressed as

$$\bar{L} = [c_2\rho]^{-1/2}, \quad (119)$$

where ρ is the total dislocation density, a sum of mobile ρ_M and immobile ρ_I dislocation densities. In addition, we define the initial dislocation density as a sum of initial mobile ρ_{0M} and initial immobile ρ_{0I} dislocation densities. c_2 is a weighing parameter that provides flexibility to capture the effects of obstacles due to a complex network of dislocations on intersecting slip planes (descriptions of which are accessible to a crystal plasticity framework). If $c_2 = 1$, then the dislocation density will represent an effective dislocation density accounting for all the intersecting slip planes.

In the model of thermally-activated dislocation glide, mobile dislocations move through a dislocation forest via assistance of thermal fluctuations. Additionally, these dislocations have to overcome the Peierls stress (short range), the barriers provided by the existing dislocation network and the grain boundaries (long range). So the

total resistance to deformation at zero temperature ($\theta = 0$ K) is given by

$$\tau_{0r} = \tau_{0p} + \tau_{0a} + \tau_{0t}, \quad (120)$$

where τ_{0p} is the material-specific Peierls stress, which generally decreases with temperature. The resistance to deformation due to grain boundary network for an HCP metal maybe accounted through the Hall-Petch equation (Petch and Wright, 1980)

$$\tau_{0a} = k_y \bar{d}^{-0.5} \quad (121)$$

where k_y is the material-specific Hall-Petch coefficient and \bar{d} is the average grain diameter, both at $\theta = 0$ K.

The threshold shear stress to move a dislocation against the long-range glide resistance (due to existing dislocation network) may be modeled by the Taylor hardening relation

$$\tau_{0t} = \alpha_0 m_1 G_0 b \sqrt{c_2 \rho}, \quad (122)$$

where G_0 is the shear modulus at $\theta = 0$ K, α_0 is a constant (typically ranges from 0.1 to 1, e.g. 0.2 for cubic metals), and m_1 is the Taylor hardening factor. Note, the value of the initial dislocation density has a proportional effect on the value of the yield stress.

The waiting time can be written as (Kocks and Mecking, 2003; Austin and McDowell, 2011)

$$t_w = \frac{1}{v_g} \left[\exp \left(\frac{\Delta H}{K_b \theta} \right) - 1 \right], \quad (123)$$

where v_g is the attempt frequency, θ is the temperature, ΔH is the stress-dependent free enthalpy of activation, and K_b is the Boltzmann constant. The free enthalpy of activation for the thermally-activated process is written in the empirical form suggested by (Kocks et al., 1975)

$$\Delta H = \Delta H_0 \left[1 - \left(\frac{\tau/G}{\tau_{0r}/G_0} \right)^p \right]^q, \quad (124)$$

where τ_{0r} is the *mechanical threshold*, the flow stress when the activation energy $\Delta H = 0$, i.e. at $\theta = 0$ K. Further, $\Delta H_0 = g_0 G b^3$ is the free energy required to overcome the obstacles that pin the dislocations, G is the shear modulus at a finite temperature, $\tau = \frac{\tilde{\sigma}}{\sqrt{3}}$ is the effective shear stress, $\tilde{\sigma}$ is the equivalent stress (von Mises stress) in the $\tilde{\mathcal{B}}$ configuration. Further, g_0 is a dimensionless parameter for depinning, and p and q are parameters that model dependence of the depinning process on the

applied shear stress (Kocks and Mecking, 2003).

The time to travel the average distance between obstacles is based on the kinetics of dislocation propagation, accounting for pure drag and relativistic effect, given by

$$t_r = \frac{\bar{L}}{v_r} \quad (125)$$

where $v_r = c_s h$ is the velocity of a dislocation based as a function of shear wave speed c_s . Further, the parameter h is a function of material properties and effective stress

$$h = \sqrt{\xi^2 + 1} - \xi, \quad (126)$$

and

$$\xi = \frac{B_0 c_s}{2\tau b}, \quad (127)$$

where B_0 is the nominal value of the damping (or drag) coefficient in the relativistic relation and b is the Burgers vector of the dislocation. The damping coefficient is assumed to be governed by phonon damping and expressed as

$$B_0 = \frac{3K_b \theta z}{20c_s b^2}, \quad (128)$$

where z is the number of atoms per unit cell ($z = 6$ for HCP metals).

9.3. Appendix 3: Stress update scheme for viscoplastic damage constitutive model

Backward-Euler numerical integration is employed for discretized time-evolution of field and internal variables. For a generalized three-dimensional loading condition, the following stress update scheme is used.

1. Input constants, material properties, and initialize variables. Initialize flaw normals in the reference configuration, $\mathbf{N}_{(k)}$. Prescribe time period, timestep, and the velocity gradient tensor.
2. Set the current values of variables: time t , Cauchy stress $\boldsymbol{\sigma}^t$, deformation gradient \mathbf{F}^t , elastic deformation gradient \mathbf{F}_e^t , damage deformation gradient $\tilde{\mathbf{F}}_d^t$, plastic deformation gradient $\tilde{\mathbf{F}}_p^t$, and shear modulus G^t .

3. Calculate stress in intermediate configurations

$$\begin{aligned}\bar{\mathbf{S}}^t &= J_e^t(\mathbf{F}_e^t)^{-1}\boldsymbol{\sigma}^t(\mathbf{F}_e^t)^{-T}, \\ \tilde{\mathbf{S}}^t &= J_d^t(\mathbf{F}_d^t)^{-1}\bar{\mathbf{S}}^t(\mathbf{F}_d^t)^{-T}.\end{aligned}$$

4. Calculate values of deformation gradient tensor $\mathbf{F}^{t+\Delta t}$ and Lagrangian strain tensor $\mathbf{E}^{t+\Delta t}$ in the next time step using velocity gradient tensor $\mathbf{l}^{t+\Delta t}$ and timestep Δt

$$\begin{aligned}\mathbf{F}^{t+\Delta t} &= [\mathbf{I} + \mathbf{l}^{t+\Delta t}\Delta t + 0.5(\mathbf{l}^{t+\Delta t}\Delta t)^2]\mathbf{F}^t, \\ \mathbf{E}^{t+\Delta t} &= 0.5[(\mathbf{F}^{t+\Delta t})^T\mathbf{F}^{t+\Delta t} - \mathbf{I}].\end{aligned}$$

5. Calculate plastic flow, $\dot{\rho}_M^{t+\Delta t}$, $\dot{\rho}_I^{t+\Delta t}$, and $\tilde{\mathbf{d}}_p^{t+\Delta t}$ using Eq. (98) and stress measure

$$\begin{aligned}J_p\tilde{\mathbf{S}}^t \\ J_p &= \det(\tilde{\mathbf{F}}_p^t), \\ \tilde{\mathbf{d}}_p^{t+\Delta t} &= \frac{3}{2}\frac{b\rho_M^{t+\Delta t}\bar{v}^t}{\bar{\sigma}^t} [\tilde{\mathbf{C}}_{ed}^t \cdot \text{dev}(\tilde{\mathbf{S}}^t) \cdot \tilde{\mathbf{C}}_{ed}^t].\end{aligned}$$

6. Calculate $\tilde{\mathbf{l}}_p^{t+\Delta t}$ using $\tilde{\mathbf{w}}_p^{t+\Delta t} \approx 0$ for isotropic plasticity

$$\tilde{\mathbf{l}}_p^{t+\Delta t} = \tilde{\mathbf{d}}_p^{t+\Delta t} + \tilde{\mathbf{w}}_p^{t+\Delta t}.$$

7. Calculate plastic deformation gradient

$$\tilde{\mathbf{F}}_p^{t+\Delta t} = [\mathbf{I} + \tilde{\mathbf{l}}_p^{t+\Delta t}\Delta t + 0.5(\tilde{\mathbf{l}}_p^{t+\Delta t}\Delta t)^2]\tilde{\mathbf{F}}_p^t.$$

8. Calculate push-forward of plastic rate of deformation from $\tilde{\mathcal{B}}$ to $\bar{\mathcal{B}}$ using $\bar{\mathbf{w}}_p^{t+\Delta t} \approx 0$ for isotropic plasticity and update total plastic strain in $\bar{\mathcal{B}}$,

$$\begin{aligned}
\bar{\mathbf{d}}_p^{t+\Delta t} &= (\mathbf{F}_d^{t+\Delta t})^{-T} (\tilde{\mathbf{d}}_p^{t+\Delta t}) (\mathbf{F}_d^{t+\Delta t})^{-1} \\
\bar{\mathbf{l}}_p^{t+\Delta t} &= \bar{\mathbf{d}}_p^{t+\Delta t} + \bar{\mathbf{w}}_p^{t+\Delta t}, \\
\bar{\mathbf{E}}_p^{t+\Delta t} &= \bar{\mathbf{E}}_p^t + \bar{\mathbf{d}}_p^{t+\Delta t} \Delta t.
\end{aligned}$$

9. Calculate the rate of crack growth, new crack lengths, and then calculate the rate of compliance change $\dot{\mathbb{S}}^{t+\Delta t}$ and $\mathbb{S}^{t+\Delta t}$ using $\tilde{\mathbf{S}}^t$ and push-forward of flaw normals,

$$\tilde{\mathbf{n}}_{(k)} = (\tilde{\mathbf{F}}_p^{t+\Delta t})^{-T} \mathbf{N}_{(k)} / |(\tilde{\mathbf{F}}_p^{t+\Delta t})^{-T} \mathbf{N}_{(k)}|.$$

10. Calculate the damaged stiffness matrix $\mathbb{C}^{t+\Delta t}$, the rate of damaged stiffness matrix $\dot{\mathbb{C}}^{t+\Delta t}$ (Ayyagari et al., 2018), and rate of damage deformation gradient $\dot{\bar{\mathbf{F}}}_d^{t+\Delta t}$ using Eq. (40), assuming variables $s, \bar{u}_{ls}, \varpi_3, \varpi_4$, and, ϖ_5 as time-rate dependent.

11. Calculate damage velocity gradient and updated damage deformation gradient in configuration $\bar{\mathbb{B}}$

$$\begin{aligned}
\bar{\mathbf{l}}_d^{t+\Delta t} &= \dot{\bar{\mathbf{F}}}_d^{t+\Delta t} \bar{\mathbf{F}}_d^t, \\
\bar{\mathbf{F}}_d^{t+\Delta t} &= [\mathbf{I} + \bar{\mathbf{l}}_d^{t+\Delta t} \Delta t + 0.5(\bar{\mathbf{l}}_d^{t+\Delta t} \Delta t)^2] \bar{\mathbf{F}}_d^t.
\end{aligned}$$

12. Calculate updated elastic deformation gradient tensor, elastic right Cauchy-Green deformation tensor, and elastic velocity gradient in configuration $\bar{\mathbb{B}}$

$$\begin{aligned}
\mathbf{F}_e^{t+\Delta t} &= \mathbf{F}^{t+\Delta t} (\tilde{\mathbf{F}}_p^{t+\Delta t})^{-1} (\bar{\mathbf{F}}_d^{t+\Delta t})^{-1}, \\
\bar{\mathbf{C}}_e^{t+\Delta t} &= (\mathbf{F}_e^{t+\Delta t})^T \mathbf{F}_e^{t+\Delta t}, \\
\bar{\mathbf{l}}_e^{t+\Delta t} &= [(\mathbf{F}_e^{t+\Delta t})^{-1} (\mathbf{l}^{t+\Delta t}) \mathbf{F}_e^{t+\Delta t}] - \bar{\mathbf{l}}_d^{t+\Delta t} - \bar{\mathbf{l}}_p^{t+\Delta t}.
\end{aligned}$$

13. Calculate symmetric part of damage velocity gradient and updated damage strain in configuration $\bar{\mathbb{B}}$

$$\begin{aligned}
\bar{\mathbf{d}}_d^{t+\Delta t} &= 0.5[\bar{\mathbf{C}}_e^{t+\Delta t} (\bar{\mathbf{l}}_d^{t+\Delta t}) + (\bar{\mathbf{l}}_d^{t+\Delta t})^T \bar{\mathbf{C}}_e^{t+\Delta t}], \\
\bar{\mathbf{E}}_d^{t+\Delta t} &= \bar{\mathbf{E}}_d^t + \bar{\mathbf{d}}_d^{t+\Delta t} \Delta t.
\end{aligned}$$

14. Calculate updated elastic Lagrangian strain tensor using push-forward of total Lagrangian strain tensor in configuration $\bar{\mathbb{B}}$

$$\begin{aligned}
\bar{\mathbf{E}}^{t+\Delta t} &= (\bar{\mathbf{F}}_d^{t+\Delta t})^{-T} (\tilde{\mathbf{F}}_p^{t+\Delta t})^{-T} \{0.5[(\mathbf{F}^{t+\Delta t})^T \mathbf{F}^{t+\Delta t} - \mathbf{I}]\} (\tilde{\mathbf{F}}_p^t)^{-1} (\bar{\mathbf{F}}_d^t)^{-1}, \\
\bar{\mathbf{E}}_e^{t+\Delta t} &= \bar{\mathbf{E}}^{t+\Delta t} - \bar{\mathbf{E}}_d^{t+\Delta t} - \bar{\mathbf{E}}_p^{t+\Delta t}.
\end{aligned}$$

15. Calculate the rate of elastic Lagrangian strain tensor using pull-back of the symmetric part of velocity gradient in configuration $\bar{\mathbb{B}}$

$$\begin{aligned}\dot{\bar{\mathbf{E}}}^{t+\Delta t} &= (\mathbf{F}_e^{t+\Delta t})^T 0.5[(\mathbf{l}^{t+\Delta t})^T + \mathbf{l}^{t+\Delta t}] \mathbf{F}_e^t, \\ \dot{\bar{\mathbf{E}}}_e^{t+\Delta t} &= \dot{\bar{\mathbf{E}}}^{t+\Delta t} - \bar{\mathbf{d}}_d^{t+\Delta t} - \bar{\mathbf{d}}_p^{t+\Delta t}.\end{aligned}$$

16. Calculate rate of second Piola-Kirchhoff stress in configuration $\bar{\mathcal{B}}$

$$\dot{\bar{\mathbf{S}}}^{t+\Delta t} = \dot{\mathbb{C}}^{t+\Delta t} \cdot \bar{\mathbf{E}}_e^{t+\Delta t} + \mathbb{C}^{t+\Delta t} \cdot \dot{\bar{\mathbf{E}}}_e^{t+\Delta t}.$$

17. Calculate updated second Piola-Kirchhoff stress in configuration $\bar{\mathcal{B}}$

$$\bar{\mathbf{S}}^{t+\Delta t} = \bar{\mathbf{S}}^t + \dot{\bar{\mathbf{S}}}^{t+\Delta t} \Delta t.$$

18. Calculate updated Cauchy stress from push-forward of second Piola-Kirchhoff stress in configuration \mathcal{B}

$$\begin{aligned}J_e^{t+\Delta t} &= \det \mathbf{F}_e^{t+\Delta t}, \\ \boldsymbol{\sigma}^{t+\Delta t} &= (J_e^{t+\Delta t})^{-1} (\mathbf{F}_e^{t+\Delta t}) \bar{\mathbf{S}}^{t+\Delta t} (\mathbf{F}_e^{t+\Delta t})^T.\end{aligned}$$

19. Calculate temperature increase using dissipated power conjugate in configuration $\bar{\mathcal{B}}$ and update temperature

$$\begin{aligned}\Delta \theta &= Q \frac{\Delta t}{\bar{C}_v \rho^{t+\Delta t} J_e^{t+\Delta t}} [(\bar{\mathbf{C}}_e^{t+\Delta t} \bar{\mathbf{S}}^{t+\Delta t} \bar{\mathbf{C}}_e^{t+\Delta t}) : (\bar{\mathbf{d}}_d^{t+\Delta t} + \bar{\mathbf{d}}_p^{t+\Delta t})], \\ \theta^{t+\Delta t} &= \Delta \theta + \theta^t.\end{aligned}$$

References

- Ablen, S., Field, R., Mataya, M., 1995. Elevated temperature stress-strain behavior of beryllium powder product, in: 2nd IEA International workshop on beryllium technology for fusion, Jackson Hole, pp. 1–33.
- Anahid, M., Samal, M.K., Ghosh, S., 2011. Dwell fatigue crack nucleation model based on crystal plasticity finite element simulations of polycrystalline titanium alloys. *Journal of the Mechanics and Physics of Solids* 59, 2157–2176. URL: <http://dx.doi.org/10.1016/j.jmps.2011.05.003>, doi:10.1016/j.jmps.2011.05.003.
- Anderson, P., Hirth, J., Lothe, J., 2017. *Theory of Dislocations*. Cambridge University Press.
- Armstrong, R.W., 1968. Theory of the tensile ductile-brittle behavior of polycrystalline h.c.p. materials, with application to beryllium. *Acta Metallurgica* 16, 347–355. doi:10.1016/0001-6160(68)90021-7.
- Austin, R.A., McDowell, D.L., 2011. A dislocation-based constitutive model for viscoplastic deformation of fcc metals at very high strain rates. *International Journal of Plasticity* .
- Ayyagari, R.S., Daphalapurkar, N.P., Ramesh, K.T., 2018. The effective compliance of spatially evolving planar wing-cracks. *Journal of the Mechanics and Physics of Solids* 111, 503–529.
- Barker, L.M., Jones, A.H., Chou, S.C., 1987. Fracture toughness of CIP-HIP Beryllium at elevated temperatures. *Theoretical and Applied Fracture Mechanics* 7, 45–49.
- Becker, R., Lloyd, J.T., 2016. A reduced-order crystal model for HCP metals: Application to Mg. *Mechanics of Materials* 98, 98–110. doi:10.1016/j.mechmat.2016.04.009.
- Belytschko, T., Liu, W., Moran, B., Elkhodary, K., 2014. *Nonlinear Finite Elements for Continua and Structures, Second Edition*. John Wiley Sons, Ltd.
- Bertin, N., Cai, W., 2018. Energy of periodic discrete dislocation networks. *Journal of the Mechanics and Physics of Solids* .

- Beyerlein, I.J., Tomé, C.N., 2008. A dislocation-based constitutive law for pure Zr including temperature effects. *International Journal of Plasticity* 24, 867–895. doi:10.1016/j.ijplas.2007.07.017.
- Blaschke, D., 2019. Properties of dislocation drag from phonon wind at ambient conditions URL: <https://arxiv.org/abs/1902.02451>.
- Blumenthal, W.R., Abeln, S.P., Cannon, D.D., Gray, G.T., Carpenter, R.W., 1998. Influence of strain rate and temperature on the mechanical behavior of beryllium. *Shock Compression of Condensed Matter-1997*, AIP Conference Proceedings 429, 411–414.
- Bratov, V., Borodin, E.N., 2015. Comparison of dislocation density based approaches for prediction of defect structure evolution in aluminium and copper processed by ECAP. *Materials Science and Engineering A* 631, 10–17. doi:10.1016/j.msea.2015.02.019.
- Brown, D.W., Clausen, B., Sisneros, T.A., Balogh, L., Beyerlein, I.J., 2013. In situ neutron diffraction measurements during annealing of deformed beryllium with differing initial textures. *Metallurgical and Materials Transactions A: Physical Metallurgy and Materials Science* doi:10.1007/s11661-013-1932-3.
- Buckley, D.H., 1966. Effect of orientation on friction characteristics of single crystal Beryllium in vacuum. Technical Report. National Aeronautics and Space Administration.
- Cady, C.M., Liu, C., Trujillo, C.P., Brown, D.W., Iii, G.T.G., 2018. The Shear Response of Beryllium as a Function of Temperature and Strain Rate. *DYMAT, EPJ Web of Conferences* 183, 1–6. doi:10.1051/epjconf/201818302017.
- Cai, W., Arsenlis, A., Weinberger, C.R., Bulatov, V.V., 2006. A non-singular continuum theory of dislocations. *Journal of the Mechanics and Physics of Solids* 54, 561–587.
- Chen, D., Costello, L.L., Geller, C.B., Zhu, T., McDowell, D.L., 2019. Atomistic modeling of dislocation cross-slip in nickel using free-end nudged elastic band method. *Acta Materialia* 168, 436–447.
- Clayton, J.D., 2009. A continuum description of nonlinear elasticity, slip and twinning, with application to sapphire 465, 307–334. doi:10.1098/rspa.2008.0281.

- Clayton, J.D., Bammann, D.J., McDowell, D.L., 2005. A geometric framework for the kinematics of crystals with defects. *Philosophical Magazine* doi:10.1080/14786430500363312.
- Clayton, J.D., Hartley, C.S., McDowell, D.L., 2014. The missing term in the decomposition of finite deformation. *International Journal of Plasticity* 52, 51–76. URL: <http://dx.doi.org/10.1016/j.ijplas.2013.04.009>, doi:10.1016/j.ijplas.2013.04.009.
- Clayton, J.D., McDowell, D.L., 2003. Finite polycrystalline elastoplasticity and damage: Multiscale kinematics. *International Journal of Solids and Structures* doi:10.1016/S0020-7683(03)00317-2.
- Clifton, R.J., 1970. On the analysis of elastic/visco-plastic waves of finite uniaxial strain. In: Burke, J.J., Weiss, V. (Eds.), *Shock Waves and the Mechanical Properties of Solids*. Syracuse University Press, Syracuse, NY , 73–116.
- Daphalapurkar, N.P., Ramesh, K.T., 2012. Orientation dependence of the nucleation and growth of partial dislocations and possible twinning mechanisms in aluminum. *Journal of the Mechanics and Physics of Solids* 60, 277–294. URL: <http://dx.doi.org/10.1016/j.jmps.2011.10.009>, doi:10.1016/j.jmps.2011.10.009.
- Daphalapurkar, N.P., Ramesh, K.T., Graham-Brady, L., Molinari, J.F., 2011. Predicting variability in the dynamic failure strength of brittle materials considering pre-existing flaws. *Journal of the Mechanics and Physics of Solids* , 297–319.
- Daphalapurkar, N.P., Wilkerson, J.W., Wright, T.W., Ramesh, K.T., 2014. Kinetics of a fast moving twin boundary in nickel. *Acta Materialia* 68, 82–92. URL: <http://dx.doi.org/10.1016/j.actamat.2014.01.010>, doi:10.1016/j.actamat.2014.01.010.
- Davoudi, K.M., Vlassak, J.J., 2018. Dislocation evolution during plastic deformation: Equations vs. discrete dislocation dynamics study. *Journal of Applied Physics* 123. doi:10.1063/1.5013213.
- Dawu, X., Zhicong, Q., Xiangchao, W., Lifeng, H., 2016. Compressive deformation behaviors of beryllium. *Explosion and shock waves* 36, 285–288.
- Deshpande, V.S., Evans, A.G., 2008. Inelastic deformation and energy dissipation in ceramics: A mechanism-based constitutive model. *Journal of the Mechanics and Physics of Solids* 56, 3077–3100. doi:10.1016/j.jmps.2008.05.002.

- Deshpande, V.S., Gamble, E.A.N., Compton, B.G., McMeeking, R.M., Evans, A.G., Zok, F.W., 2011. A constitutive description of the inelastic response of ceramics. *Journal of the American Ceramic Society* 94, 204–214. doi:10.1111/j.1551-2916.2011.04516.x.
- Einstein, H.H., Ghahreman, B., 1995. Coalescence of fractures under shear stress experiments. *Journal of Geophysical Research* 100, 5975–5990.
- Eshelby, J., Frank, F., Nabarro, F., 1951. The equilibrium of linear arrays of dislocations. *The London, Edinburgh, and Dublin Philosophical Magazine and Journal of Science* 42, 351–364. URL: <http://www.tandfonline.com/doi/abs/10.1080/14786445108561060>, doi:10.1080/14786445108561060.
- Estrin, Y., Kubin, L.P., 1986. Local strain hardening and nonuniformity of plastic deformation. *Acta Metallurgica* 34, 2455–2464. doi:10.1016/0001-6160(86)90148-3.
- Follansbee, P.S., Kocks, U.F., 1988. A constitutive description of the deformation of alpha uranium based on the use of the mechanical threshold stress as a state variable. *Acta Metallurgica* 36, 81–93. URL: <http://www.sciencedirect.com/science/article/pii/0001616088900302>, doi:10.1016/0001-6160(88)90030-2.
- Freund, L.B., 1972. Crack propagation in an elastic solid subjected to general loading-II. Non-uniform rate of extension. *Journal of the Mechanics and Physics of Solids* 20, 141–152.
- Gandhi, C., Ashby, M.F., 1979. Overview no. 5. Fracture-mechanism maps for materials which cleave: F.C.C., B.C.C. and H.C.P. metals and ceramics. *Acta Metallurgica* 27, 1565–1602. doi:10.1016/0001-6160(79)90042-7.
- Gardner, R.N., Pollock, T.C., Wilsdorf, H.G., 1977. Crack initiation at dislocation cell boundaries in the ductile fracture of metals. *Materials Science and Engineering* 29, 169–174. doi:10.1016/0025-5416(77)90123-9.
- Govila, R.K., Kamdar, M.H., 1970. Cleavage in beryllium monocrystals. *Metallurgical Transactions* doi:10.1007/BF02811786.
- Grechka, V., Kachanov, M., 2006. Effective elasticity of fractured rocks: A snapshot of the work in progress. *Geophysics* 71, W45–W58.

- Green, A.P., Sawkill, J., 1961. Plastic anisotropy and fracture in beryllium. *Journal of Nuclear Materials* 3, 101–110.
- Greenspan, J., 1957. Ductility in Beryllium related to grain size orientation and grain size. Technical Report.
- Griffith, A., 1920. The phenomena of rupture and flow in solid. *Philosophical Transactions A* 221, 163–198.
- Hill, R., 1972. On constitutive macro-variables for heterogeneous solids at finite strain. *Proceedings of the Royal Society of London A: Mathematical, Physical and Engineering Sciences* 326, 131–147. doi:10.1098/rspa.1972.0001.
- Hoge, K.G., Mukherjee, A.K., 1977. The temperature and strain rate dependence of the flow stress of tantalum. *Journal of Materials Science* 12, 1666–1672. doi:10.1007/BF00542818.
- Hu, G., Liu, J., Graham-Brady, L., Ramesh, K., 2015. A 3d mechanistic model for brittle materials containing evolving flaw distributions under dynamic multiaxial loading. *Journal of the Mechanics and Physics of Solids* 78, 269–297.
- Huang, C., Subhash, G., 2003. Influence of lateral confinement on dynamic damage evolution during uniaxial compressive response of brittle solids. *Journal of the Mechanics and Physics of Solids* 51, 1089–1105. doi:10.1016/S0022-5096(03)00002-4.
- Hull, D., Bacon, D., 2011. *Introduction to dislocations* (fifth edition). Butterworth-Heinemann, USA.
- Irwin, G.R., 1957. Analysis of Stresses and Strains Near the End of a Crack Traversing a Plate. *J. Appl. Mech.* .
- Johnson, G., Cook, W., 1983. A constitutive model and data for metals subjected to large strains high strain rates and high temperatures, in: *Proceedings of the Seventh International Symposium on Ballistics*, The Hague, The Netherlands, pp. 541–548.
- Johnson, G.R., Cook, W.H., 1985. Fracture characteristics of three metals subjected to various strains, strain rates, temperatures and pressures. *Engineering Fracture Mechanics* 21, 31–48. doi:10.1016/0013-7944(85)90052-9.

- Johnston, T.L., Stokes, R.J., Li, C.H., 1962. Crack nucleation in magnesium oxide bi-crystals under compression. *Philosophical Magazine* 7, 23–34.
- Johnston, W.G., Gilman, J.J., 1960. Dislocation multiplication in lithium fluoride crystals. *Journal of Applied Physics* 31, 632–643. doi:10.1063/1.1735655.
- Kachanov, M., 1980. Continuum model of medium with cracks. *Journal of Engineering Mechanics* 106, 1039–1051.
- Kachanov, M., Sevostianov, I., 2013. Effective Properties of Heterogeneous Materials. doi:10.1007/978-94-007-5715-8.
- Kamdar, M.H., 1971. Cleavage in zinc. *Metallurgical Transactions* 2, 485–489.
- Kanninen, M.F., Mukherjee, A.K., Rosenfield, A.R., Hahn, G.T., 1968. The Speed of Ductile-Crack Propagation and the Dynamics of Flow in Metals. Springer Berlin Heidelberg, Berlin, Heidelberg. pp. 96–133.
- Kimberley, J., Ramesh, K., Daphalapurkar, N., 2013. A scaling law for the dynamic strength of brittle solids. *Acta Materialia* 61. doi:10.1016/j.actamat.2013.02.045.
- Klopp, R.W., Clifton, R.J., Shawki, T.G., 1985. Pressure-shear impact and the dynamic viscoplastic response of metals. *Mechanics of Materials* 4, 375–385. doi:10.1016/0167-6636(85)90033-X.
- Kocks, U.F., 1966. A statistical theory of flow stress and work-hardening. *Philosophical Magazine* 13, 541–566. doi:10.1080/14786436608212647.
- Kocks, U.F., Argon, A.S., Ashby, M.F., 1975. Thermodynamics and Kinetics of Slip. volume 19. Pergamon Press, Oxford.
- Kocks, U.F., Mecking, H., 2003. Physics and phenomenology of strain.pdf. *Progress in Materials Science* 48, 171–273. doi:10.4324/9781315279015.
- Lawn, B.R., Dabbs, T.P., Fairbanks, C.J., 1983. Kinetics of shear-activated indentation crack initiation in soda-lime glass. *Journal of Materials Science* 18, 2785–2797. doi:10.1007/BF00547596.
- Leong, A.F.T., Robinson, A.K., Fezzaa, K., Sun, T., Sinclair, N., Casem, D.T., Ramesh, K.T., Lambert, P.K., Hustedt, C.J., Daphalapurkar, N.P., Hufnagel, T.C., 2018. Quantitative in situ studies of dynamic fracture in brittle solids using dynamic X-ray phase contrast imaging. *Experimental Mechanics* doi:10.1007/s11340-018-0414-3.

- Liu, J., Graham-Brady, L., 2016. Effective anisotropic compliance relationships for wing-cracked brittle materials under compression. *IJSS* 100-101, 158–168.
- Lloyd, J.T., 2018. A dislocation-based model for twin growth within and across grains. *Proceedings of the Royal Society A: Mathematical, Physical and Engineering Sciences* 474. doi:10.1098/rspa.2017.0709.
- Lloyd, J.T., Clayton, J.D., Austin, R.A., McDowell, D.L., 2014. Plane wave simulation of elastic-viscoplastic single crystals. *Journal of the Mechanics and Physics of Solids* 69, 14–32. URL: <http://dx.doi.org/10.1016/j.jmps.2014.04.009>, doi:10.1016/j.jmps.2014.04.009.
- Luscher, D.J., Addressio, F.L., Cawkwell, M.J., Ramos, K.J., 2017. A dislocation density-based continuum model of the anisotropic shock response of single crystal α -cyclotrimethylene trinitramine. *Journal of the Mechanics and Physics of Solids* 98, 63–86. URL: <http://dx.doi.org/10.1016/j.jmps.2016.09.005>, doi:10.1016/j.jmps.2016.09.005.
- Luscher, D.J., Buechler, M.A., Walters, D.J., Bolme, C.A., Ramos, K.J., 2018. On computing the evolution of temperature for materials under dynamic loading. *International Journal of Plasticity* , 0–1 URL: <https://doi.org/10.1016/j.ijplas.2018.07.014>, doi:10.1016/j.ijplas.2018.07.014.
- Ma, A., Roters, F., 2004. A constitutive model for fcc single crystals based on dislocation densities and its application to uniaxial compression of aluminium single crystals. *Acta Materialia* 52, 3603–3612. doi:10.1016/j.actamat.2004.04.012.
- Mecking, H., Kocks, U.F., 1981. Kinetics of flow and strain-hardening. *Acta Metallurgica* 29, 1865–1875.
- Murakami, S., 1983. Notion of continuum damage mechanics and its application to anisotropic creep damage theory. *Journal of Engineering Materials and Technology* 105, 99–105.
- Nadal, M.H., Bourgeois, L., 2010. Elastic moduli of beryllium versus temperature: Experimental data updating. *Journal of Applied Physics* 108. doi:10.1063/1.3455859.
- Nemat-Nasser, S., 1985. Discussion of Geometric probability approach to the characterization and analysis of microcracking in rocks. *Mechanics of Material* 4, 277–281.

- Nemat-Nasser, S., Obata, M., 1988. A microcrack model of dilatancy in brittle materials. *Journal of applied mechanics* 55, 24–35.
- Nemeth, N.N., 2014. Probability density distribution of the orientation of strength-controlling flaws from multiaxial loading using the unit-sphere stochastic strength model for anisotropy. *International Journal of Fracture* 185, 97–114. doi:10.1007/s10704-013-9906-4.
- Nes, E., Pettersen, T., Marthinsen, K., 2000. On the mechanisms of work hardening and flow-stress saturation. *Scripta Materialia* 43, 55–62. doi:10.1016/S1359-6462(00)00363-8.
- Nguyen, T., Luscher, D.J., Wilkerson, J.W., 2017. A dislocation-based crystal plasticity framework for dynamic ductile failure of single crystals. *Journal of the Mechanics and Physics of Solids* 108, 1–29. URL: <http://dx.doi.org/10.1016/j.jmps.2017.07.020>, doi:10.1016/j.jmps.2017.07.020.
- Nicholas, T., 1975. Mechanical properties of structural grades of Beryllium at high strain rates. AFML-TR-75-168 U.S. Air F, 1–34.
- Nicolas, A., Fortin, J., Gueguen, Y., 2017. Micromechanical constitutive model for low temperature constant strain rate deformation of limestones in the brittle and semibrittle regime. *Geophysical Journal International* , 300–321.
- Oudriss, A., Feaugas, X., 2016. Length scales and scaling laws for dislocation cells developed during monotonic deformation of (001) nickel single crystal. *International Journal of Plasticity* 78, 187–202.
- Paliwal, B., Ramesh, K., 2008. An interacting micro-crack damage model for failure of brittle materials under compression. *Journal of the Mechanics and Physics of Solids* 56, 896–923.
- Paliwal, B., Ramesh, K.T., McCauley, J.W., 2006. Direct observation of the dynamic compressive failure of a transparent polycrystalline ceramic (AION). *Journal of the American Ceramic Society* 89, 2128–2133. doi:10.1111/j.1551-2916.2006.00965.x.
- Palmer, A.C., Rice, J.R., 1973. The Growth of Slip Surfaces in the Progressive Failure of Over-Consolidated Clay. *Proceedings of the Royal Society A: Mathematical, Physical and Engineering Sciences* 332, 527–548.

- Papirov, I.I., Stoev, P.I., Tikhinskii, G.F., 1979. Failure of single crystals of beryllium. Translated from *Problemy Prochnosti* , 86–91.
- Park, C.H., Bobet, A., 2010. Crack initiation, propagation and coalescence from frictional flaws in uniaxial compression. *Engineering Fracture Mechanics* 77, 2727–2748. URL: <http://dx.doi.org/10.1016/j.engfracmech.2010.06.027>, doi:10.1016/j.engfracmech.2010.06.027.
- Park, T., Voyiadjis, G., 1998. Kinematic description of damage. *Journal of applied mechanics* 65, 93–98.
- Petch, N.J., Wright, E., 1980. The plasticity and cleavage of polycrystalline beryllium I. Yield and flow stress. *Proc. R. Soc. Lond. A* 370, 17–27.
- Pollock, J.T., Hurley, G.F., 1973. Dependence of room temperature fracture strength on strain-rate in sapphire. *Journal of Materials Science* 8, 1595–1602.
- Pollock, T.C., Wilsdorf, H.G.F., 1983. Beryllium Fracture Observed by In Situ High Voltage Electron Microscopy. *Materials Science and Engineering* 61, 7–15.
- Regnier, P., Dupouy, J.M., 1970. Prismatic Slip in Beryllium and the Relative Ease of Glide in H.C.P. Metals. *physica status solidi (b)* .
- Rhee, M., Zbib, H., Hirth, J., Huang, H., de la Rubia, T., 1998. Models for long- / short-range interactions and cross slip in 3D dislocation simulation of BCC single crystals. *Modelling and Simulation in Materials Science and Engineering* 6, 467–492.
- Rice, J.R., 1968. A path dependent integral and the approximate analysis of strain concentration by notches and cracks. *Journal of Applied Mechanics* 35, 379–386.
- Rollett, A.D., Kocks, U., 1993. A Review of the Stages of Work Hardening. *Solid State Phenomena* 35-36, 1–18. doi:10.4028/www.scientific.net/ssp.35-36.1.
- Roters, F., Raabe, D., Gottstein, G., 2000. Microstructural Approach Based on Three. *Acta Materialia* 48, 4181–4189.
- Sarfarazi, M., Ghosh, S.K., 1987. On the micromechanical theories of stressinduced cleavage microcracking in crystalline solids. *Engineering Fracture Mechanics* 27, 215–230.

- Scheidler, M., Wright, T.W., 2001. A continuum framework for finite viscoplasticity. *International Journal of Plasticity* 17, 1033–1085. doi:10.1016/S0749-6419(00)00080-2.
- Sisneros, T.A., Brown, D.W., Clausen, B., Donati, D.C., Kabra, S., Blumenthal, W.R., Vogel, S.C., 2010. Influence of strain rate on mechanical properties and deformation texture of hot-pressed and rolled beryllium. *Materials Science and Engineering A* doi:10.1016/j.msea.2010.04.035.
- Smith, E., Barnby, J., 1967. Crack nucleation in crystalline solids. *Metal Science Journal* 1, 56–64.
- Steinberg, D.J., Cochran, S.G., Guinan, M.W., 1980. A constitutive model for metals applicable at high-strain rate. *Journal of Applied Physics* 51, 1498–1504.
- Stokes, R.J., Johnston, T.L., Li, C.H., 1958. Crack formation in magnesium oxide single crystals. *Philosophical Magazine* 3, 718–725.
- Stroh, A.N., 1954. The Formation of Cracks as a Result of Plastic Flow. *Proceedings of the Royal Society A: Mathematical, Physical and Engineering Sciences* 223, 404–414.
- Stroh, A.N., 1957. A theory of the fracture of metals. volume 6. doi:10.1080/00018735700101406.
- Stroh, A.N., 1958. The cleavage of metal single crystals. *Philosophical Magazine* 3, 597–606.
- Taylor, W., Moore, A., 1964. Tensile deformation modes in polycrystalline beryllium near the ductile-brittle transition. *Journal of Nuclear Materials* 13, 23–27. doi:10.1016/0022-3115(64)90062-5.
- Terlinde, G., Luetjering, G., Luetjering, G., 1982. Influence of Grain Size and Age-Hardening on Dislocation Pile-Ups and Tensile Fracture for a Ti-Al Alloy. *Metallurgical Transactions A* 13, 1283–1292. URL: <http://dx.doi.org/10.1007/BF02645512>, doi:10.1007/BF02645512.
- Westlake, D.G., 1963. Initiation and propagation of microcracks in crystals of zirconium-hydrogen alloys. *Am. Soc. Metals, Trans. Quart.* 56, 1–19.
- Wilhelm, M., Aldinger, F., 1976. Influence of copper additions on the basal cleavage in beryllium single crystals at room temperature. *Metallurgical Transactions A* 7, 695–701. doi:10.1007/BF03186801.

- Wilsdorf, H.G., 1983. The ductile fracture of metals: A microstructural viewpoint. *Materials Science and Engineering* 59, 1–39. doi:10.1016/0025-5416(83)90085-X.
- Winey, J.M., Gupta, Y.M., 2014. Shock wave compression of hexagonal-close-packed metal single crystals: Time-dependent, anisotropic elastic-plastic response of beryllium. *Journal of Applied Physics* 116.
- Wong, T.F., 1990. A Note on the Propagation Behavior of a Crack Nucleated by a Dislocation Pileup. *Journal of Geophysical Research* 95, 8639–8646.
- Zener, C., 1948. *Fracturing of Metals*. American Society for Metals.

Table 2: List of material properties and microstructure inputs for beryllium

Constant	Value	Units	Description
ν	0.06	-	Poisson's ratio (Nadal and Bourgeois, 2010)
E	286.2×10^9	N m^{-2}	elastic modulus
ρ_0	1850	kg m^{-3}	density
C_v	1.925×10^{-3}	$\text{N m kg}^{-1} \text{ }^\circ\text{C}^{-1}$	specific heat
θ_m	1560	K	melting temperature
c_d	13123	m s^{-1}	ambient 1D wave speed
c_s	8542	m s^{-1}	ambient shear wave speed
c_r	7726	m s^{-1}	ambient Rayleigh wave speed
σ_c	8×10^8	N m^{-2}	cleavage strength (Greenspan, 1957)
$G_c = 2\gamma_s$	2.1	N m^{-1}	fracture energy (Govila and Kamdar, 1970)
μ_f	0.5	-	friction coefficient (Buckley, 1966)
b	2.29×10^{-10}	m	Burgers vector, basal dislocation
d	11.4×10^{-6}	m	average grain size (Blumenthal et al., 1998)

Table 3: Parameters for pressure- and temperature-dependent shear modulus for beryllium (Steinberg et al., 1980)

Constant	Value	Units	Description
G_a	135×10^9	N m^{-2}	ambient shear modulus
p_a	0	GPa	ambient pressure
θ_a	300	K	ambient temperature
$\left(\frac{1}{G_a} \frac{\partial G}{\partial p}\right)$	15.5×10^{-3}	GPa^{-1}	-
$\left(\frac{1}{G_a} \frac{\partial G}{\partial \theta}\right)$	-0.26×10^{-3}	K^{-1}	-

Table 4: Calibrated parameters for the dislocation plasticity model for beryllium

Constant	Value	Units	Reference/rationale/calibration
ρ_{0M}	1×10^{10}	m^{-2}	initial mobile dislocation density; calibrated
ρ_{0I}	1×10^{10}	m^{-2}	initial immobile dislocation density; calibrated
α_0	0.2	-	Taylor constant (Petch and Wright, 1980)
m_1	4.3	-	Taylor factor (Petch and Wright, 1980)
c_2	1	-	interaction of dislocations
c_3	1	-	fraction of dislocations in a pileup
c_4	3.1×10^{-5}	-	multiplier for trapping; calibrated
c_5	0.07	-	constant for trapping; calibrated
c_6	1	-	annihilation coefficient; calibrated
v_g	9.5×10^{10}	s^{-1}	attempt frequency
K_b	1.38×10^{-23}	N m K^{-1}	Boltzmann constant
g_0	0.32	-	energy barrier coefficient (Chen et al., 2019)
B_0	5×10^{-5}	N s m^{-2}	phonon drag viscosity (HCP) (Blaschke, 2019)
p	0.5	-	barrier shape parameter; calibrated
q	1.5	-	barrier shape parameter; calibrated
τ_0	14×10^6	N m^{-2}	Peierls stress (Basal) (Green and Sawkill, 1961)
ρ_{satI}	3×10^{15}	m^{-2}	saturation density (Oudriss and Feaugas, 2016)
ρ_{satM}	3×10^{14}	m^{-2}	saturation density (Oudriss and Feaugas, 2016)
α_{mult}	18×10^3	-	multiplication coefficient; calibrated
$\dot{\epsilon}_{0tp}$	1	s^{-1}	reference rate for trapping; calibrated
Q	0.9	-	Taylor-Quinney factor
k_y	10	$\text{MPa mm}^{1/2}$	Hall-Petch coefficient (Petch and Wright, 1980)

Table 5: Calibrated parameters for the brittle damage model for beryllium

Constant	Value	Units	Reference/rationale/calibration
d_1	4	-	crack speed limit parameter (Kanninen et al., 1968)
d_2	8	-	crack kinetics exponent; calibrated
τ_{0coh}	14×10^6	N m^{-2}	cohesive resistance in shear (Green and Sawkill, 1961)
η_{coh}	0.05	-	decaying factor (Nemat-Nasser and Obata, 1988)
L_{ps}	1.55×10^{-6}	m	average cell size (Pollock and Wilsdorf, 1983)
η	10^7	m^{-3}	crack density; calibrated
α_2	$[0, \pi/2]$	radians	crack-normal angle with Y-axis
θ_2	$[0, 2\pi]$	radians	crack-normal angle with X-axis in XZ-plane
n^{α_2}	2	-	divisions of α_2
n^{θ_2}	8	-	divisions of θ_2

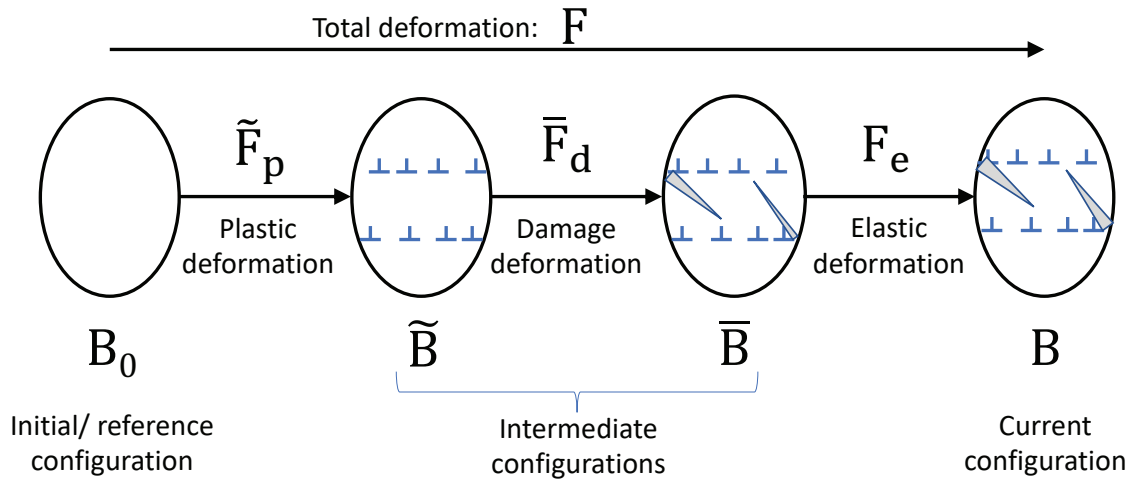


Figure 1: Multiplicative decomposition of deformation gradient tensor into plastic, damage, and elastic deformation tensors.

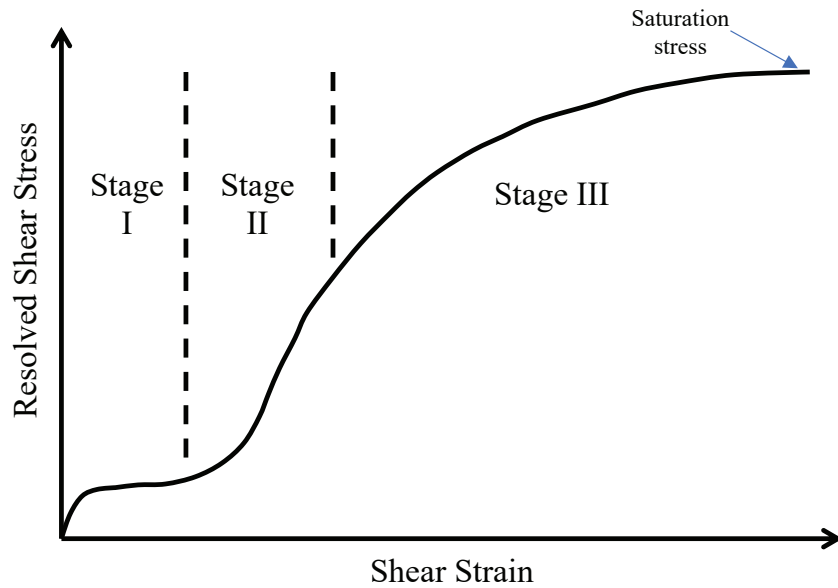


Figure 2: Schematic illustrating various Stages of work hardening for plastic flow in a single crystal metal.

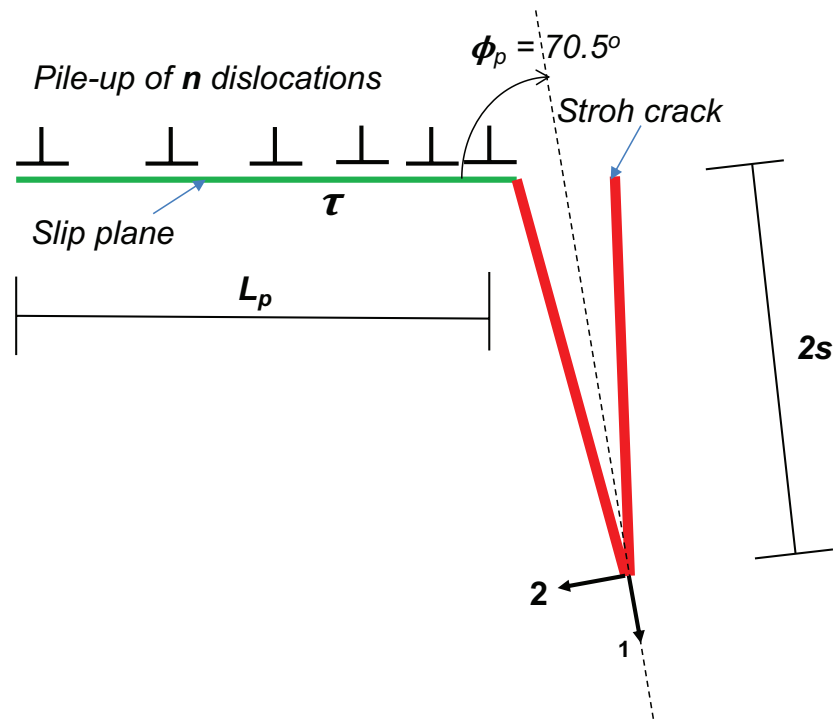


Figure 3: Schematic of Stroh crack nucleated at the head of a dislocation pileup.

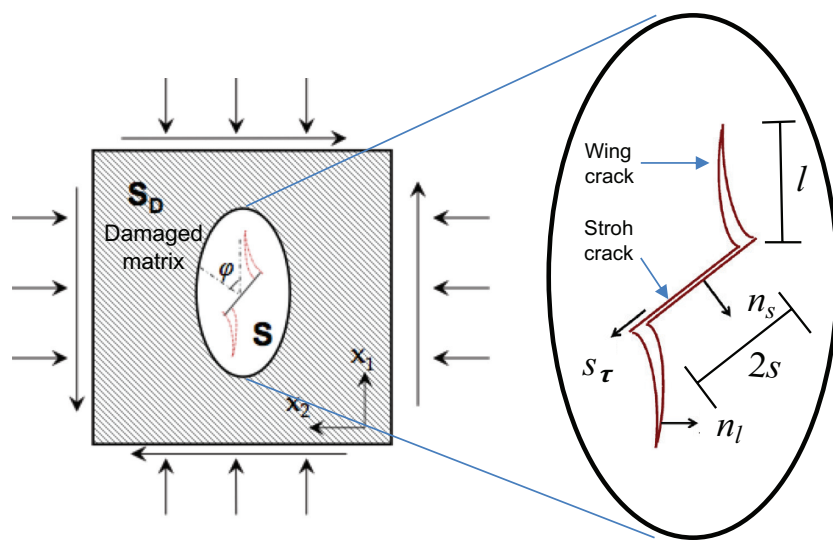


Figure 4: Schematic showing growth of wing cracks due to sliding on the Stroh crack.

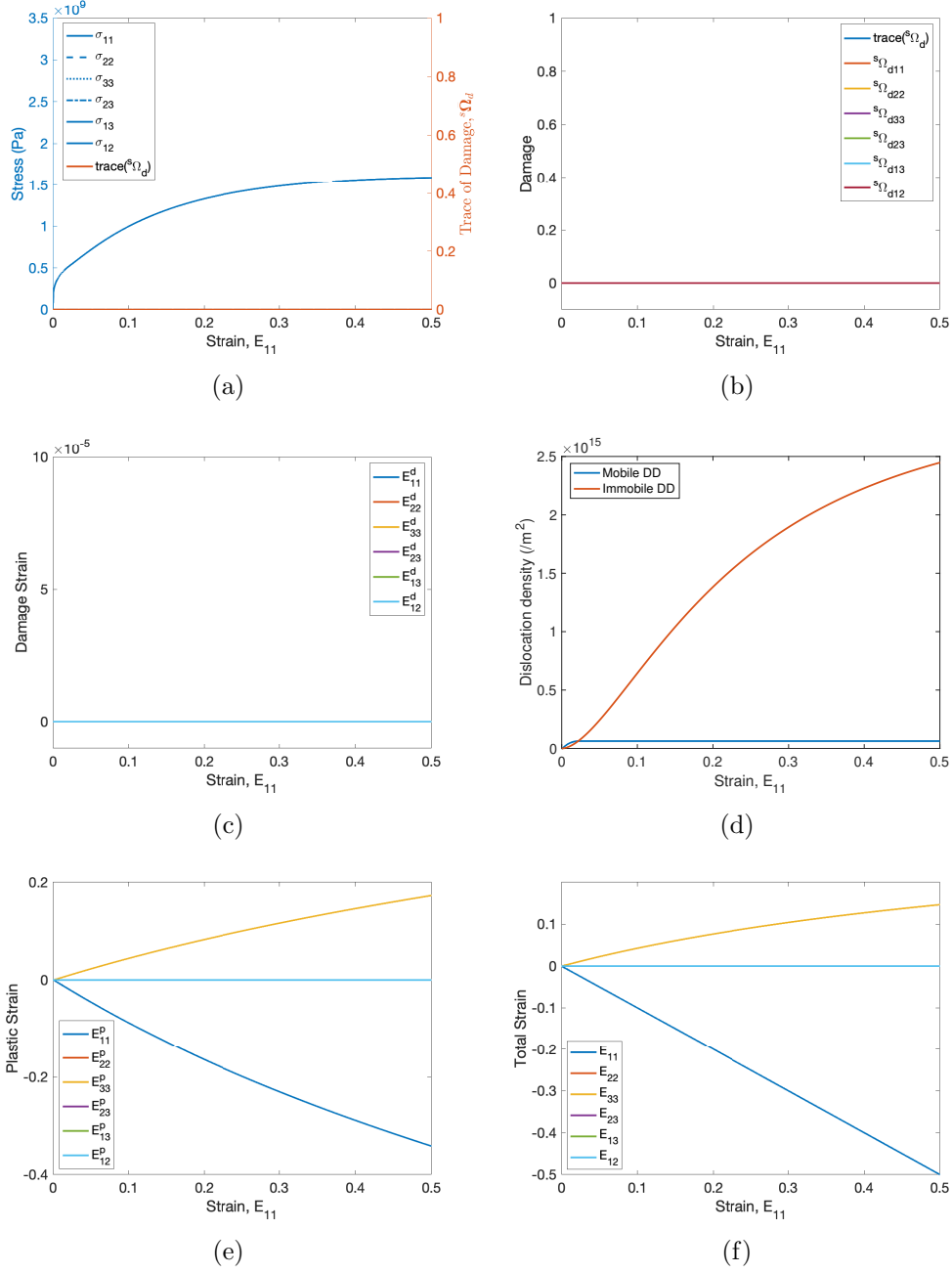


Figure 5: Representative results from the viscoplastic model, without the damage model. Plots are presented for following variables against the applied strain E_{11} : (a) uniaxial stress in compression, with superimposed trace of the damage tensor; (b) components of the damage tensor; (c) components of the damage strain tensor, Lagrangian; (d) immobile and mobile dislocation densities; (e) components of the plastic strain tensor, Lagrangian; and, (f) components of the total strain tensor, Lagrangian.

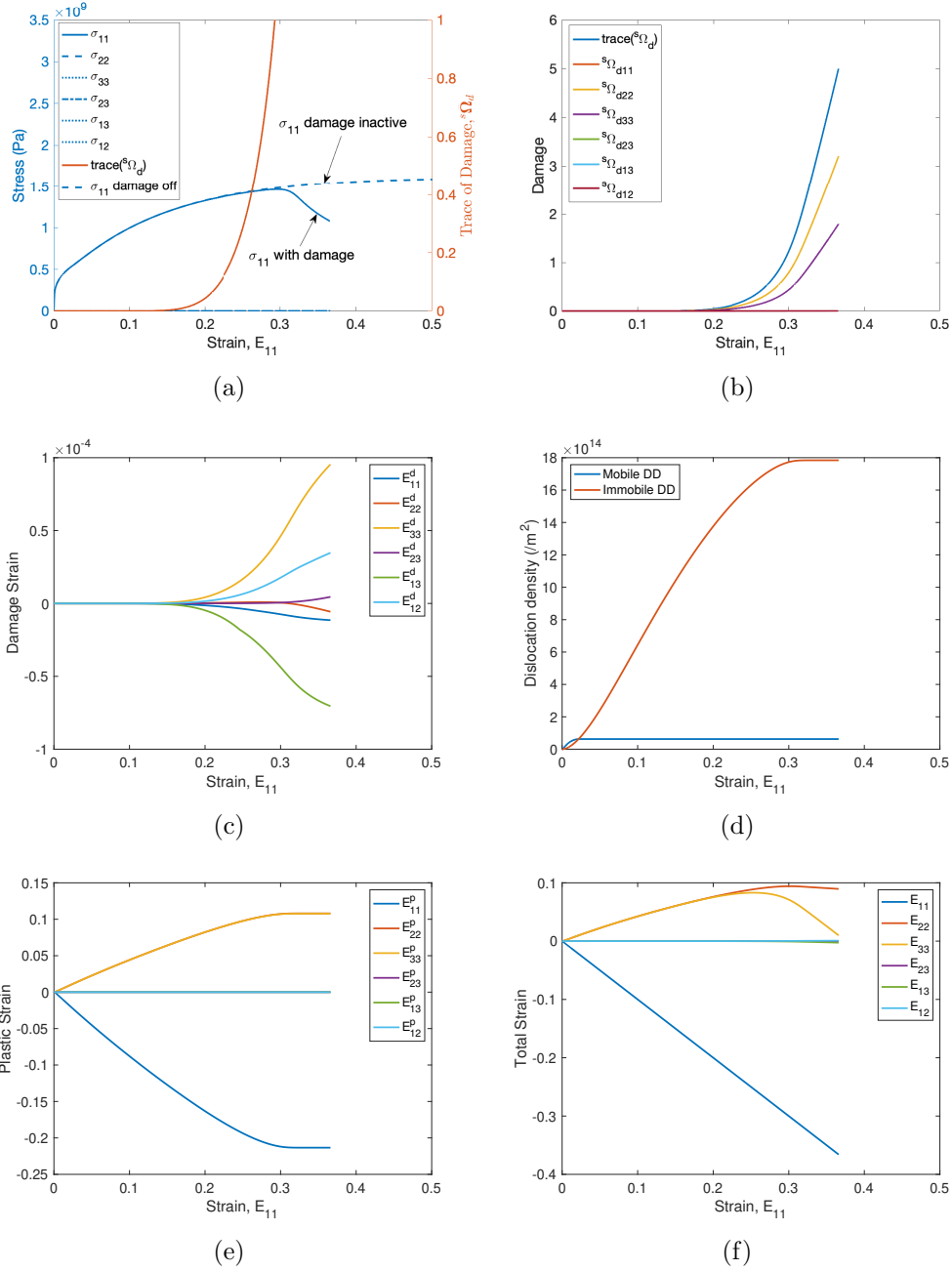


Figure 6: Representative results from the combined viscoplastic and damage models. Plots are presented for following variables against the applied strain E_{11} : (a) uniaxial stress in compression, with superimposed trace of the damage tensor; (b) components of the damage tensor; (c) components of the damage strain tensor, Lagrangian; (d) immobile and mobile dislocation densities; (e) components of the plastic strain tensor, Lagrangian; and, (f) components of the total strain tensor, Lagrangian.

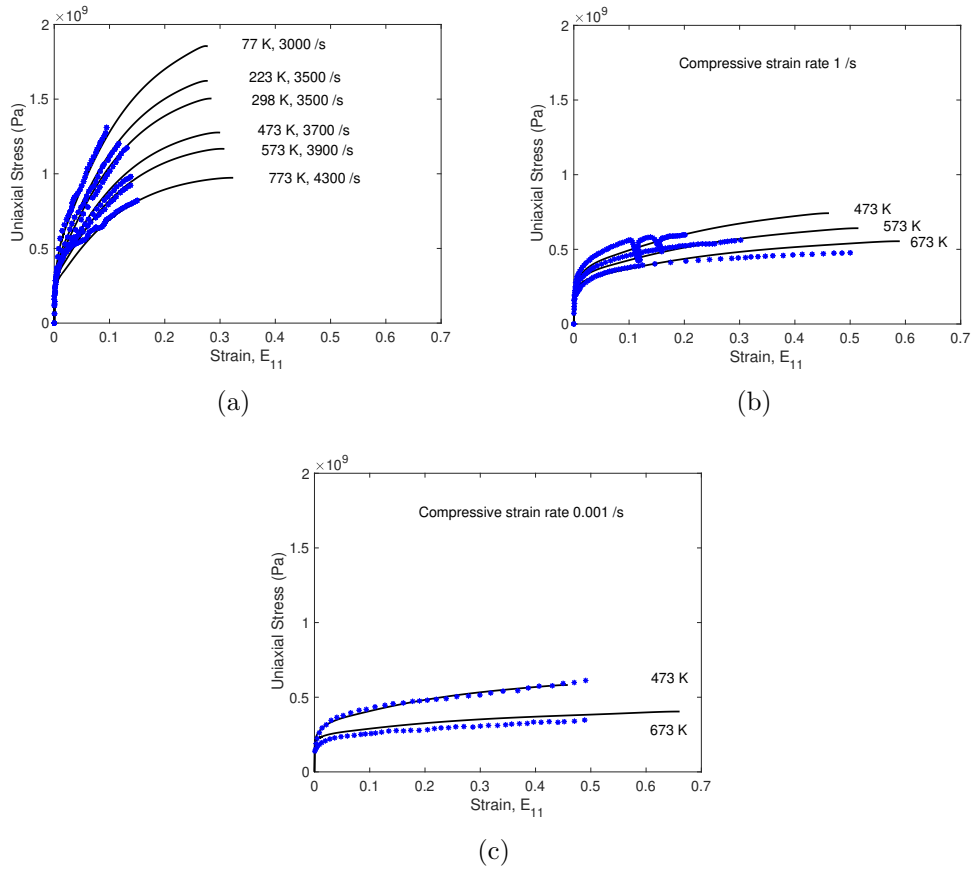


Figure 7: Outcome of model calibration to measured uniaxial stress-strain response under compression: (a) calibration to SHPB rates, with data from (Blumenthal et al., 1998); (b) calibration to moderate rates of 1 /s, with data from (Ablen et al., 1995) ; and, (c) calibration to quasistatic rates of 0.001 /s, with data from (Ablen et al., 1995).

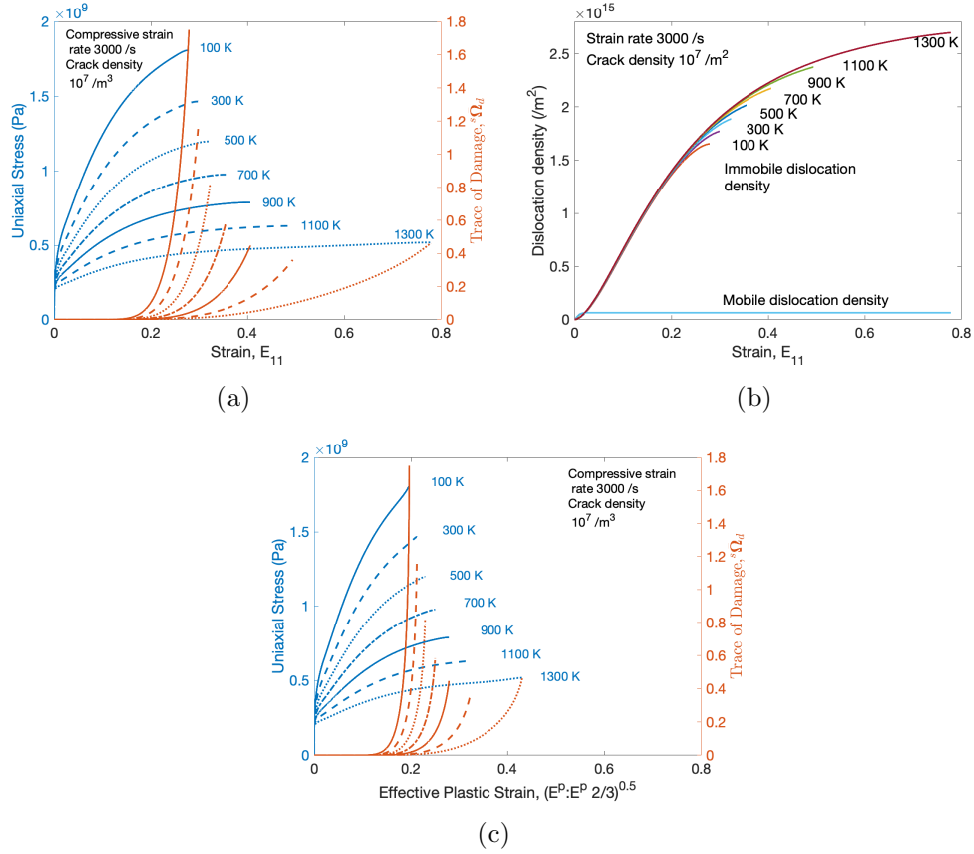


Figure 8: Temperature dependence of the mechanical response under compression for a fixed Stroh crack density $10^7 / m^3$ and rate of compression $3000 / s$: (a) predicted evolution of stress with applied strain, along with ultimate stress and ultimate strain, for temperatures in the range 100-1300 K; plot includes trace of the damage tensor; (b) evolution of immobile and mobile dislocation densities; and, (c) predicted evolution of stress with plastic strain. Plots includes trace of the damage tensor.

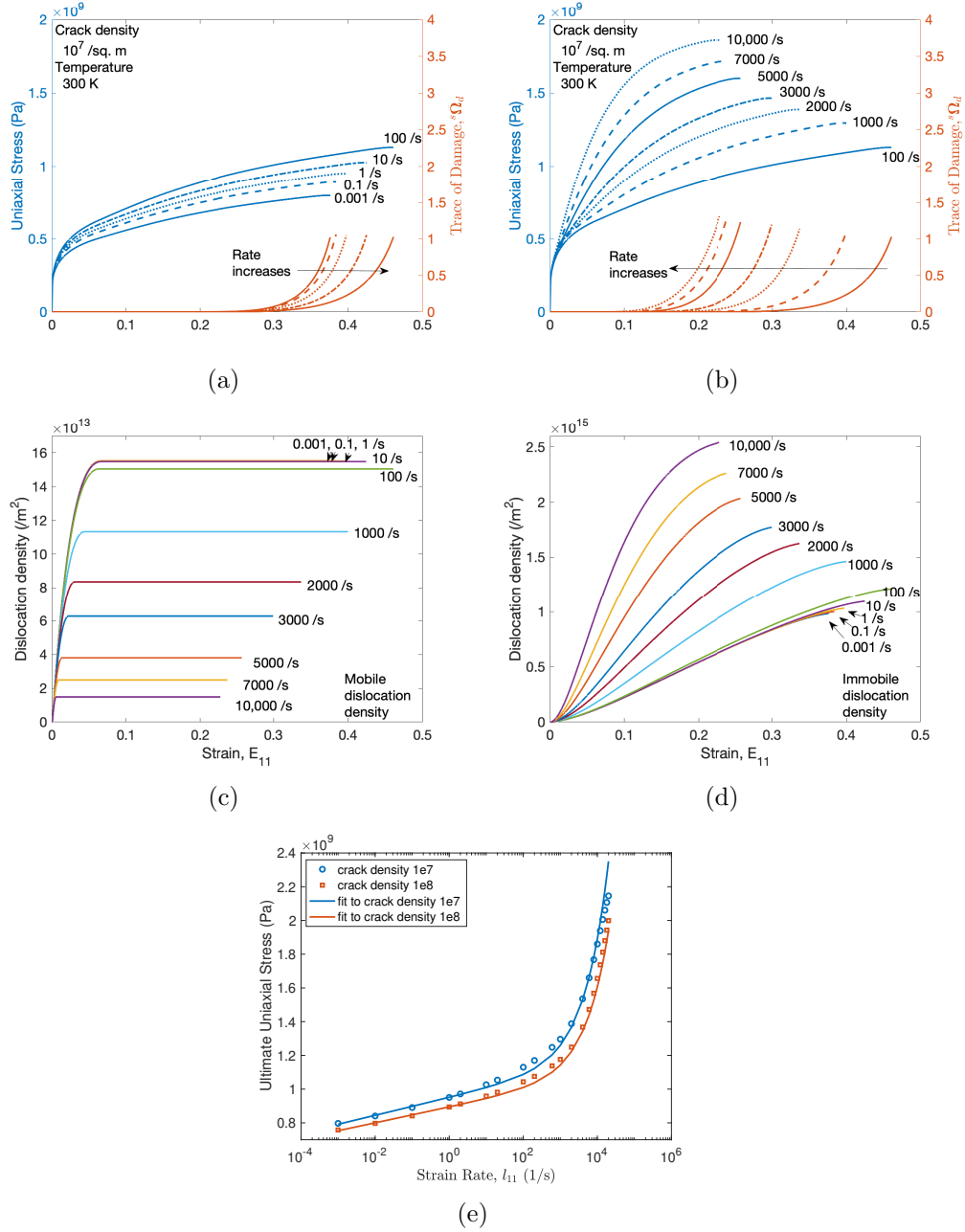
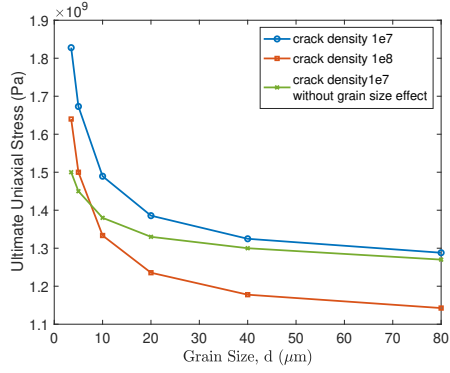
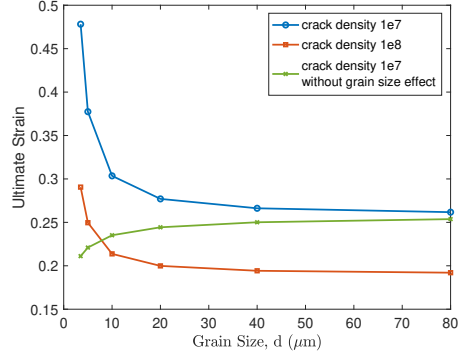


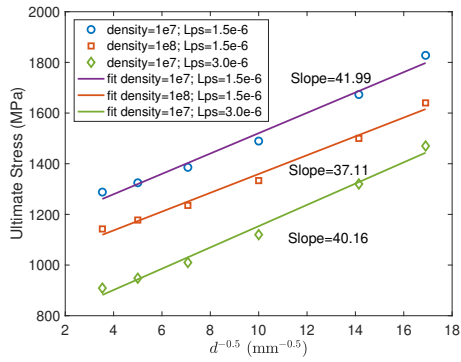
Figure 9: Rate dependence of the mechanical response under compression for a fixed Strohm crack density $10^7 / \text{m}^3$ and temperature 300 K: (a) uniaxial stress-strain for compressive rates 0.001-100 /s, with superimposed trace of the damage tensor; (b) uniaxial stress-strain for compressive rates 100-10,000 /s, with superimposed trace of the damage tensor; (c) evolution of mobile dislocation density for different rates; (d) evolution of immobile dislocation density for different rates; and, (e) calculated rate dependence of strength (markers) and superimposed analytic fit of Eq. (100), for Strohm crack densities 10^7 and $10^8 / \text{m}^3$.



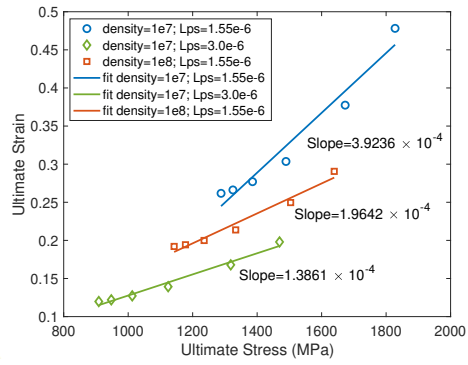
(a)



(b)



(c)



(d)

Figure 10: Grain size dependence of the mechanical response under compression: (a) ultimate stress in compression versus grain size, for fixed Strohm crack density, and with and without grain size effect in Eq. (31), (b) ultimate strain in compression versus grain size, for fixed Strohm crack density, and with and without grain size effect in Eq. (31), (c) ultimate stress versus inverse square root of grain size, for different Strohm crack densities and pileup spacing; and, (d) ultimate strain versus inverse square root of grain size, for different Strohm crack densities and pileup spacing.

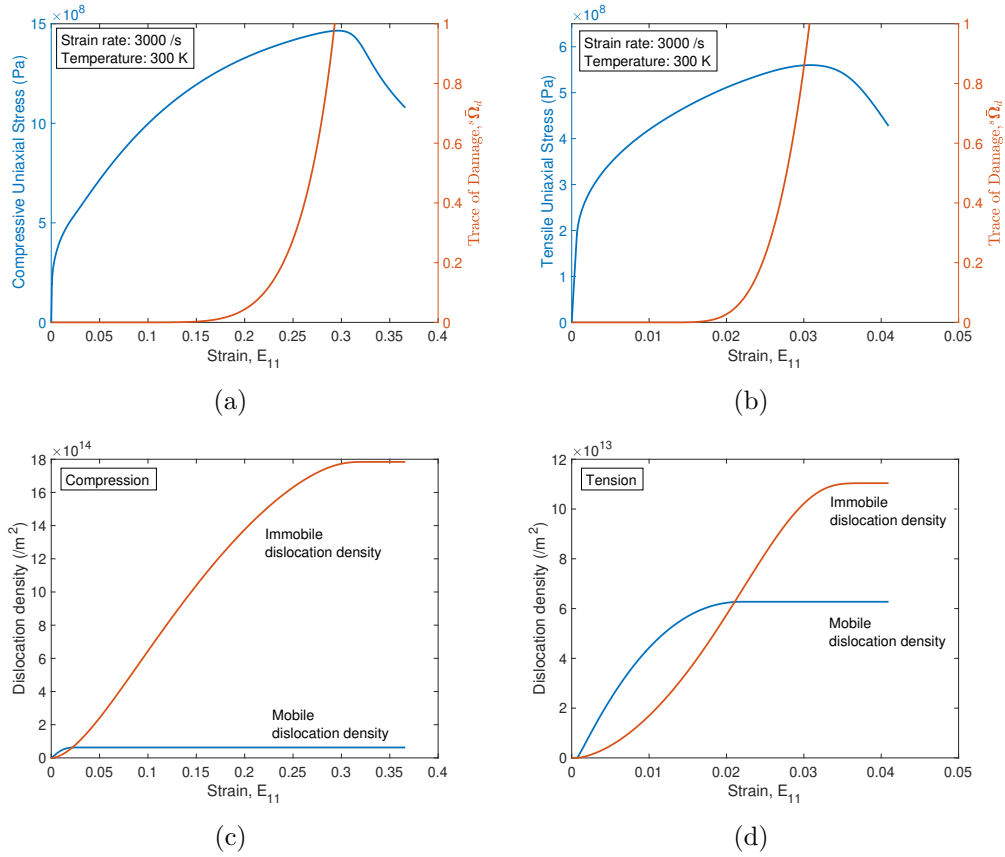


Figure 11: Tension compression asymmetry of failure response: (a) uniaxial stress-strain curve under compression, with superimposed trace of the damage tensor; (b) uniaxial stress-strain curve under tension, with superimposed trace of the damage tensor; (c) evolution of immobile and mobile dislocation densities under compression; and, (d) evolution of immobile and mobile dislocation densities under tension.